NPS-PH-92-006

NAVAL POSTGRADUATE SCHOOL

Monterey, California

A COMPARISON OF EIGHT CASES SELECTED FROM THE VANDENBERG AFB MT. IRON TRACER STUDY WITH RESULTS FROM THE LINCOM/RIMPUFF DISPERSION MODEL

R. F. KAMADA, S. A. DRAKE, T. MIKKELSEN
AND S. THYKIER-NIELSEN

DECEMBER 1991

FINAL REPORT FOR PERIOD
OCTOBER 1990 - SEPTEMBER 1991

Approved for public release; distribution unlimited

Prepared for:
U.S. Air Force, Space Division Los Angeles AFB, California 90009

NAVAL POSTGRADUATE SCHOOL
Monterey, California

Rear Admiral R.W. West, Jr.
Superintendent

H. Shull
Provost

This report was prepared for and funded by the U.S. Air Force Space Division, Los Angeles, CA., 90009.

This report was prepared by:

unclassified

SECURITY CLASSIFICATION OF THIS PAGE

REPORT DOCUMENTATION PAGE

Form Approved
OMB No 0704-0188

1a REPORT SECURITY CLASSIFICATION unclassified	1b RESTRICTIVE MARKINGS
2a SECURITY CLASSIFICATION AUTHORITY	3 DISTRIBUTION / AVAILABILITY OF REPORT approved for public release, distribution unlimited
2b DECLASSIFICATION / DOWNGRADING SCHEDULE	
4 PERFORMING ORGANIZATION REPORT NUMBER(S) NPS-PH-92-006	5 MONITORING ORGANIZATION REPORT NUMBER(S)
6a NAME OF PERFORMING ORGANIZATION Naval Postgraduate School 6b OFFICE SYMBOL (If applicable) PH	7a NAME OF MONITORING ORGANIZATION USAF Space Systems Division
6c ADDRESS (City, State, and ZIP Code) Physics Department (Code PH) Monterey, CA 93943-5000	7b ADDRESS (City, State, and ZIP Code) Los Angeles, CA 90009
8a NAME OF FUNDING / SPONSORING ORGANIZATION USAF Space Systems Div. 8b OFFICE SYMBOL (If applicable) USAF/SSD	9 PROCUREMENT INSTRUMENT IDENTIFICATION NUMBER MIPR FY76169100412
8c ADDRESS (City, State, and ZIP Code) Los Angeles AFB, CA 90009	10 SOURCE OF FUNDING NUMBERS PROGRAM ELEMENT NO / PROJECT NO / TASK NO / WORK UNIT ACCESSION NO

11 TITLE (Include Security Classification)
A Comparison of Eight Cases Selected from the Vandenberg Mt. Iron Tracer Study with Results from tne LINCOM/RIMPUFF Dispersion Model

12 PERSONAL AUTHOR(S)
R. F. Kamada, S. A. Drake, T. Mikkelsen, and S. Thykier-Nielsen

13a TYPE OF REPORT	13b TIME COVERED	14 DATE OF REPORT (Year, Month, Day)	15 PAGE COUNT
technical	FROM Oct 90 TO Sep 91	30 Dec 91	85

16 SUPPLEMENTARY NOTATION

17 COSATI CODES			18 SUBJECT TERMS (Continue on reverse if necessary and identify by block number)
FIELD	GROUP	SUB-GROUP	Atmospheric turbulent diffusion, mesoscale wind flow, lagrangian puff/plume dispersion

19 ABSTRACT (Continue on reverse if necessary and identify by block number)
The LINCOM/RIMPUFF plume dispersion model is used to simulate eight plume releases from the Mt. Iron study at Vandenberg AFB. LINCOM wind fields and RIMPUFF plume widths agree well with Mt. Iron but RIMPUFF plumes are longer, probably because the zinc sulfide tracer was not inert as previously assumed and was adsorbed by the surface canopy. Bi-modal dose isopleths resulting from passage over Honda Canyon are not well simulated. "Tower anchoring" improves wind field simulation if tower measurements are accurate over the time scale of dispersion. Centerline dose scatter plots, fractional bias, normalized root mean square error, and dose isopleth correlation areas (DICA) performance measures are compared. Fractional bias and DICA appear to be most robust. LINCOM/RIMPUFF modeling theory is presented in detail.

20 DISTRIBUTION / AVAILABILITY OF ABSTRACT	21 ABSTRACT SECURITY CLASSIFICATION	
☒ UNCLASSIFIED/UNLIMITED ☐ SAME AS RPT ☐ DTIC USERS	unclassified	
22a NAME OF RESPONSIBLE INDIVIDUAL R. F. Kamada	22b TELEPHONE (Include Area Code) 408-646-2674	22c OFFICE SYMBOL PH

DD Form 1473, JUN 86 *Previous editions are obsolete*

S/N 0102-LF-014-6603

SECURITY CLASSIFICATION OF THIS PAGE
unclassified

Table of Contents

Table of Figures

1. INTRODUCTION

The USAF Western Space and Missile Center is located along the southern California coast at Vandenberg AFB, where large Atlas and Titan rockets are used to launch polar orbiting satellites. Since the rockets are fueled by tanker trucks, USAF has directed much effort toward avoiding or mitigating the potential for large, accidental, ground level releases of toxic fumes.

If released, such fumes would disperse downwind according to the detailed mechanics of the release, nature of the propellants, and prevailing atmospheric conditions and terrain. Even during normal launch, massive amounts of propellants are released into the atmospheric boundary layer via the rocket exhaust cloud. Thus, USAF focuses part of its mitigation effort on field studies and computer forecast/nowcasts of such cold and hot spills to prepare toxic hazard corridors (THCs) for base and civilian personnel.

For example, Battelle Corp. conducted the Mt. Iron dispersion study from the three south base launch complexes, SLC-4, SLC-5, and SLC-6, with 252 zinc sulfide tracer releases from Dec. 1965 to July 1967 (Hinds and Nickola, 1967). Until the recent Lompoc Valley Diffusion Study (LVDE) of potential emissions from the Hypergolic Stockpile and Storage Facility (HSSF) (Skupniewicz, et al. 1990, 1991), Mt. Iron was the only field study involving tracer releases conducted from South Vandenberg. Eighty-eight releases were conducted from SLC-4, 25 from SLC-5, and 139 from SLC-6.

Since SLC-6 is presently decommissioned, SLC-4 is now the main launch pad for large Vandenberg rockets, Thus, in an effort to assess possible replacements for the currently used Ocean Breeze/ Dry Gulch (OBDG) type regression equations (Haugen and Taylor, 1963), more physically based computer models such as AFTOX and HOTMAC/RAPTAD (Kunkel and Izumi, 1991; Yamada and Bunker, 1991) have been used to simulate Mt. Iron releases from SLC-4. The Naval Postgraduate School (NPS) has made available an eight case subset of the Mt. Iron data set to the Vandenberg modeling community and has made efforts to coordinate the various simulation studies. This report describes the use of LINCOM/RIMPUFF, a dispersion model from RISO National Laboratory of Denmark, to simulate the above eight representative cases.

2. MOUNTAIN IRON DATA DESCRIPTION

2.1 The Vandenberg AFB Domain

Vandenberg AFB is located about 100 miles northwest of Los Angeles on the California coast. The Vandenberg domain features generally hilly terrain, punctuated by the east-west oriented Santa Ynez River Valley which separates North and South Vandenberg. The South

Vandenberg terrain is generally rougher than that of North Vandenberg with ridge to canyon elevation differences ranging from around 100 to 400m. At Pt. Arguello (near SLC-6) the coastline slants sharply eastward away from the generally north-south direction. This is repeated further south beyond Vandenberg by a similar coastline turning feature at Pt. Concepcion. Honda Ridge on South Vandenberg has a high point at Tranquillon Peak of over 600m and an average height of about 200m. It represents the northern edge of the coastal Santa Ynez Mountains. At an average elevation of about 60m, Honda Canyon, roughly 2km wide, separates Honda Ridge from Target Ridge, the first ridge south of SLC-4 (see fig. 1).

The climatological flow is from the northwest, controlled by subsiding anti-cyclonic flow around the chronic eastern Pacific High. Adiabatic compression of this subsiding air mass creates the typically strong, low California coastal subsidence inversion seen at Vandenberg. The northwesterly flow is augmented by the summer time California coast-to-Central-Valley monsoon, as well as the local seabreeze. However, the turning coastline at Pts. Arguello and Concepcion induces a local divergence of the climatological northwesterlies. Moreover, Honda Ridge, together with the typically low subsidence inversion, tends to divert daytime northwesterly flows to the west, so that winds over SLC-6 are usually channeled to a narrow range about the north-south direction (see Vandenberg Meteorology and Plume Dispersion Handbook, Kamada et al, 1989, hereafter referred to as the Handbook).

2.2 General Data Description

113 tests were conducted at SLC-4 and SLC-5 during Phase I of Mt. Iron in the first half of 1966. In the experimental design, fluorescent zinc sulfide tracer particles with a mean solid diameter of 2.5 μm was released as a wet aerosol fog from a test stand at a height of 12 ft, usually for 30 minutes. Sample tracer dosages were collected on membrane filters and assayed for fluorescence by alpha emission, using a Rankin counter. Due to the rugged terrain, the sampling lines were limited to existing paved and gravel roads as shown in fig. 2. Sampler spacing ranged between approximately 160 - 640 meters (0.1 - 0.4 miles), depending on distance from the release point. The 160m spacing was used for roads near the release site. A 320m spacing was used along the eastern section of Santa Ynez, Honda Canyon, Honda Ridge, and Tranquillon Mountain Rds. The 640m spacing was reserved for the section of the Sudden Coast Rd. from Pt. Arguello stretching south by southeast to Jalama Beach .

For this data/model comparison, we selected eight representative cases. The cases were chosen on the basis of completeness of the data set collected by Battelle during Mt. Iron and the significance of the presumed flow type as defined in the Handbook.

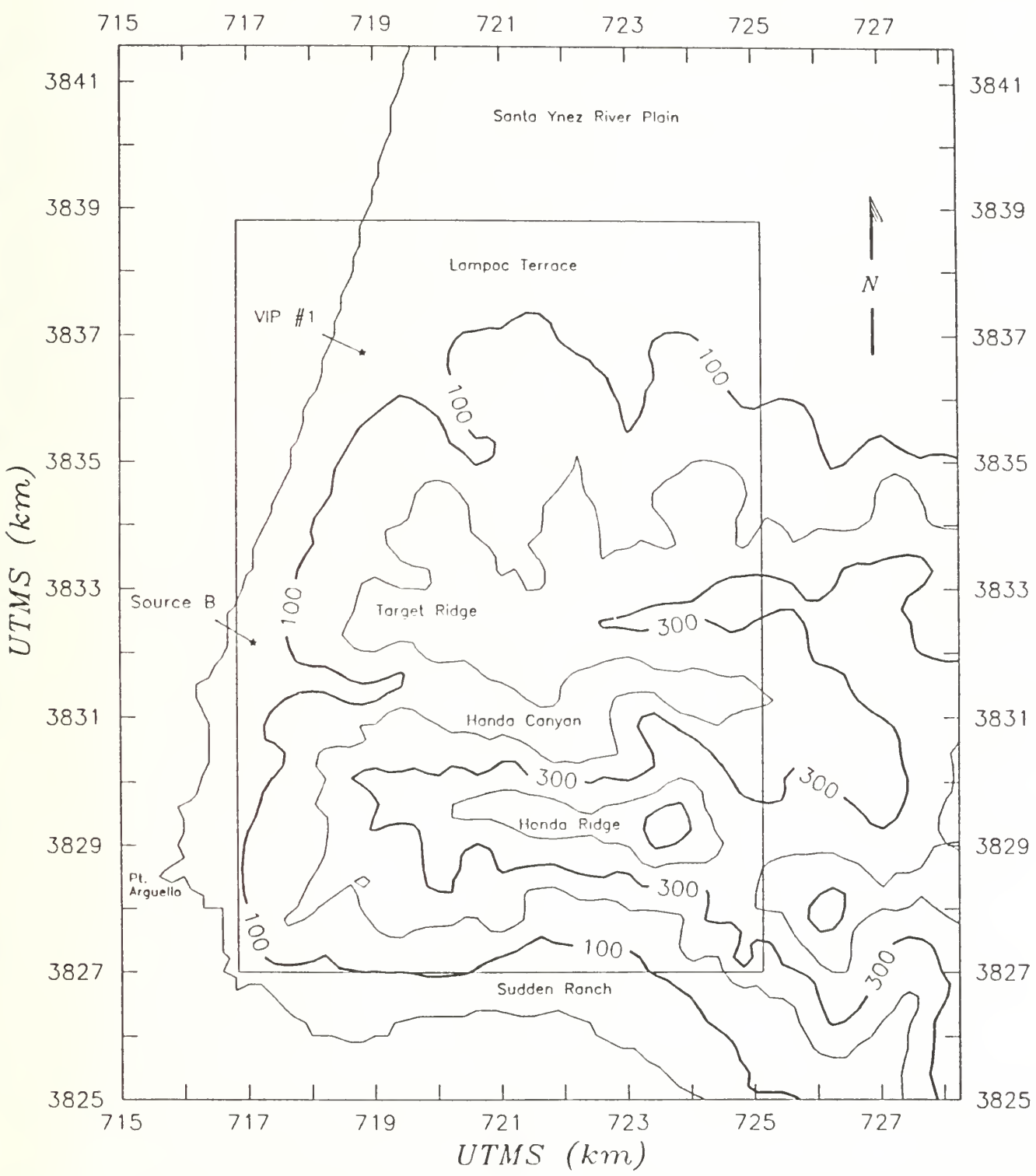

Fig. 1 Terrain Map of South Vandenberg. Inner rectangle shows the 100m inner grid area for RIMPUFF. Elevations are in meters.

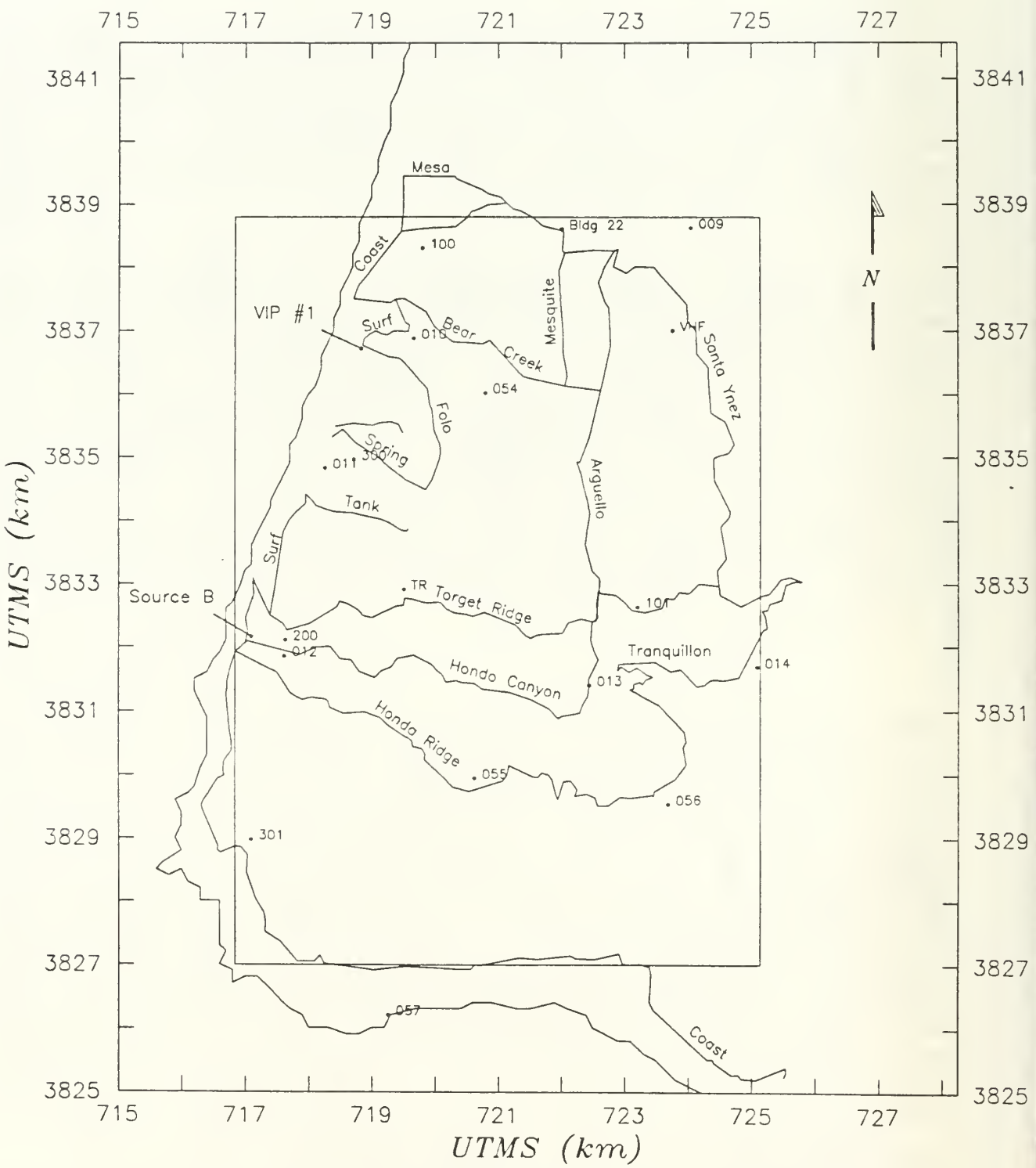

Fig. 2 Sampling routes over South Vandenberg for Mt. Iron. Inner rectangle shows the 100m inner grid area for LINCOM. Weather towers are numbered.

The available Mt. Iron sensor array consisted of towers, sondes, and bag samplers. There were: 1) wind speeds, directions, and direction standard deviations from 19 towers over 7.5, 30, 60, and 90 minute averages (shown in Tables 2.1.1, 2.1.2 and fig. 2), 2) tethersonde temperatures at approximately 20 meter intervals up to 260 m. The tethersonde (often referred to as a wiresonde) was located at the release site, either VIP-1 at the northwest corner of SLC-4 or Area 529 at the southwest corner of SLC-5. 3) twice-a-day NWS rawinsondes from Building 22, 4) supplemental rawin or radiosondes from VIP-1, Scout D, upper Honda Canyon, and the Boathouse. The rawinsondes were released as often as every hour for 3-4 hours, usually commencing one hour before tracer release. 5) bag sampling lines were deployed along Mesa, Coast, Surf, Arguello, Santa Ynez, Bear Creek, Folo, Tank, Target Ridge, Honda Canyon, Tranquillon Mt., Honda Ridge, and Sudden Coast roads, using a total of ~ 330 bag samplers. The Queen Air aircraft, used for 24 flights during Phase II, was deployed only for case 110 of the eight cases selected for study. For case 110 the plume centerlines derived from the aircraft data were essentially identical with those from ground sampling.

Table 2.1.1 Tower/Sonde sites

Program Index.	VAFB Site #.		
1	301		
2	056		
3	014		
4	012		
5	101		
6	Target Ridge		
7	011		
8	300		
9	054		
10	100		
11	VHF		
12	010		
13	009		
14	055		
15	057	(Boathouse, BH) *	
16	013	(Honda Canyon, HC) *	
17	200	(Scout-D, SD) *	
18	VIP-1	*	(Source)
19	B22	(Bldg.22) *	

The asterisks denote rawinsonde launches at the same site as the tower

Table 2.1.2 Wind Speed, Direction, θ, and Standard Deviation, σ_θ, for Main Sensor Sites

Site	28	31	48	55	87	90	91	110	Case
VIP-1		6.7	1.5	5.0	5.2	3.9	3.3	2.7	V m/s
	285	330	318	321	250	325	360	270	θ deg
	17	5			6	8	6	15	σ_θ deg
VHF	3.8	7.4		7.9	4.4	5.1	2.8	5.0	V
	294	341		333	275	303	340	296	θ
	7	13		14	11	5	5		σ_θ
Target	1.2	9.6	2.3	5.7	1.1	5.8	6.8	2.0	V
Ridge	269	4	55	339	271	298	324	323	θ
	3	19	6	11	12	9	6	9	σ_θ
WT101	4.1	7.4	4.1	7.4					V
	300	330	325	303	251	300	315	325	θ
	8	15	8	15	2	12	14	4	σ_θ
Telemetry	2.4	4.1		4.9	2.0	6.0	5.7	2.0	V
Peak	321	335		309	318	310	313	16	θ
	5	8		10	4	12	12	4	σ_θ
Ion	2.5	2.0	1.0	2.9	3.4	2.9	3.5	4.1	V
Sounder	259	328	235	288	256	1	360	249	θ
Honda Cyn	5	4	2	6	7	6	7	8	σ_θ
LaSalle	2.4		1.0	2.9	2.6	4.0	2.6	2.1	V
Canyon Rd	328		212	298	268	315	316	275	θ
Honda Cyn	5			9	5	8	5	4	σ_θ
WT200	1.9	2.3		0.5		1.2	0.8	2.7	V
	274	220	10	256	254	184	105	259	θ
	4	5		7	8	2	2	5	σ_θ
WT301	2.2			7.4	3.9	7.8	7.6	2.8	V
	339	339		340	204	1	15	329	θ
	5	15		15	8	16	15	6	σ_θ
Boat	3.5	7.5	7.0		2.3	13.0	14.5	4.6	V
House	280	350	315	340	213	309	313	239	θ
	7	17	13		7	26	29	9	σ_θ

2.3 Case Study Selection

As the Mt. Iron study gained momentum, hourly rawinsondes became available at up to four locations. However, this was not true in the early going, and the wiresonde at the release site was not operative for the first two dozen or so cases. Thus, upper air data during the early stages of the study was rather sparse. Even some of the ground based towers were not yet installed. So, although the Mt. Iron study began in the beginning of December 1965, our first study case with fairly complete data was case 28 which took place in February of 1966.

Many of the sensors also were inoperative at various times, particularly the wiresonde. Since release site winds and temperature structure are usually the most critical inputs when simulating plume transport, we tried to limit our selections to those cases where wiresonde data was available.

Within the available data, our other primary consideration was to sample as many flow conditions as possible. Table 2.2.1 summarizes ten significant flow types, as characterized in the Handbook.

Table 2.2.1 Surface Flow Types and Typical Conditions

	FLOW TYPE	FLOW ALOFT 052	ANGLE AT	INVERSION HEIGHT	USUALLY OCCURS	COMMON CAUSES AND FEATURES
1.	Moderate South westerly	SE over mixed* layer	190-310	Low	spring & fall	Seabreeze/easterly diurnal balance, mesoscale eddy
2.	Weak Westerly	Weak	240-290	Low	winter, or with summer stratus	Seabreeze with mild land-sea temperature difference
3.	Summer North westerly	Weak	290-340	Low/Mid	After noon	Pacific High & Monsoon
4.	Evening Northerly	Weak	340-070	Mid	Non-winter	Veering behind seabreeze front
5.	Stagnation	Weak	000-360	None (surface)	Near dawn	Weak Seabreeze/ slope drainage balance.Usually not stationary
6.	Nocturnal Easterly	varies	040-160	None (Surface)	winter	Slope drainage, winter monsoon, & diurnal
7.	Synoptic Easterly	Strong E	040-160	High or None	spring & fall	Warm, dry Santa Ana
8.	Storm Southerly	SW w/ upper trough	090-200	High or None	winter	Frontal passage
9.	Winter North westerly	Strong NW	290-030	Mid/High or None	After noon or storms	Postfrontal or Nevada Low if strong, Pac High/ seabreeze if weak
10.	Baja Southerly	?	090-170	Mid	fall	Surface low over Baja California

Low = 100m
Mid = 400m
High = 600m

With the above considerations in mind we selected the following cases from the 1966 data period:

Case	Date
28	February 16
31	February 24
48	March 29
55	April 21
87	June 13
90	June 21
91	June 22
110	June 22

All the flow types in Table 2.2.1, save for the Baja Southerly, can be viewed within the context of seasonal and diurnal variations in the Vandenberg area according to Table 2.2.2, also taken from the Handbook. Perhaps as many as five or six of the above flow types are represented among the eight cases. As is consistent with Vandenberg climatology, the vast majority of the Mt. Iron flows were either seabreeze or synoptic, post-frontal northwesterlies. These are represented in cases: 31, 55, and 90. Weaker seabreeze westerlies are also present in cases, 28 and 110. The evening northerly and perhaps partial stagnation is indicated in cases, 48 and 91. The remaining case, 87, is a seabreeze southwesterly, perhaps initiated by the positioning of the edge of the local stratus deck rather than competition between the seabreeze and a synoptic easterly.

Storm southerlies, nocturnal easterly drainage, synoptic easterlies, and Baja Southerlies are not indicated in the available data. The first of the three cases which might be construed as storm southerlies does not appear in the Mt. Iron data set until MI-175 from SLC-6 in January 1967 during Phase II. Since data collection during storm periods is difficult or impossible, perhaps this was intentionally avoided until a high level of field competence was achieved. The scarcity of easterly drainage flow cases during both Phase I and Phase II is not surprising, since most data were taken during daylight hours.

The upper air data was also valuable for visualizing the temporal and spatial evolution of the flow over Vandenberg (e.g, sea-breeze front location, marine layer depth, drainage, fog or stratus effects) and aided in determining the flow type analysis.

Since a number of rarer flow types characterized in the Handbook were not available within the data set, we also tried to skew the sampling to span all three available seasons and some night time cases. Thus, cases 31, 48, 90, and 91 were nocturnal releases,

while cases 28, 55, 87, and 110 were in daytime. Cases 28 and 31 occurred during late winter, 48 and 55 in spring, and 87, 90, 91, and 110 occurred in early summer. Tracer was released from SLC-6 exclusively during the fall season.

Seven of the eight cases were releases from SLC-4, with only case 55 being a release from SLC-5. Though not from SLC-4, case 55 was chosen because it was the only case indicating strong convection. In Phase I there were some instances of plumes from SLC-5 largely confined to flow up Honda canyon during the usual mid-morning seabreeze westerlies. But this pattern was not seen from SLC-4 and we did not include them.

2.4 Case Flow Analysis

The eight Mountain Iron cases extend from February to June, with marine boundary layer heights varying between 160 and 1300 meters. The following are capsule descriptions of the meteorology.

MI-28

Date : 16 February 1966
Release time : 1200 local
site : VIP #1
duration : 15 min
Flow Type : Seabreeze weak westerly (SWW)
Inversion : Deep, weak, at 1300 meters?

Flow analysis : The small horizontal variation in the temperature profile suggests modestly higher off-coast pressures indicative of a typical noontime, weak winter seabreeze. Wind vectors at WT301 and the Boathouse suggest that the flow diverges around the high terrain across Honda Ridge, where hill induced pressure gradients create the surface layer acceleration, evident at the 500m level at WT055. The veering indicated at Telemetry Peak and WT014 are probably due to local divergence initiated by the high terrain. Even at these modest wind speeds the evident flow distortion generated by Honda Ridge suggests a lower, stronger inversion than is indicated by sounding records.

MI-31

Date, release time: 24 February 1966
Release time : 1845 local
site : VIP #1
duration : 15 min
Flow Type : Synoptic Northwesterly (NW)
Inversion : Unknown, probably deep

Flow analysis : Wiresonde temperatures were available only to 220m. Hence, the lack of upper wind or cloud data precludes certainty. However, the strong northwesterly flow, wind speeds and time of year suggest post-frontal forcing with modest veering within Honda Canyon and surface layer acceleration across Honda Ridge. The lack of flow divergence to the westward, lower portion of Honda Ridge also suggests a high inversion, consistent with post-frontal conditions. The abscence of backing once the flow has passed beyond the ridge is consistent with this interpretation.

MI-48

Date : 29 March 1966
Release time : 2315 local
site : VIP #1
duration : 5 min
Flow Type : Nocturnal Drainage (ND)

Inversion : Elevated subsidence type at 400m near release site but with large variability. For example the inversion above the boathouse appears low, perhaps due to radiation fog.

Flow analysis : Tower winds show veered, northwesterly remnants of a seabreeze disturbed by more veering across Honda Ridge. The inversion lid forces the flow west over the lower portion of Honda Ridge. South of the ridge, continuity forces the winds east again, as seen at the Boathouse. Downslope drainage flow into the canyons is seen at low levels, with complicated reverse flow due to radiation fog which forms in the larger drainage pool areas such as upper Honda Canyon.

MI-55

Date : 21 April 1966
Release time : 1109 local
site : Bldg 529 (SCOUT)
duration : 30 min
Flow Type : Northwesterly

Inversion : Weak subsidence type at 650m.

Flow analysis : Well-mixed boundary layer up to the inversion with winds maximizing at 200-300m, then decreasing aloft. Humidity profiles indicate cloud cover over Honda Canyon and Scout D. In view of the unstable lapse rates indicated by both the rawin and wiresondes, this suggests spring cumulus convection, consistent with the short plume footprint. Flow distortion across Honda Ridge, similar to MI-48, is still evident but weaker, perhaps due to the higher, weaker inversion.

MI-87

Date : 13 June 1966
Release time : 1310 local
site : VIP #1
duration : 30 min
Flow Type : Southwesterly seabreeze

Inversion : Low subsidence type at 250m.

Flow analysis : The flow is weakened and backed from its usual summertime pattern near the surface. However, rawinsondes and towers along the ridge lines show that the higher level winds retained the usual northwesterly seabreeze character for this time of day. This is the opposite pattern from that expected for southwesterlies induced by inland high pressures, the kind which give rise to hot e terly Santa Anas further south. In this case the seabreeze has ought a fog front with it, leading to a low level, thermally based, southwesterly "fog breeze".

MI-90

Date : 21 June 1966
Release time : 2300 local
site : VIP #1
duration : 30 min
Flow Type : Northwesterly summer seabreeze

Inversion : High subsidence type at 600m.

Flow analysis : The high inversion, clear skies and strong winds this late into the evening suggest some frontal augmentation of the usual seabreeze. The usual flow distortion over and around Honda Ridge is again shown by the wind vectors at WT301, 055, and 057. Tripling of the speed at WT055 suggests strong flow funneling near the inversion, as well as acceleration over hills, due to hill induced pressure gradients (Jackson and Hunt, 1979). The anomalous southerly flow at the mouth of Honda Canyon is hard to explain, except as instrument error. However, we speculate that the high winds at the Boathouse may be due to a lowered inversion height and consequent high speed funneling south of Honda Ridge. The boundary layer may be lower south of the ridge because the ridge obstructs and dams the northwesterly flow, inducing a Scorer type of hydraulic jump across the ridge. Rippling of the inversion base by leeside gravity waves may augment this effect.

MI-91

Date : 22 June 1966
Release time : 0203 local
site : VIP #1
duration : 30 min
Flow Type : Evening Northerly

Inversion : Mid-level subsidence type at 400m.

Flow analysis : This release occurred three hours after case 90. In the interim winds have veered from northwesterly to northerly and weakened somewhat, due to the lack of thermal forcing. This follows the summer seabreeze pattern outlined in the Handbook. According to rawinsondes, the veering occurred around 0000 local time and appeared more evident above 600m, while the inversion base fell sharply (by ~250m). These changes may be consistent with post-frontal relaxation of the hydraulic jump mentioned in the case 90 analysis. Even so, northerly forcing remained intense enough to avoid any drainage or higher level easterly return flow tendencies, as often appear later at night. Again, the usual flow distortion over and around Honda Ridge shows up in the wind vectors at WT301, 055, and 057. And the wind vane at the mouth of Honda Canyon still seems in error.

MI-110

Date : 22 June 1966
Release time : 1055 local
site : VIP #1
duration : 30 min
Flow Type : Seabreeze Weak Westerly

Inversion : strong subsidence type at 160m

Flow analysis : This release occurred eight hours after case 91. In the interim winds have veered completely around to westerly. Inland heating has burnt back the overnight stratus cover to near shore, above which remains the ever present subsidence inversion. However, the seabreeze is still weak, due to the limited heating period, nor has Coriolis induced veering really begun yet. This follows the summer seabreeze pattern outlined in the Handbook. According to rawinsondes, winds backed rapidly above the inversion to a light southeasterly, also typical of the general seabreeze circulation pattern at Vandenberg.

3. LINCOM-RIMPUFF MODEL DESCRIPTION

3.1 LINCOM

There are two general classes of models, diagnostic (steady state), and prognostic (time marching). Diagnostic codes are suited for nowcasts where immediate toxic hazard corridors (THCs) are needed for accidental spills. Prognostic codes are more suited for forecasts of hypothetical spills or planned launches. This distinction blurs, if a diagnostic model is fast enough to provide frequent updates based on perhaps a five minute or better basis, or if faster-than-real-time prognostic codes are run continuously and frequently nudged by new input data. LINCOM is a five level, diagnostic boundary layer flow model, which when combined with a puff dispersion model such as RIMPUFF, is fast enough to allow such updates on a two minute basis. LINCOM 1.0 itself requires about one minute for a typical case at 500m resolution over a 40 x 60 km domain on a 386/33 PC.

LINCOM was developed by Ib Troen at the RISO National Laboratory in Roskilde, Denmark (Troen, 1986). Other recent contributers have been George Lai, Ray Kamada, and Torben Mikkelsen.

LINCOM uses linearized versions of the u, v, and w components of the momentum equation, the boundary layer mixing form of the mass continuity equation and the equation of state. LINCOM versions 1.0 and 1.1 both neglect the temperature equation (also termed the thermodynamic energy equation). Thus, neither stable nor unstable conditions are treated within the governing equations. However, through an objective analysis scheme applied after the solutions from the governing equations are obtained, LINCOM is designed to match the tower data exactly, with dynamic interpolation between towers. That is, at grid points between the tower inputs, LINCOM adjusts the winds by combining linearized dynamics with a terrain modified, inverse-distance-square based objective analysis. So LINCOM conforms to the actual winds and the thermodynamic and dynamic forcings, to the level of accuracy and resolution provided by the towers. Since LINCOM operates at five levels within the boundary layer (default values are: 6', 54', 0.2 Zi, 0.5 Zi, and 0.8 Zi), levels above the towers use similarity based extrapolations.

LINCOM 1.0 was used for the Mt. Iron study. However, in version 1.1, the resultant wind field is not completely anchored to the tower data, as is discussed below.

LINCOM is speed optimized by two techniques. First, we transform the Vandenberg terrain from grid point to Fourier spectral space wherein the governing equations are solved. In this way the same resolution can be achieved using far fewer sine/cosine waves as grid points. Second, instead of numerically solving the governing

equations at each grid point, linearization lets us pre-calculate symbolic solutions so that only the coefficients for each wave number need further adjustment. Together these two techniques allow more than an order of magnitude speed increase over standard finite difference methods.

In addition, for linearized neutral flow, Lai (unpublished) showed recently that the total flow can always be expressed as a linear combination of independent orthogonal components of the mean and perturbed flows along just the x and y axes. Since the orthogonal flows are pre-calculable, we can simply find the mean wind speed and direction which best matches the Vandenberg tower winds and apply them to pre-calculated solutions. In version 1.0, a "look-up" mode employs a set of 72 wind fields spaced in three degree increments around 360° of arc which are interpolated to obtain the final field. However, in version 1.1, the best linear combination of two pre-calculated orthogonal fields is provided.

Trade-offs are involved in formulating such a model. Since LINCOM does not account for time tendencies in the velocity, dynamical forcing due to terrain is effectively propagated instantaneously over the entire domain, rather than at some realistic set of phase speeds. Linearization of the governing equations also means that second and higher order perturbation terms are neglected. In a prognostic scheme, such solutions would gradually diverge from reality. However, for a diagnostic model, where in effect only the present time step is being considered, this issue is not very significant.

Another aspect of linearization in LINCOM is that for each grid point, the vertical velocity is basically assumed equal to the horizontal velocity at that site times the sine of the terrain slope. This approximation only holds well for slopes of less than twenty degrees. Thus, the aspect ratio of the terrain (typical height/typical length) must be relatively small compared to unity. ACTA's analysis of the Vandenberg terrain concludes that at 500 meter resolution, hardly any of the terrain shows slopes greater than twenty degrees (Conley et al., 1990). Thus, the quantitative limit for the vertical velocity assumption is seldom exceeded at Vandenberg.

Transformation of the domain to spectral space involves the assumption of periodic boundary conditions. So wave energy leaving one boundary will immediately re-enter the domain from the opposite boundary. For this reason, a 10 km buffer zone was created around the Vandenberg domain in which the terrain is gradually relaxed on all sides to sea level. This has the effect of greatly damping such wave motions. However, the effect of periodic boundary conditions cannot be avoided completely and we do not have a quantitative assessment of its influence on the flow as yet.

Again, the effect of the objective analysis in LINCOM 1.0 is to anchor the resultant wind field to the wind vectors given by the Vandenberg base tower system. In LINCOM 1.0 Monin-Obukhov similarity theory is used to extend the tower vectors upward into the outer boundary layer. In effect this turns LINCOM into a dynamically based interpolation/extrapolation scheme based on the tower winds. However, the tower winds may be influenced by effects which are more local than can be resolved by the implemented 500 meter grid spacing, such as buildings and local terrain. This constitutes a type of aliasing. Since the objective analysis is not inherently mass conserving, such local streamline divergence indicated by the towers can cause departures from the continuity constraint implemented in the model physics. However, since LINCOM 1.1 is a best fit to, rather than an anchoring by the tower vectors, strict mass conservation is retained, while avoiding the aliasing issue.

Most of the available towers are clustered near the coast on Vandenberg property. Other towers are available from the Santa Barbara Air Quality Management District's set of towers, some of which are actually maintained by the regional oil refineries. There are also two local buoys maintained by NOAA and towers atop a few of the local oil drilling platforms. However, these sources have not been incorporated as yet into the on-line data stream.

3.2 RIMPUFF

There are four classes of plume diffusion models which are being considered for use at Vandenberg. In ascending order of computational demands they are: 1) steady state plume model with gaussian lateral concentration profile, 2) mixed layer scaling model, 3) lagrangian puff model with gaussian radial concentration profile, 4) lagrangian particle model with particle motions governed by a mean wind plus a random turbulent component with a gaussian velocity profile. RIMPUFF is a lagrangian puff model.

RIMPUFF is structured to handle multiple simultaneous sources. Release points can be located anywhere within the 3-D grid and can be specified individual release rates, release times and heat production. A series of puffs is released to simulate a continuous plume. At each time step, a book-keeping algorithm tracks the advection, diffusion, and fractional deposition of each puff in accordance with local meteorological parameters. The model calculates the concentration at each grid point by summing the contributions from all the surrounding puffs. These concentrations can simply be updated or also accumulated to provide dosage. The model output consists of individual puff locations and grid concentrations at user specified time intervals. From these results, a graphics program produces puff plots and concentration or dose isopleths.

RIMPUFF employs the LINCOM mean flow field to advect contaminant puffs downstream. Within-puff growth is controlled by local turbulence level, using two-particle relative diffusion theory. Local turbulence intensity depends on tower based climatological/ directional parameterizations of σ_θ, the standard deviation of wind direction, for lateral turbulence, and Pasquill-Gifford stability classes modified for complex terrain for the vertical turbulence.

RIMPUFF treats plume bifurcation in complex terrain by letting puffs split when they exceed the size of the grid spacing. I.e., for Vandenberg an initial 100m puff will grow to the 500m LINCOM grid spacing before it splits horizontally into five 250m puffs (pentafurcation). Vertical trifurcation can occur independently. The practical splitting limit on PC based computers is several hundred puff progeny. Mass, momentum, and center concentration (of the mother puff) are conserved in the splitting process. If the mean flow is not frequently updated and remains static, RIMPUFF adds stochastic (Langevin based) advection to simulate puff meander due to sub-grid turbulence. This is particularly important when puff siblings are closely spaced shortly after splitting.

Since the series of puffs is meant to simulate a continuous plume, the effective stack height after plume rise is taken from standard plume rise models for hot spill cases. 100% reflection is assumed at a user specified inversion height which parallels the terrain. The final rise height for each puff is a function of the atmospheric stability and windspeed at the time and height of the release as given by LINCOM.

For Mt. Iron the ground level reflection coefficient was set to 100%. Dry deposition is calculated using the source depletion concept according to stability and windspeed. Wet deposition accounts for rain intensity and duration in time and space, using a $1/r^2$ objective analysis, where r is the distance from the grid point to the measurement station.

As a puff model RIMPUFF has advantages over gaussian plume and similarity scaling models. It can handle non-homogeneous terrain during non-stationary conditions. As plumes extend to farther distances and longer travel times, they are more likely to encounter and respond to such variations. In complex terrain, non-gaussian profiles can occur which RIMPUFF can treat, such as bifurcated plumes, pooling, non-homogeneous channeling, and fanning.

Gaussian plume and mixed layer scaling models must also assume some kind of profile for the vertical concentration distribution. A gaussian vertical profile may be modified to account for surface reflection. This is appropriate for short distances before a significant amount of reflection occurs from an upper level inversion. At long distances a uniform vertical concentration may

be assumed. In fact, neither of these simple assumptions is entirely reasonable, since plumes will spread vertically until an inversion is reached, then reflect and mix downward in a gradual and complex fashion. Non-stationary lagrangian puffs and particles should be able to model such complex phenomena more accurately.

Puff model accuracy is mitigated, especially near the source, by finite puff size and assumed radially gaussian concentration profiles. Lagrangian particle models improve on these aspects. But they require a much larger particle swarm and more computer time. RIMPUFF's stochastic puff advection scheme is also not well tested yet. On the other hand, lagrangian particle models assume a gaussian velocity component to diffuse the particles. Yet, the vertical velocity distribution has positive skewness and therefore is not gaussian under convective conditions. Baerentsen and Berkowicz (1984) and Misra (1982), however, claim better results with an adjustable double gaussian distribution for their lagrangian models.

4.0 DATA/MODEL COMPARISON METHODS

4.1 Initialization

With a model to model comparison, it is trivial to create output grids with compatible domain size and grid spacing to quantitatively compare the results. However, a model to data comparison such as Mt. Iron requires some manipulation before quantitative results may be obtained.

Among the products of the Mt. Iron Experiment was a set of hand-drawn isopleths defining measured dosages for each case, given in terms of time-integrated concentrations normalized by release rate (units of 10^9 sec/m^3). However, these results were not immediately compatible with the format required for comparison with LINCOM/RIMPUFF which defines dosages at distinct points on a grid. Thus, the eight cases from Mt. Iron were digitized onto a 119 x 84 evenly spaced grid at 100m mesh spacing, and formatted for the commercial SURFER PC plotting package (Golden Software, 1989). This domain size was large enough to encompass the Mt. Iron and LINCOM/RIMPUFF plumes yet small enough to comply with the grid size constraints of SURFER (see figs. 1 and 2).

Inspection revealed that some of the hand-drawn dose isopleths from Mt. Iron were extended beyond the scope of the bag sampling network, presumably to ensure closure of the contour lines. Such extrapolation beyond the measurements in cases: 28, 48, 87, 90, and 110 cannot really be justified, since it relies on subjective judgement. In these cases both the modeled and measured isopleths were truncated along the last measurement line. For instance, in

case 28, the measured plume passed over the sampling line along Arguello Road, but did not reach Santa Ynez Road. Since the exact loci for dose isopleths between these two sampling lines was not known, the isopleths were truncated at Arguello Road for the DICA and other comparisons.

For the following cases the cut-off lines were:

Mt. Iron Case	Plume Cutoff
28	Arguello
48	Honda Ridge
87	Arguello / Santa Ynez
90	Tranquillon / Honda Ridge
110	Arguello

Measured dosages along the Coast Road in the vicinity of Sudden Ranch for case 91 were sufficient to resolve the plume, whereas for case 48, measured dosages were too small and the plume was truncated at Honda Ridge.

4.2 DICA and Other Merit Scoring Methods

The Dose Isopleth Correlation Area (DICA) scoring method is a conceptually simple performance measure we created to compare the coincidence between LINCOM/RIMPUFF dose isopleths and the hand drawn ones, based on Mt. Iron. From simple set theory, for each case and each dose isopleth within a case, DICA divides the total area of intersection between each modeled and measured isopleth by the total area of union. However, before being summed, it weights each intersect by the measured to modeled isopleth value ratio. Thus, if there are k number of isopleths with modeled and measured doses, a_i, a_j, and modeled and measured areas, A_i, A_j, the DICA algorithm is

$$\left[\sum_{j=1}^{k} \sum_{\substack{i=1 \\ a_i \le a_j}}^{k} (a_i/a_j) A_i \cap A_j + \sum_{i=1}^{k} \sum_{\substack{j=1 \\ i=j \\ a_j \le a_i}}^{k} (a_j/a_i) A_j \cap A_i \right] \Big/ \left[\sum_{i=1}^{k} A_i \cup \sum_{j=1}^{k} A_j \right] . \qquad (4.2.1)$$

This yields a single value, ranging between zero and one, for the amount of overlap between modeled and measured results. Perfect congruence yields unity, while no overlap yields zero.

DICA presents a fairly stiff test of "goodness of fit". That is, the congruence must be quite good to obtain DICA values above 0.5. Thus, we suggest the following interpretation of DICA scores,

DICA VALUE	FITTING ACCURACY
0.5 – 1	excellent
0.2 – 0.5	good
0.05 – 0.2	fair
0.00 – 0.05	poor.

In addition to DICA two other performance measures were utilized as suggested by Hanna (1991), fractional bias,

$$FB = \overline{(D_0 - D_m)} / \overline{(D_0 + D_m)} \quad , \qquad (4.2.2)$$

and normalized mean square error,

$$NMSE = \overline{(D_0 - D_m)} / \overline{D_0 D_m} \quad , \qquad (4.2.3)$$

where D_0 and D_m are the modeled and measured dosages at each grid point. Programs were written to determine DICA, FB, and NMSE values for each of the eight cases.

FB is useful for showing which plume predicts the largest dosages. A zero FB indicates that the model predicts on average the same dosage as was measured. The NMSE should be behaviorally similar to DICA, except that lower NMSE should imply better model predictions, while higher DICA values indicate a better fit (see discussion of relative merits in section 5.2).

All values which exceeded the lowest isopleth value of 20 are included. If either the RIMPUFF or Mt. Iron dosage value at a given grid point exceeded the minimum threshold value, then that grid point was included in the averaging process for the FB and the NMSE scores.

We also show a standard comparison of observed versus modeled centerline dose exposure levels, including factor of two and factor of four error limits (fig. 27).

5. DATA/MODEL COMPARISON RESULTS

5.1 LINCOM Winds, RIMPUFF/Data Isopleths, DICA and Other Results

Results of each Mt. Iron case and LINCOM/RIMPUFF simulation are plotted in figs. 3-27. Dose isopleths are given in terms of time-integrated concentrations normalized by release rate (10^9 sec/m^3). Locations are given in Universal Transverse Meridian System (UTMS) coordinates at 100 m resolution. The release location for case 55 was at the mouth of Honda Canyon near SLC-5. The other seven releases were from VIP #1 at the northwest corner of the SLC-4 area along the Coast Road.

The DICA, FB, and NMSE values are presented in Table 5.1 for the eight cases.

Table 5.1.1 Comparison of model performance measures.

Case	Number of points	D_o	D_p	$(D_o-D_p)^2$	FB	NMSE	DICA
28	575	420	684	1,175,025	-0.477	4.082	0.369
31	1038	231	187	125,231	+0.207	2.863	0.266
48	1499	178	225	135,991	-0.233	3.391	0.268
55	692	132	142	133,124	-0.069	7.063	0.121
87	692	264	355	265,698	-0.294	2.825	0.535
90	1589	285	460	837,967	-0.470	6.375	0.328
91	2209	177	187	387,625	-0.054	11.700	0.369
110	517	303	470	484,409	-0.432	3.395	0.472

Fig. 3 Mt. Iron Case 28 plume isopleths and tower wind vectors from the Mt. Iron Report Phase I Vol. I.

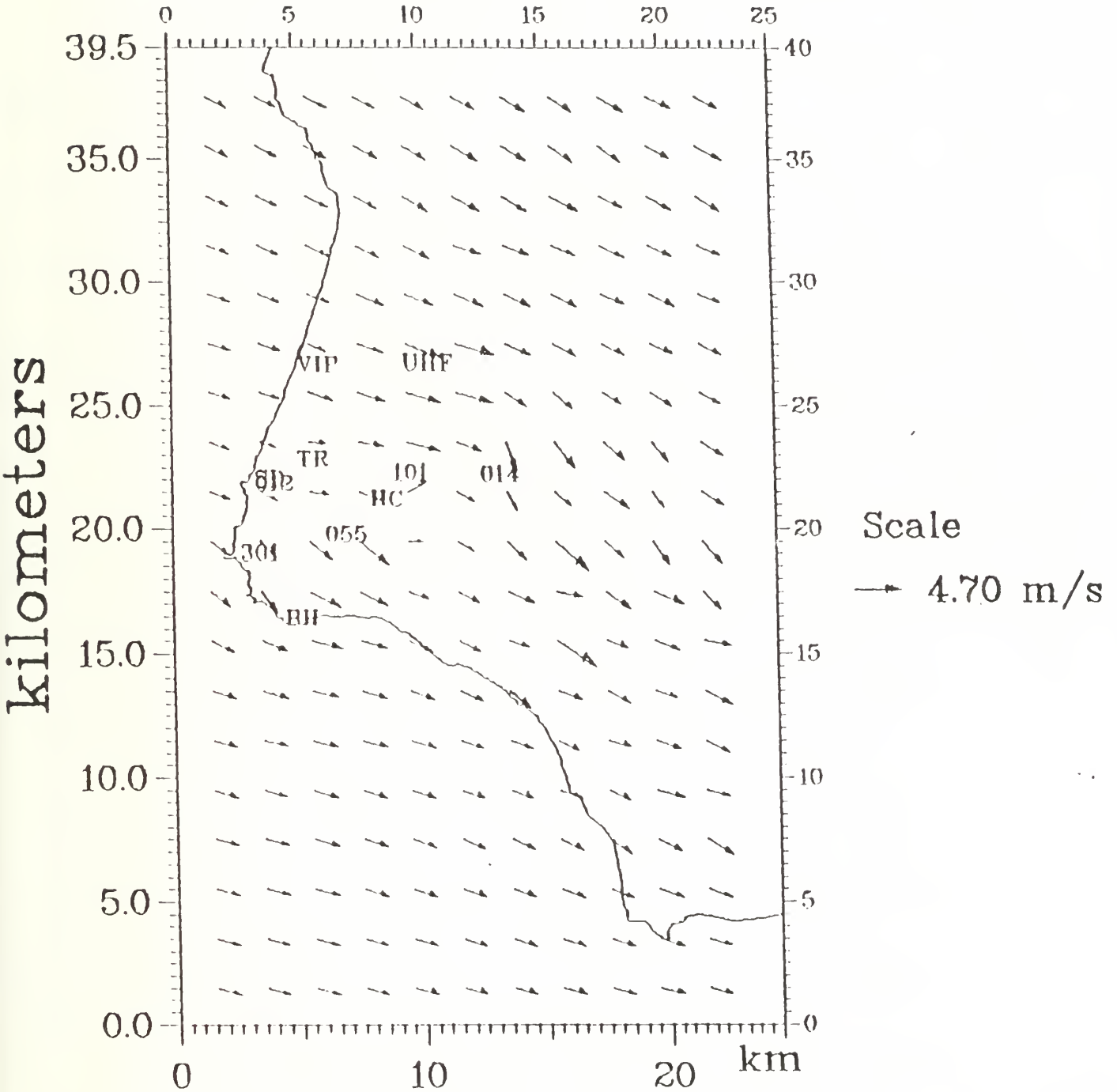

Fig. 4 LINCOM Case 28 (weak seabreeze westerly) wind vectors shown at every fourth grid point (2km). Domain is 25 x 40 km.

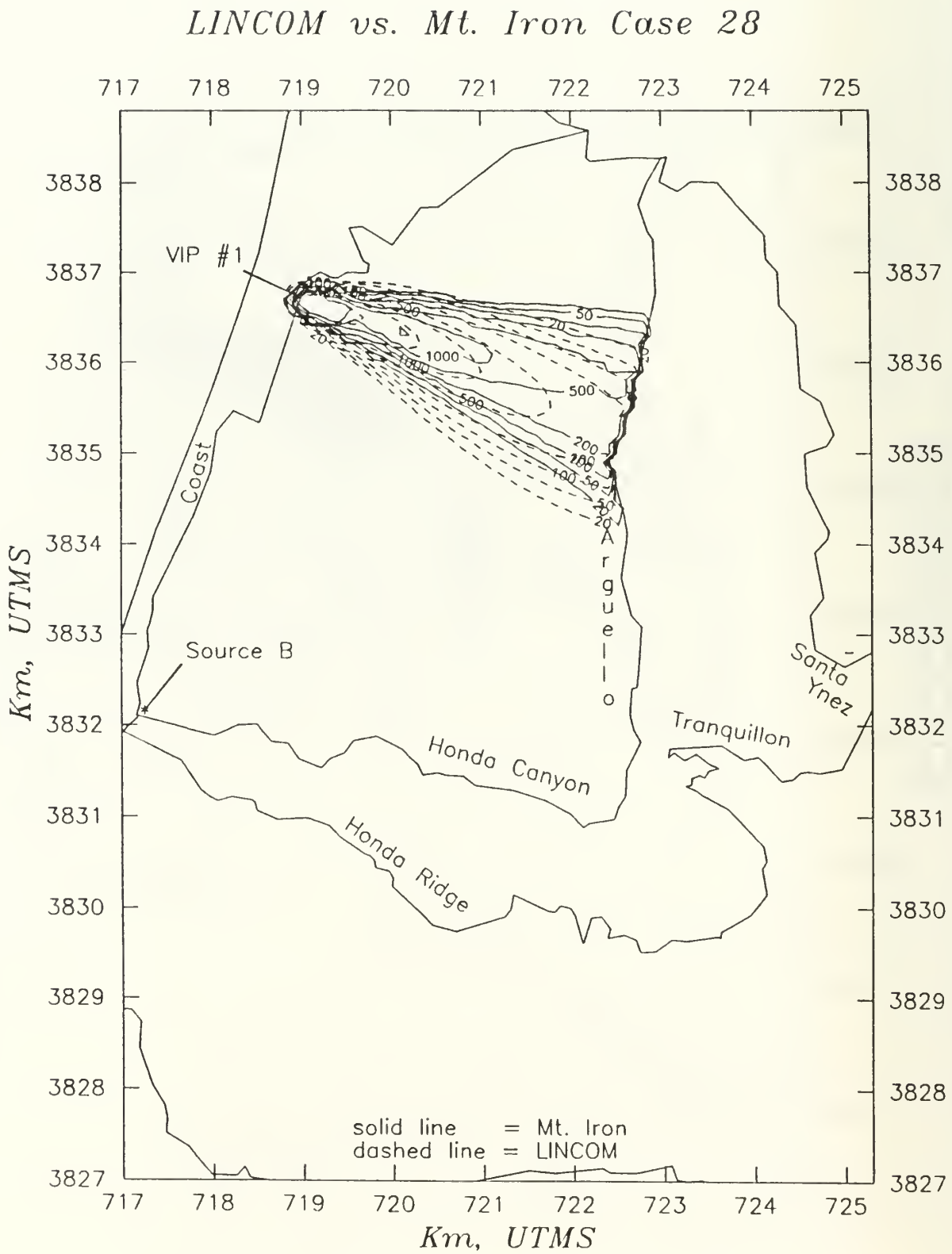

Fig. 5 LINCOM/RIMPUFF and Mt. Iron dose isopleths for Case 28 at 100m resolution. Domain is 8.4 x 11.9 km.

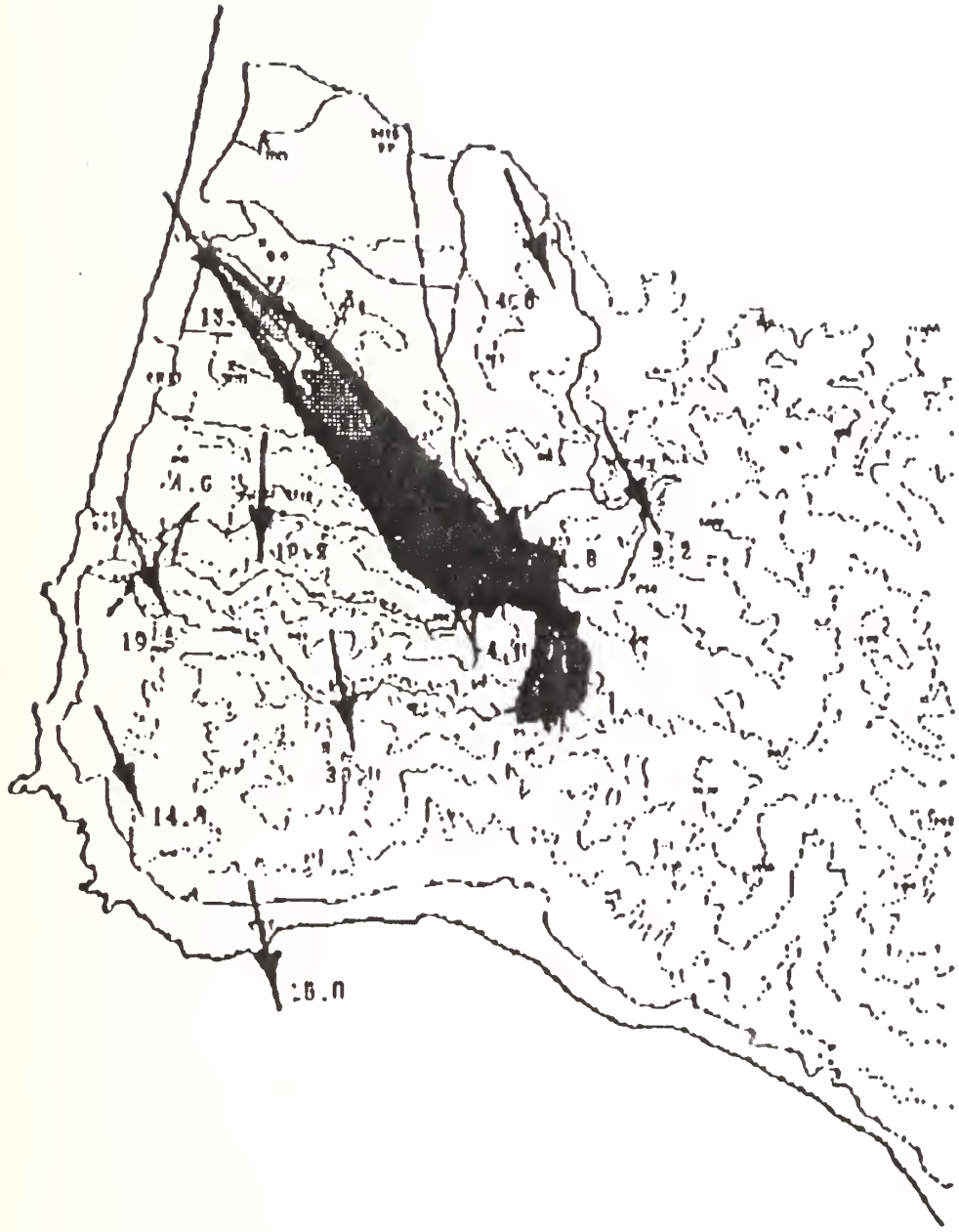

Fig. 6 Mt. Iron Case 31 plume isopleths and tower wind vectors from the Mt. Iron Report Phase I Vol. I.

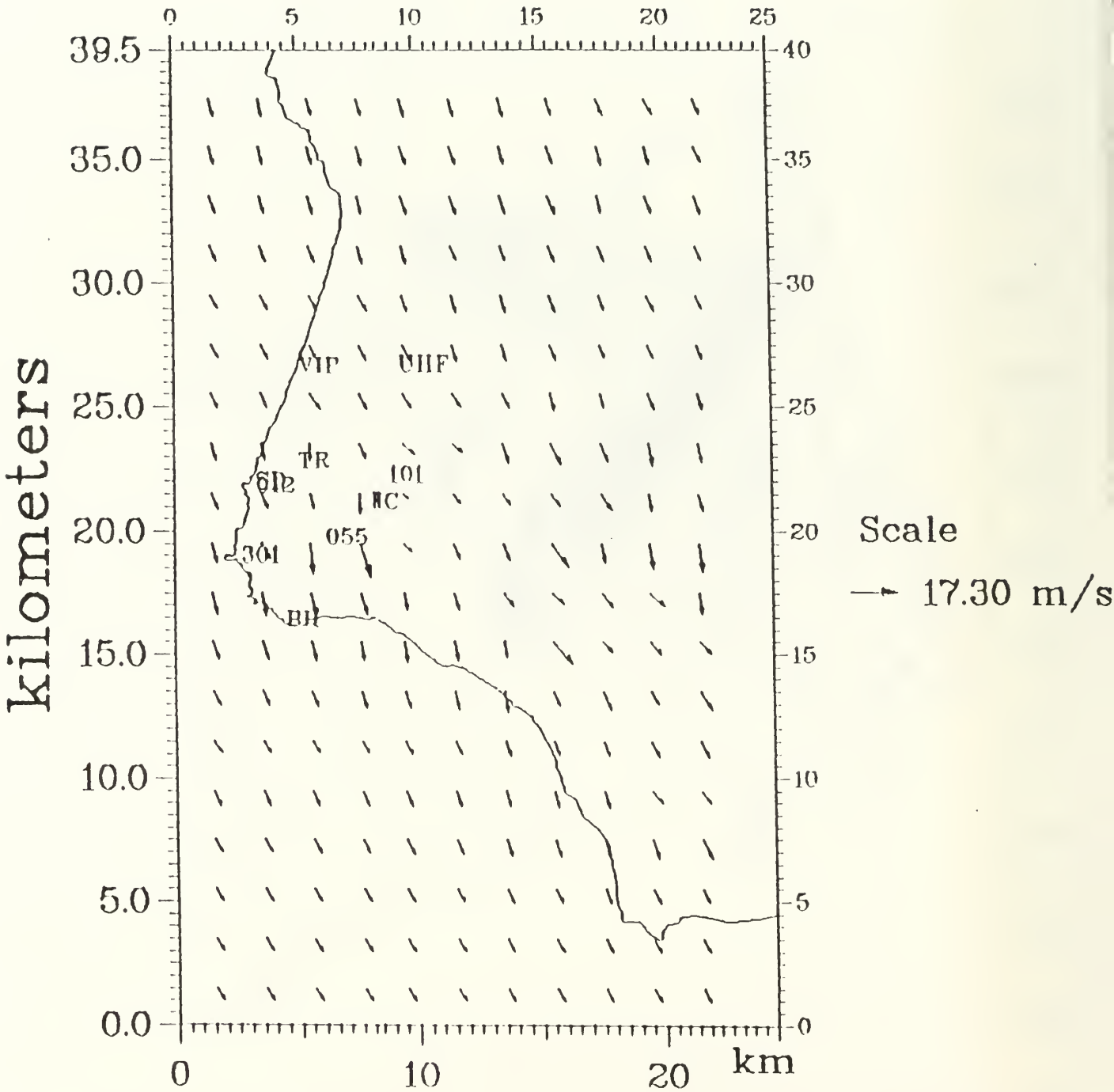

Fig. 7 LINCOM Case 31 (synoptic northwesterly) wind vectors shown at every fourth grid point (2km). Domain is 25 x 40 km.

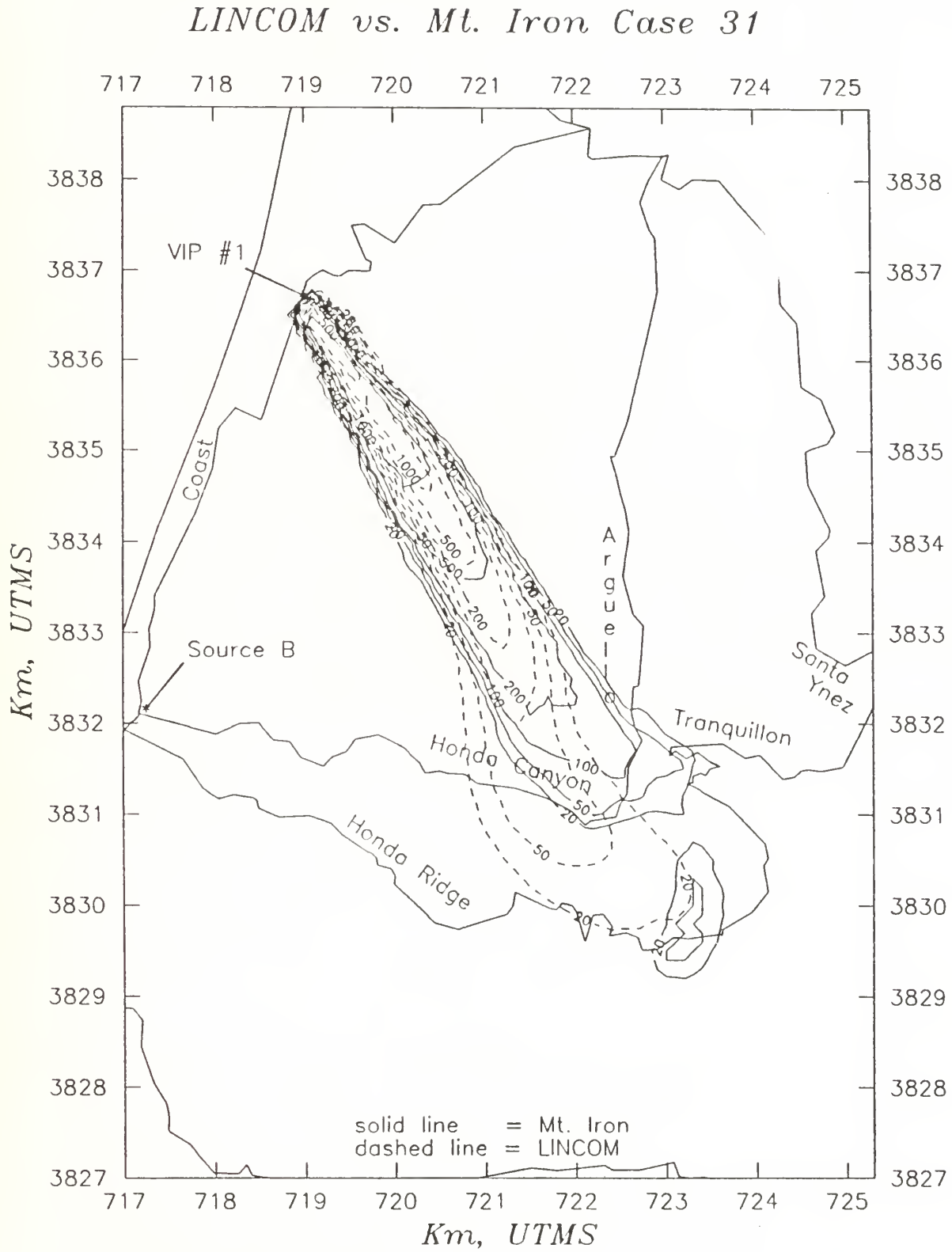

Fig. 8 LINCOM/RIMPUFF and Mt. Iron dose isopleths for Case 31 at 100m resolution. Domain is 8.4 x 11.9 km.

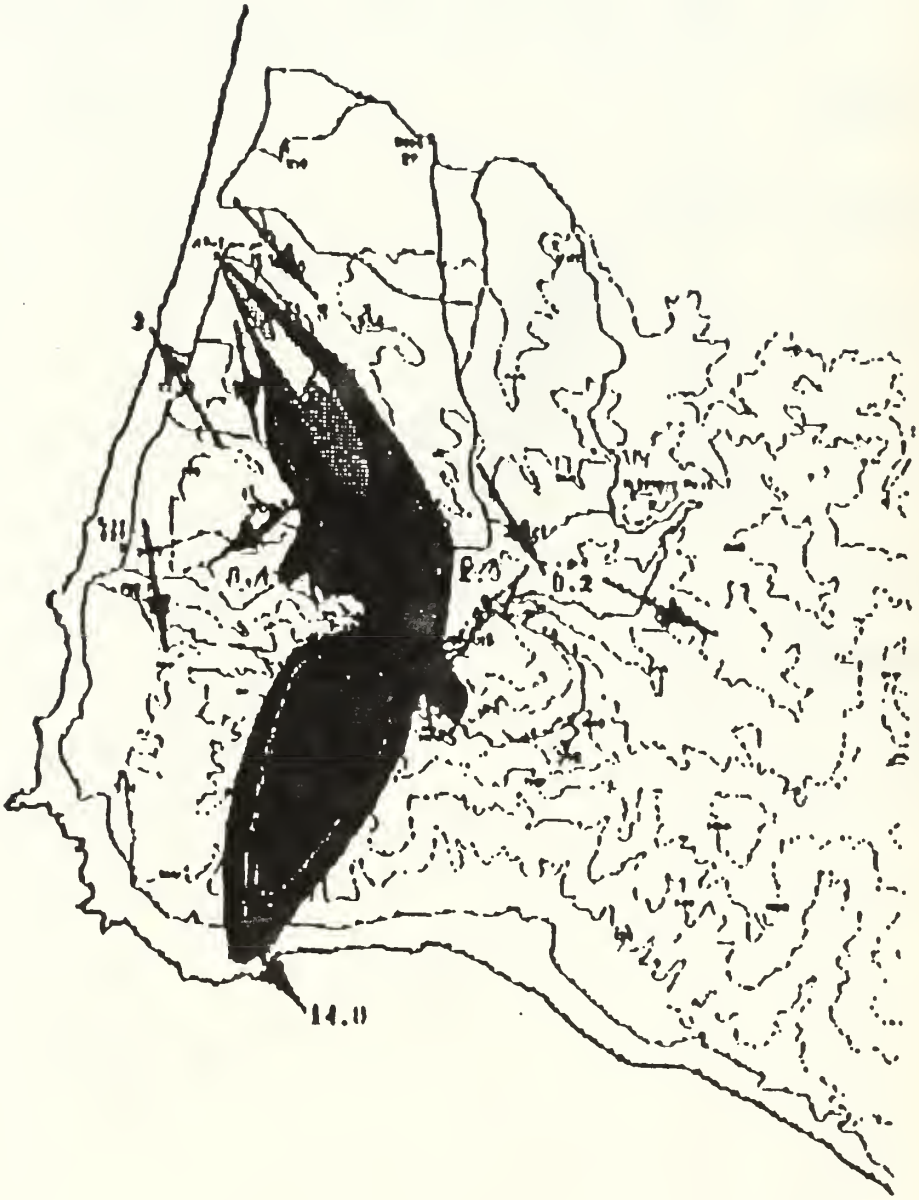

Fig. 9 Mt. Iron Case 48 plume isopleths and tower wind vectors from the Mt. Iron Report Phase I Vol. I.

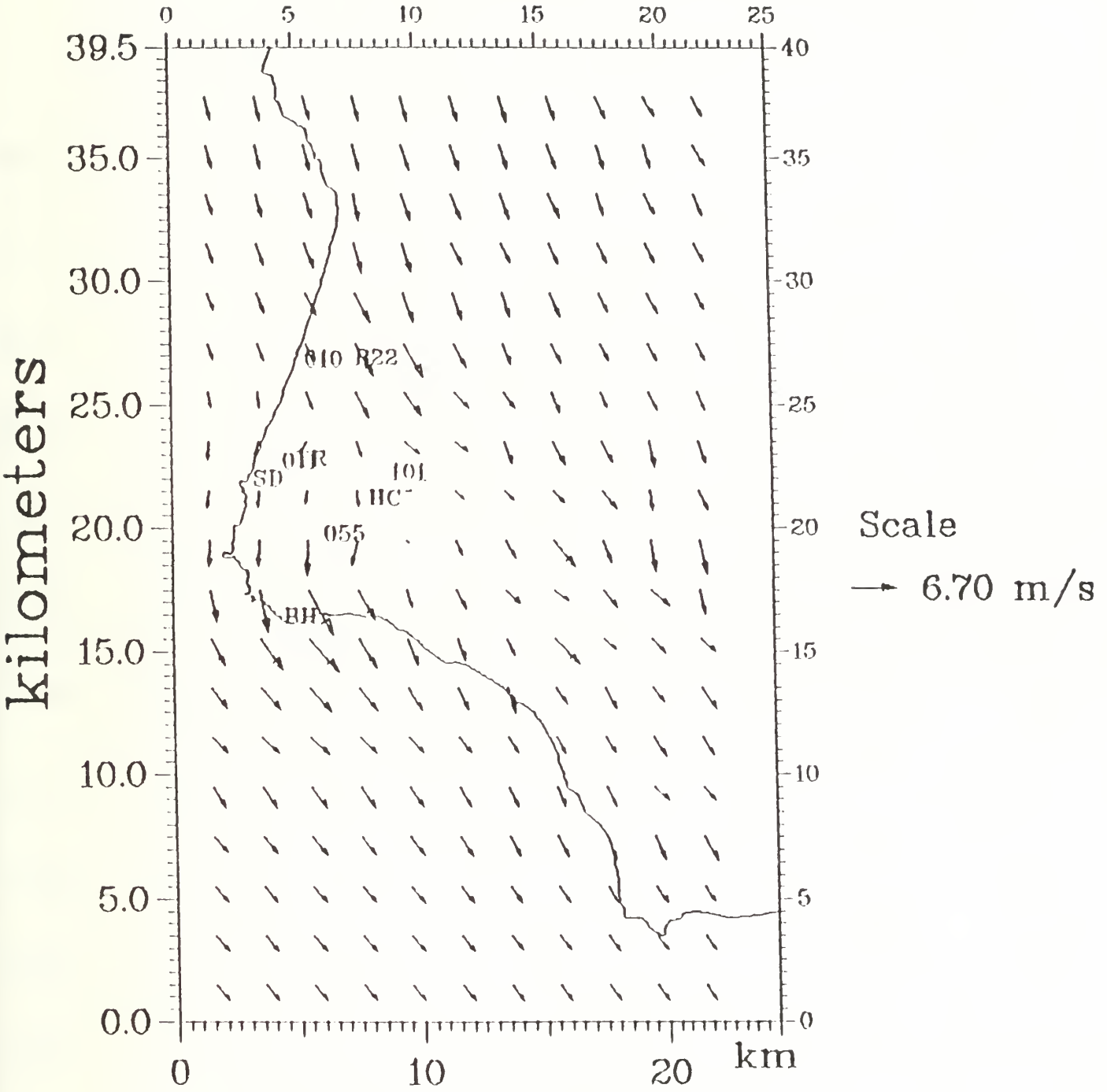

Fig. 10 LINCOM Case 48 (nocturnal drainage) wind vectors shown at every fourth grid point (2km). Domain is 25 x 40 km.

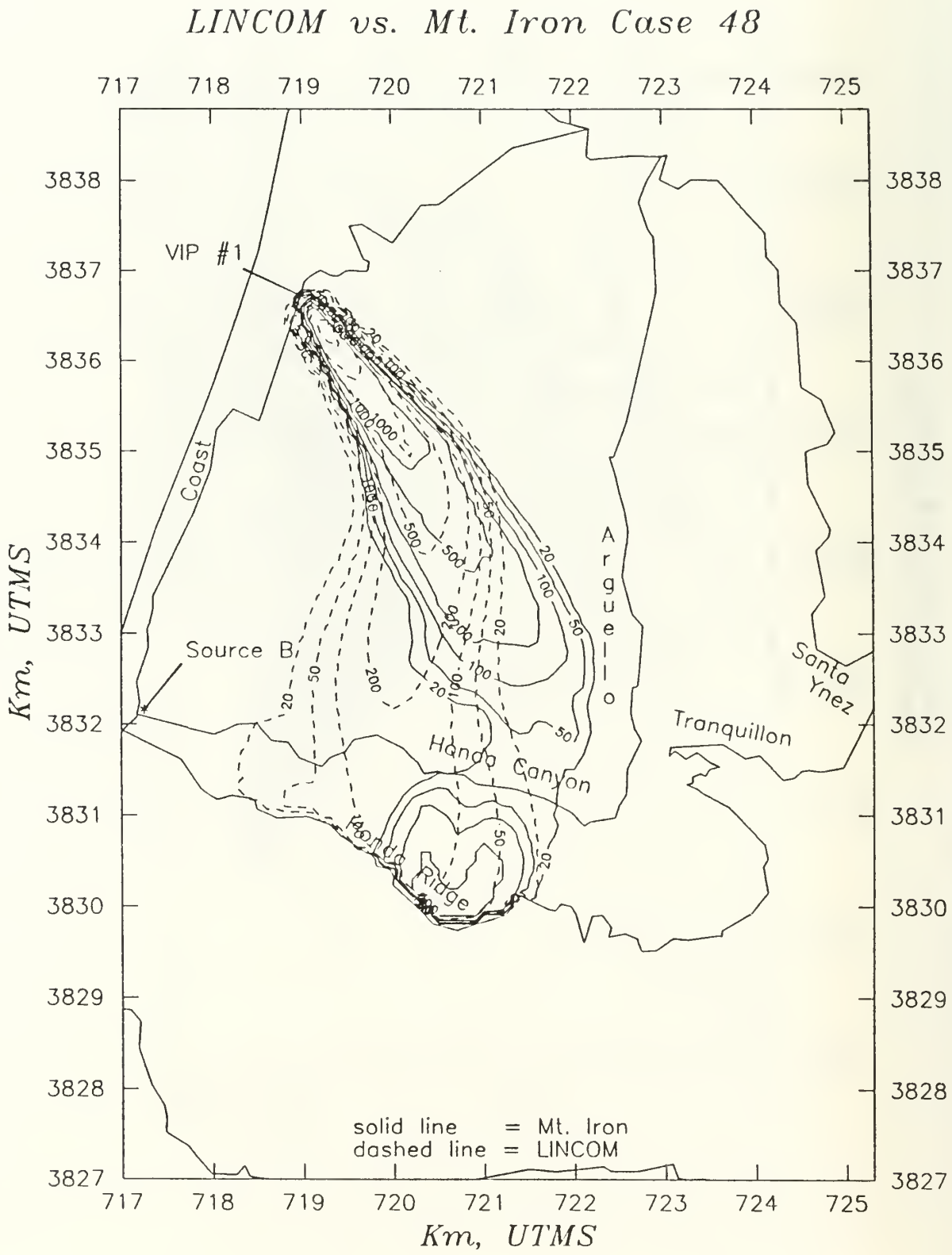

Fig. 11 LINCOM/RIMPUFF and Mt. Iron dose isopleths for Case 48 at 100m resolution. Domain is 8.4 x 11.9 km.

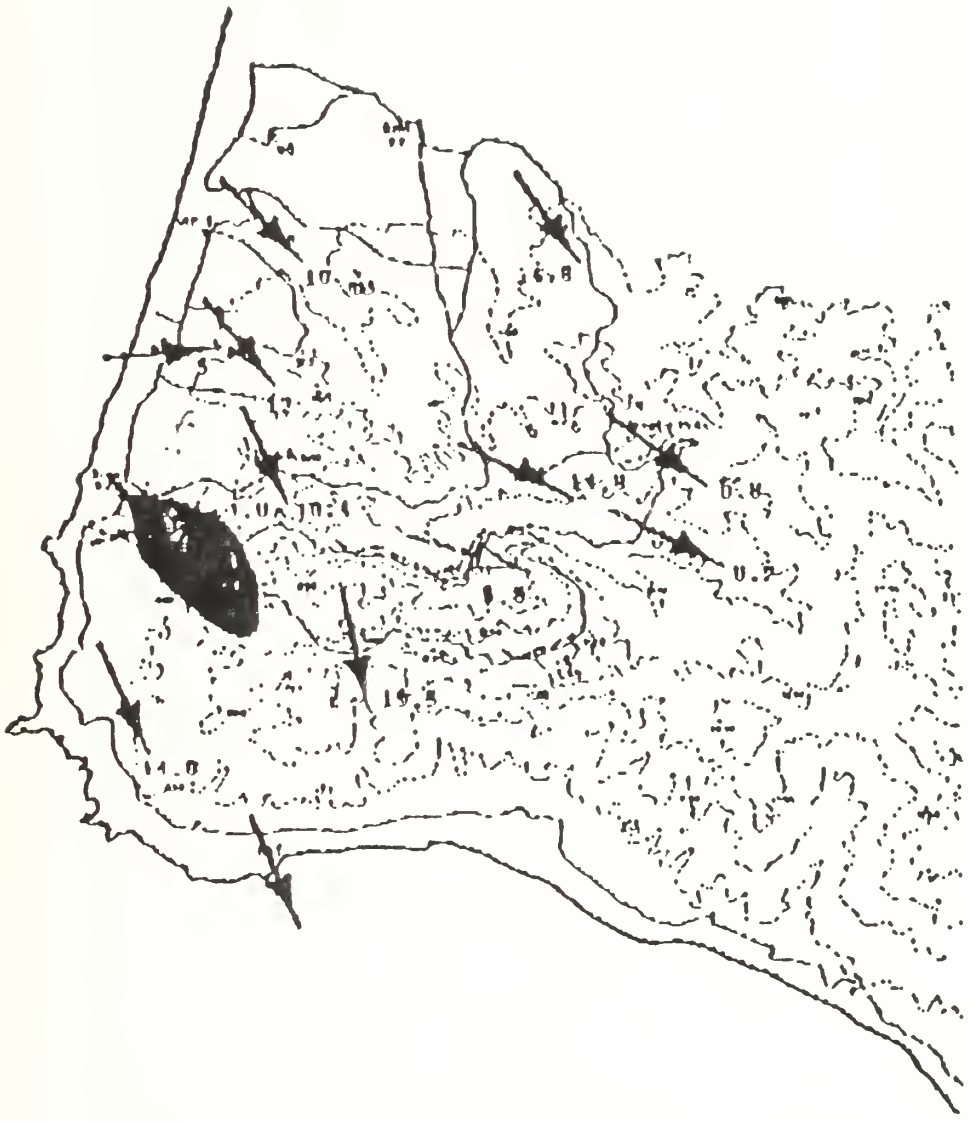

Fig. 12 Mt. Iron Case 55 plume isopleths and tower wind vectors from the Mt. Iron Report Phase I Vol. I.

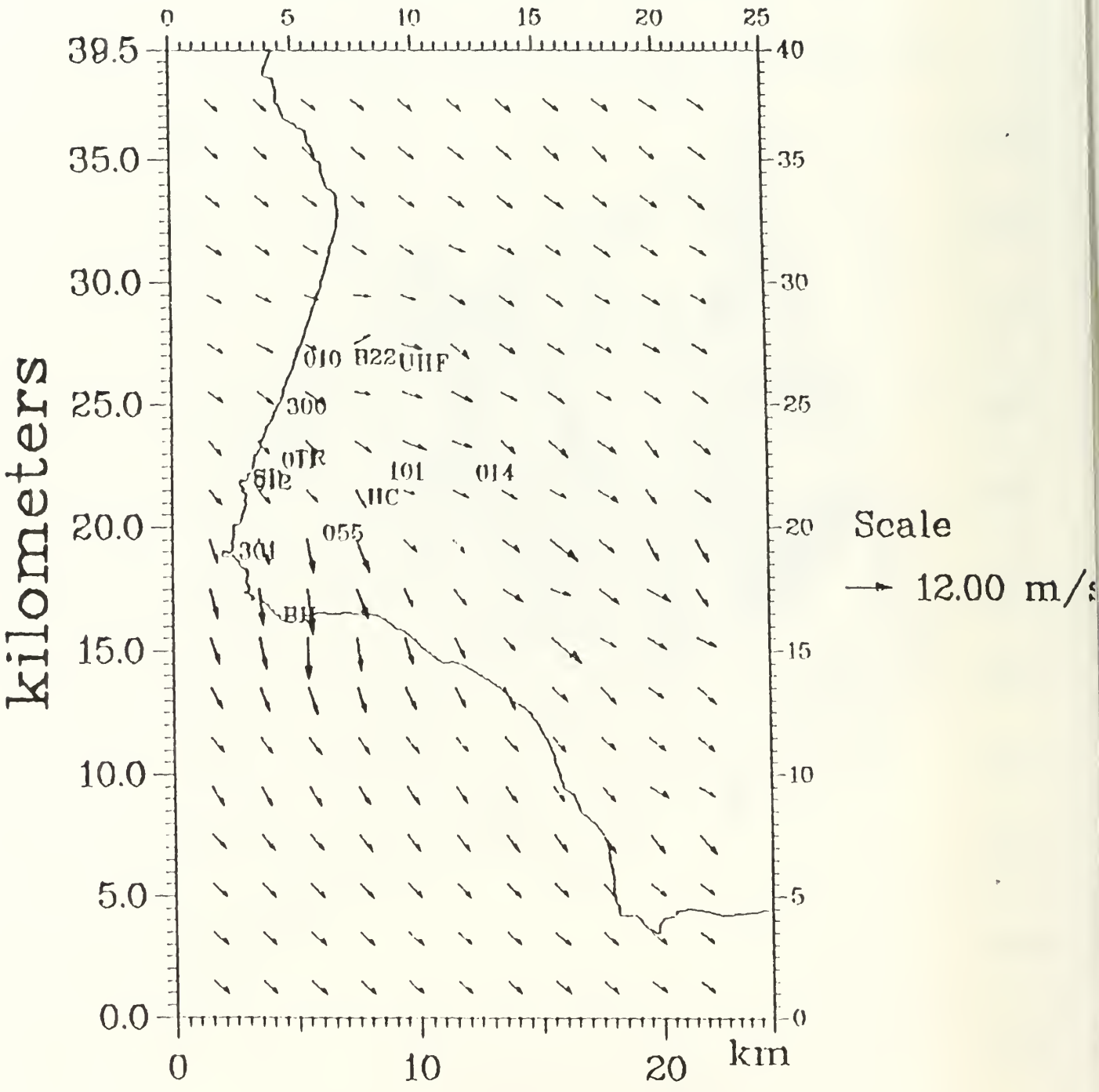

Fig. 13 LINCOM Case 55 (convective seabreeze northwesterly) wind vectors shown at every fourth grid point (2km). Domain is 25 x 40 km.

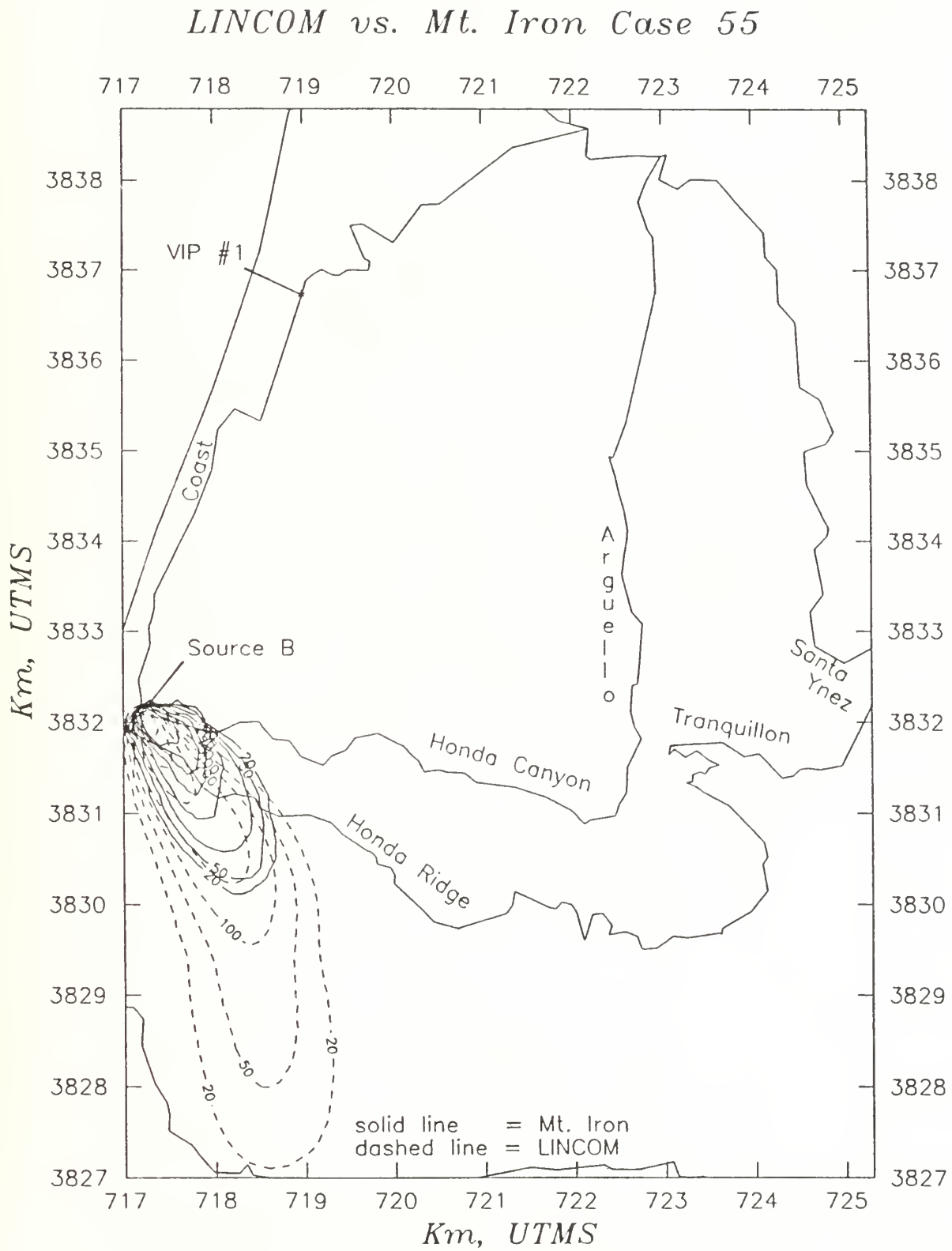

Fig. 14 LINCOM/RIMPUFF and Mt. Iron dose isopleths for Case 55 at 100m resolution. Domain is 8.4 x 11.9 km.

Fig. 15 Mt. Iron Case 87 plume isopleths and tower wind vectors from the Mt. Iron Report Phase I Vol. I.

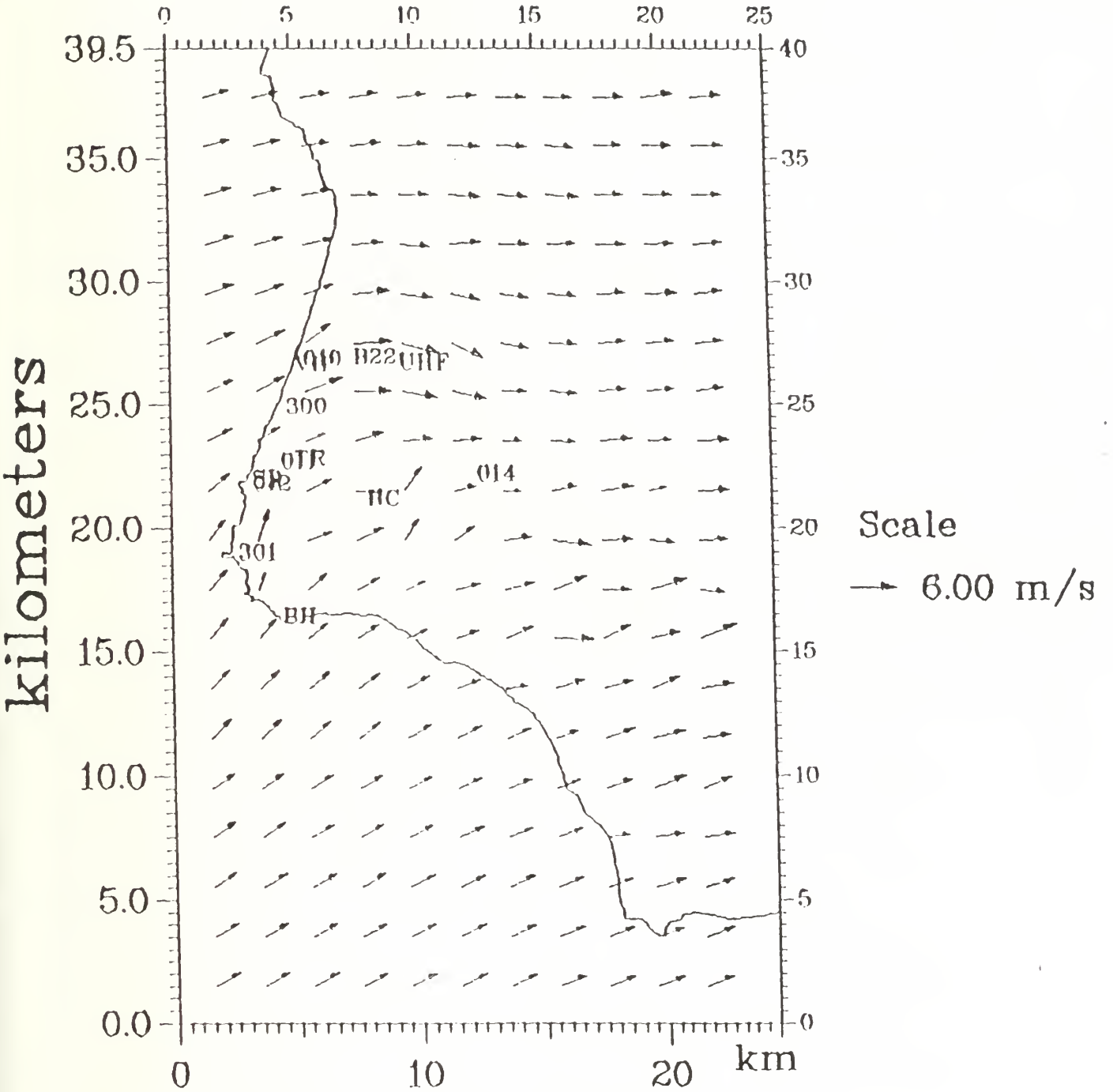

Fig. 16 LINCOM Case 87 (fog breeze southwesterly) wind vectors shown at every fourth grid point (2km). Domain is 25 x 40 km.

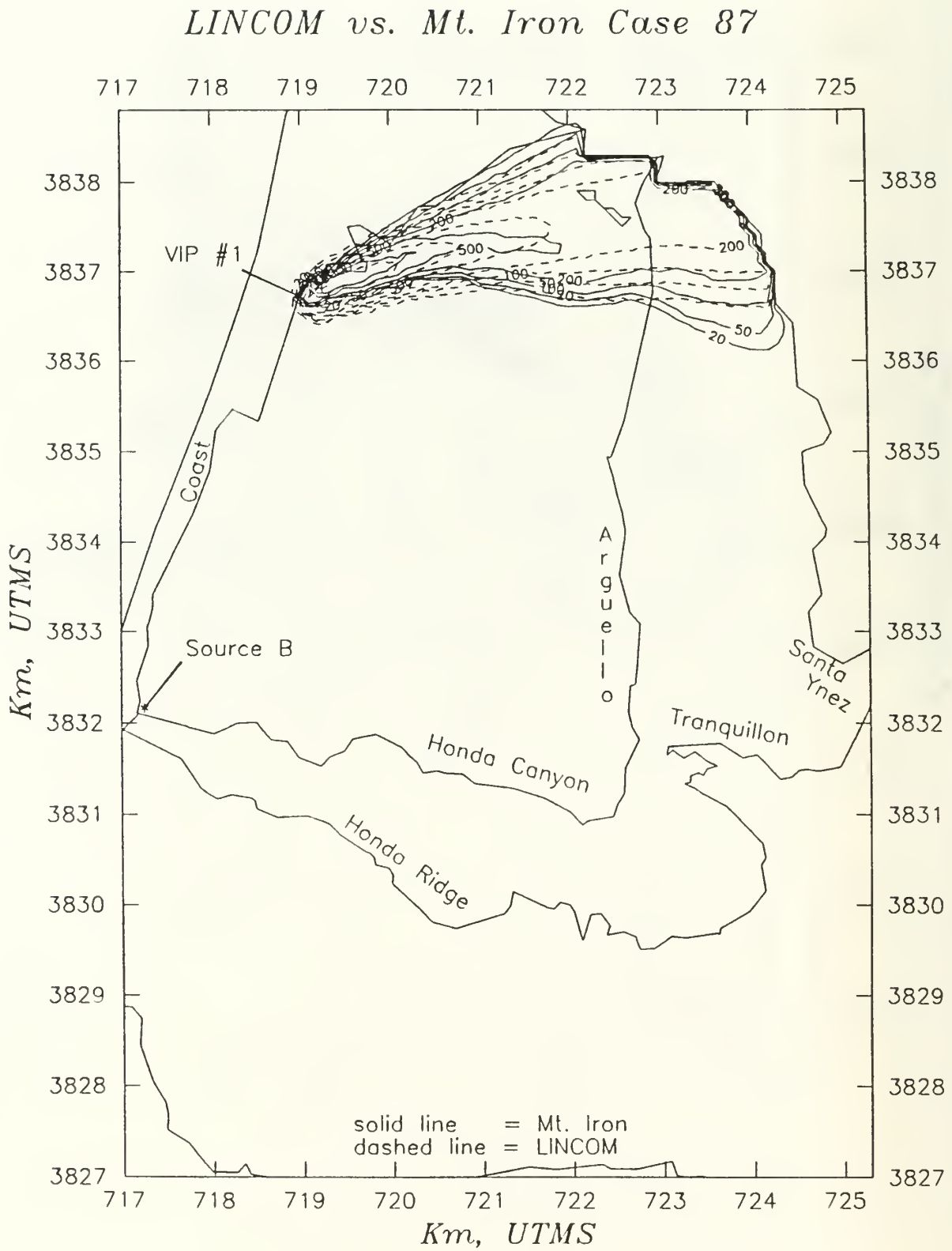

Fig. 17 LINCOM/RIMPUFF and Mt. Iron dose isopleths for Case 87 at 100m resolution. Domain is 8.4 x 11.9 km.

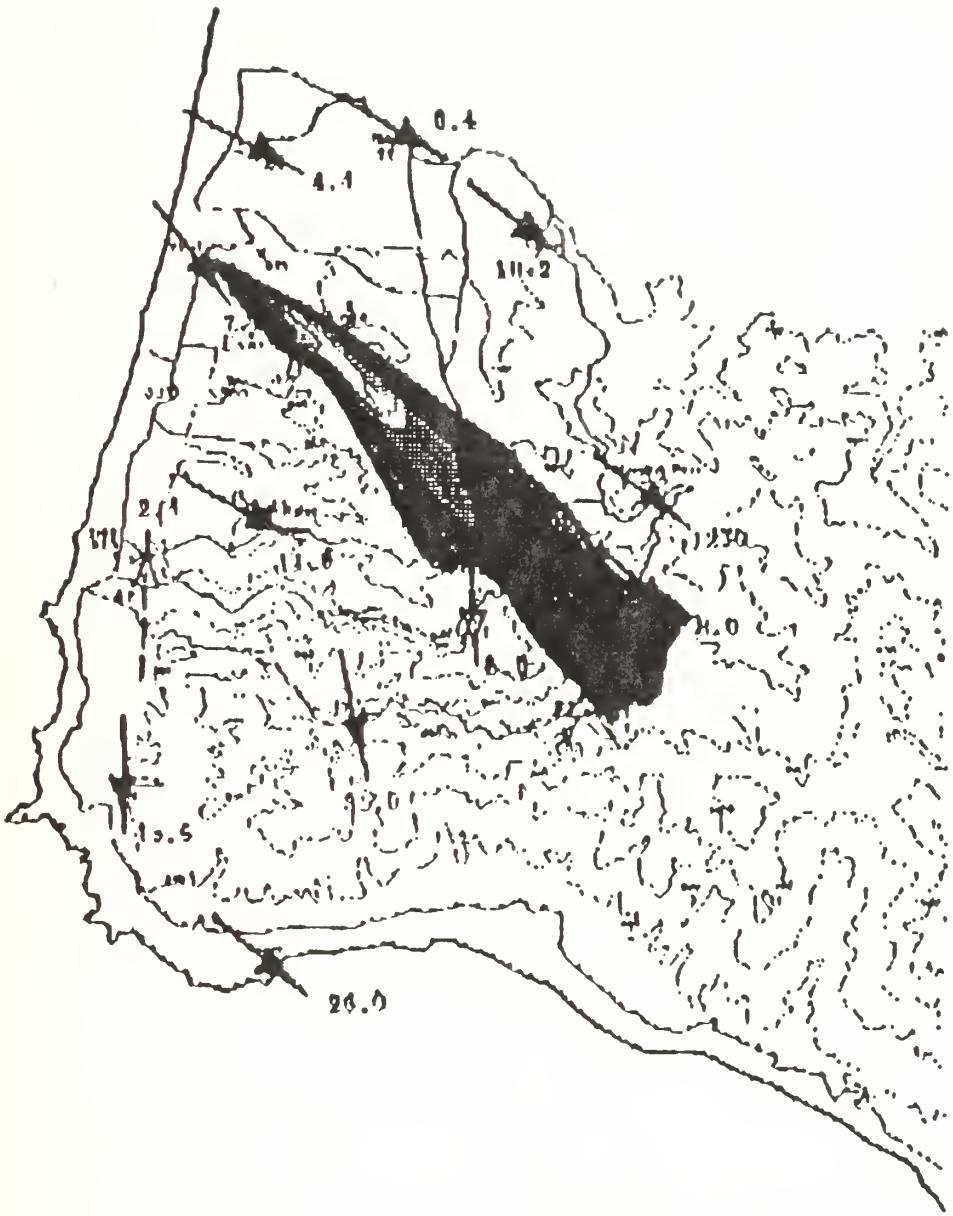

Fig. 18 Mt. Iron Case 90 plume isopleths and tower wind vectors from the Mt. Iron Report Phase I Vol. I.

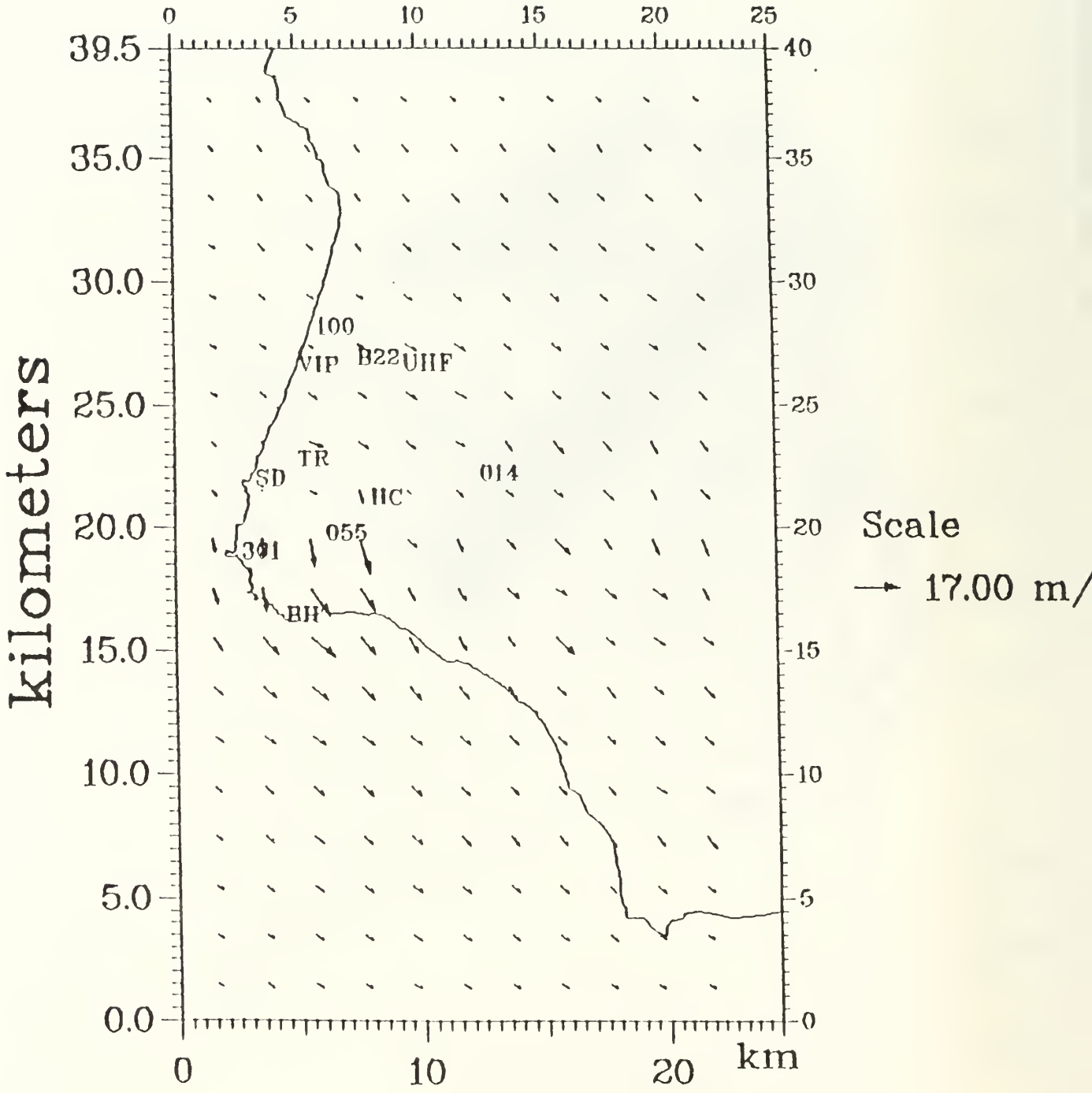

Fig. 19 LINCOM Case 90 (seabreeze northwesterly) wind vectors shown at every fourth grid point (2km). Domain is 25 x 40 km.

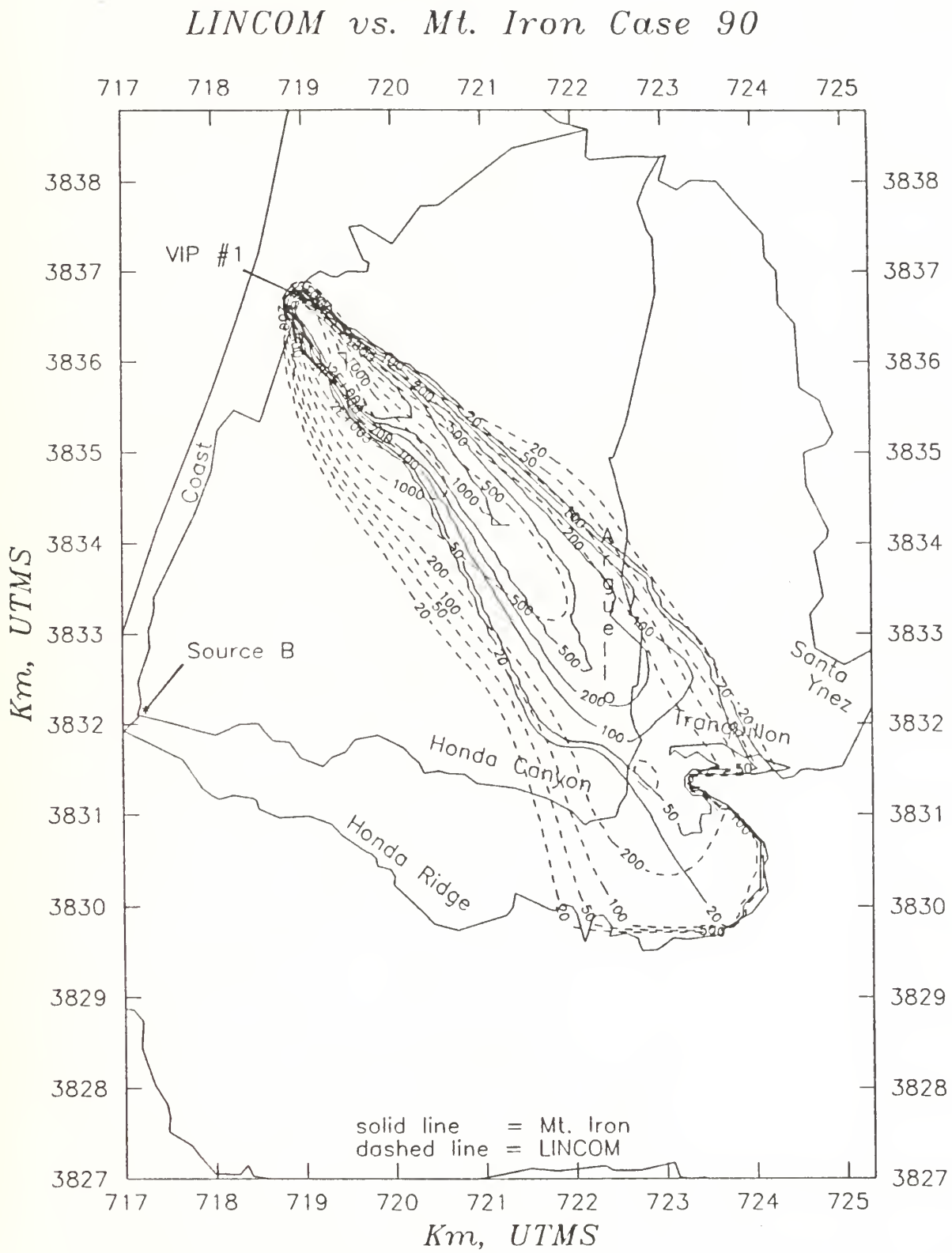

Fig. 20 LINCOM/RIMPUFF and Mt. Iron dose isopleths for Case 90 at 100m resolution. Domain is 8.4 x 11.9 km.

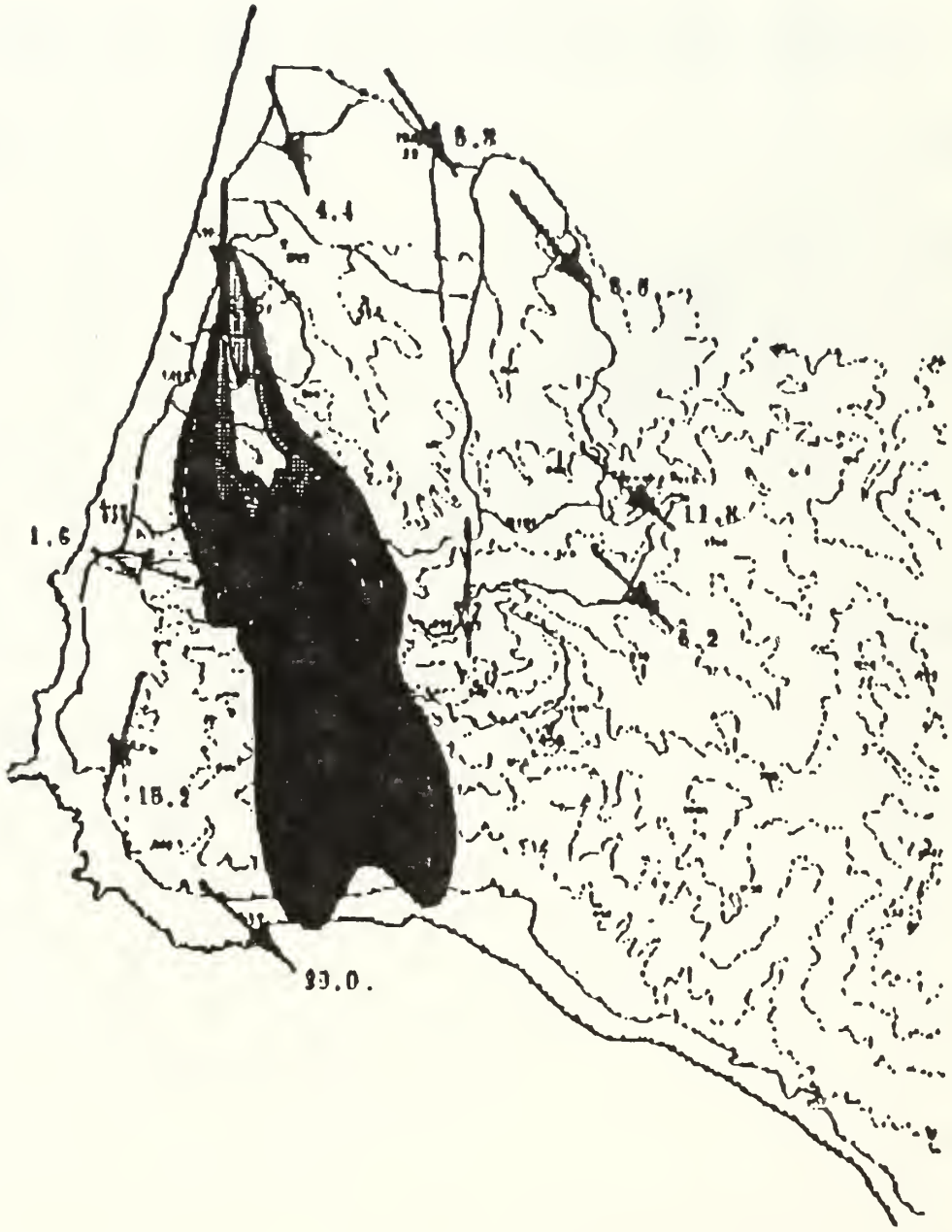

Fig. 21 Mt. Iron Case 91 plume isopleths and tower wind vectors from the Mt. Iron Report Phase I Vol. I.

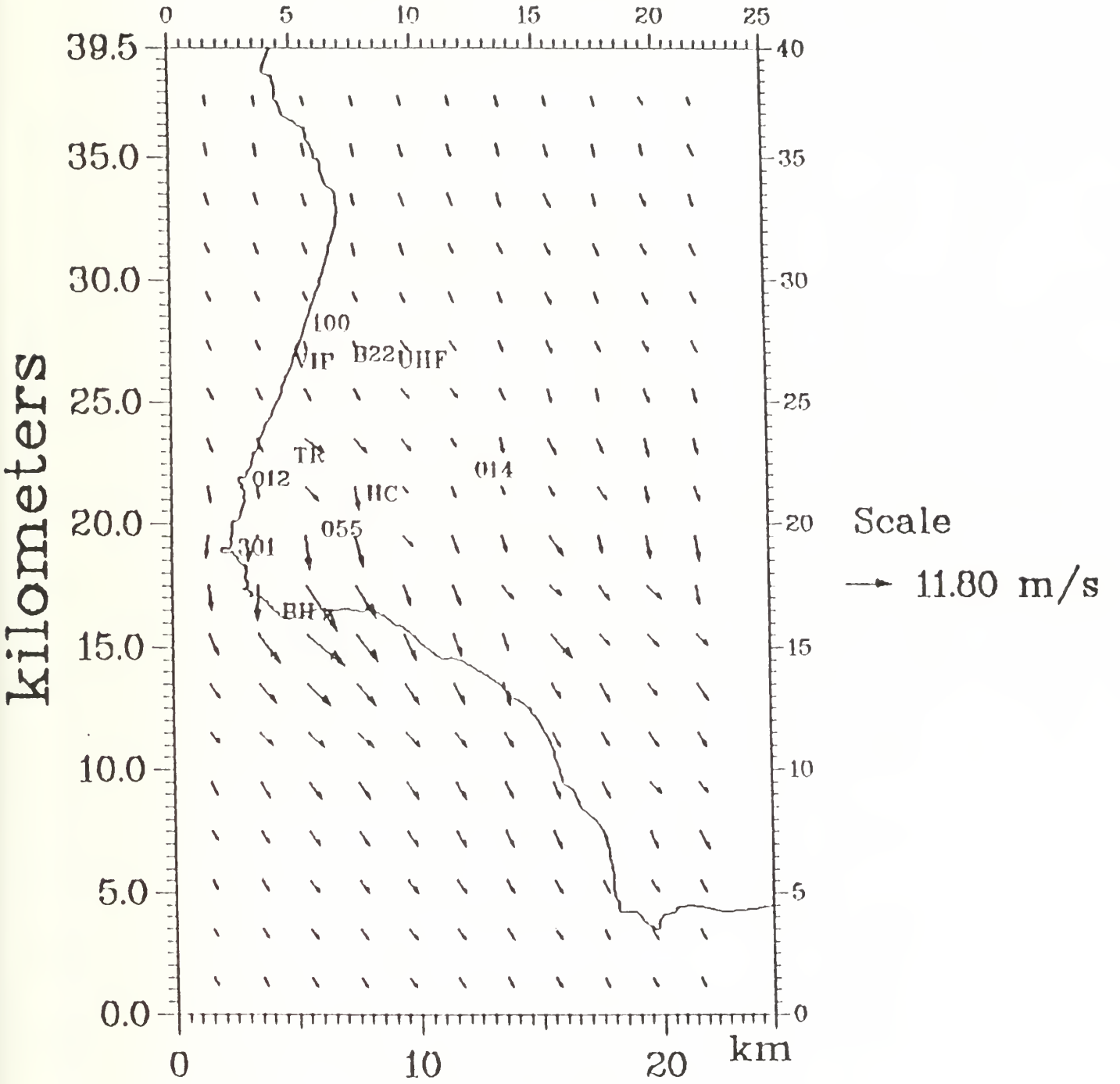

Fig. 22 LINCOM Case 91 (evening northerly) wind vectors shown at every fourth grid point (2km). Domain is 25 x 40 km.

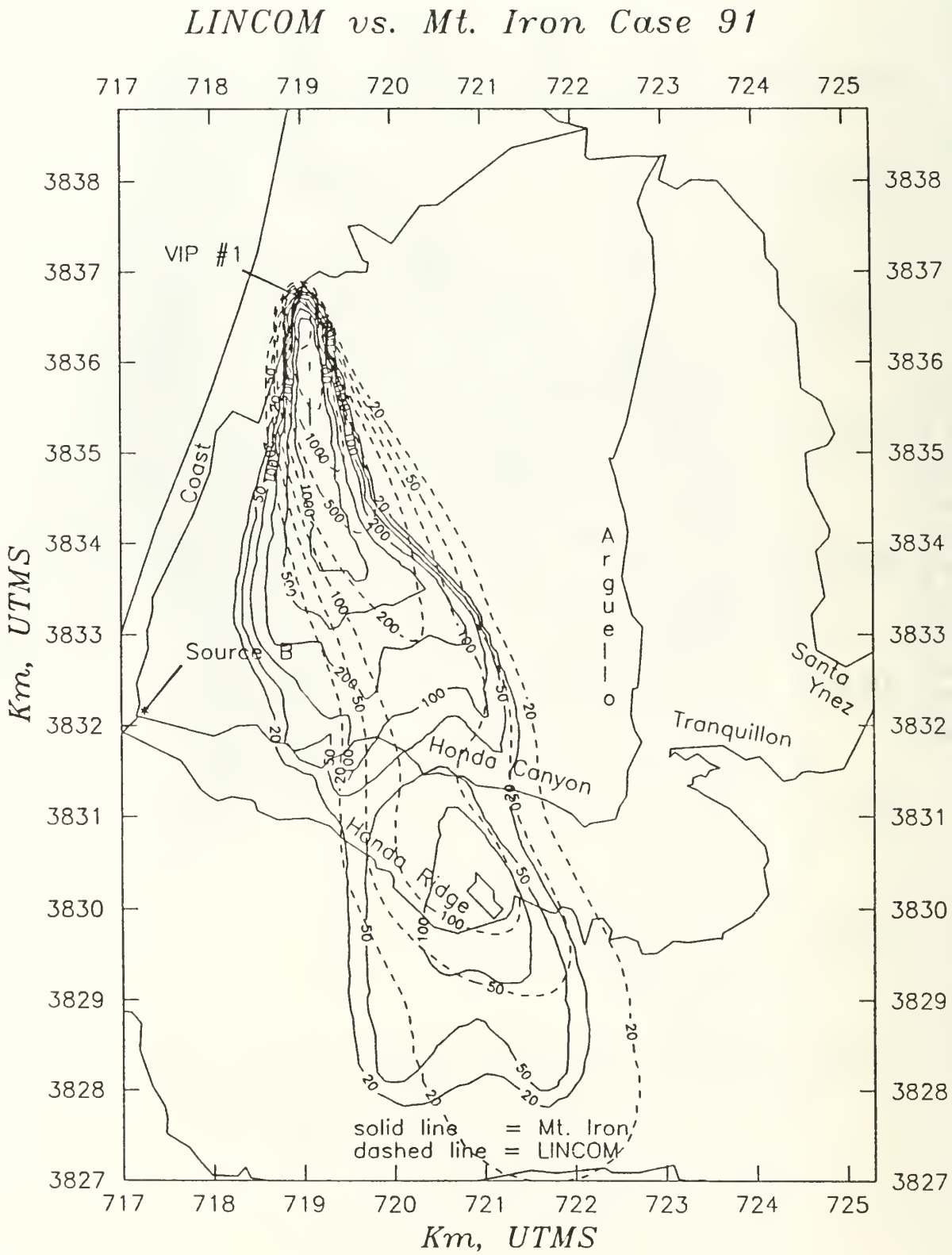

Fig. 23 LINCOM/RIMPUFF and Mt. Iron dose isopleths for Case 91 at 100m resolution. Domain is 8.4 x 11.9 km.

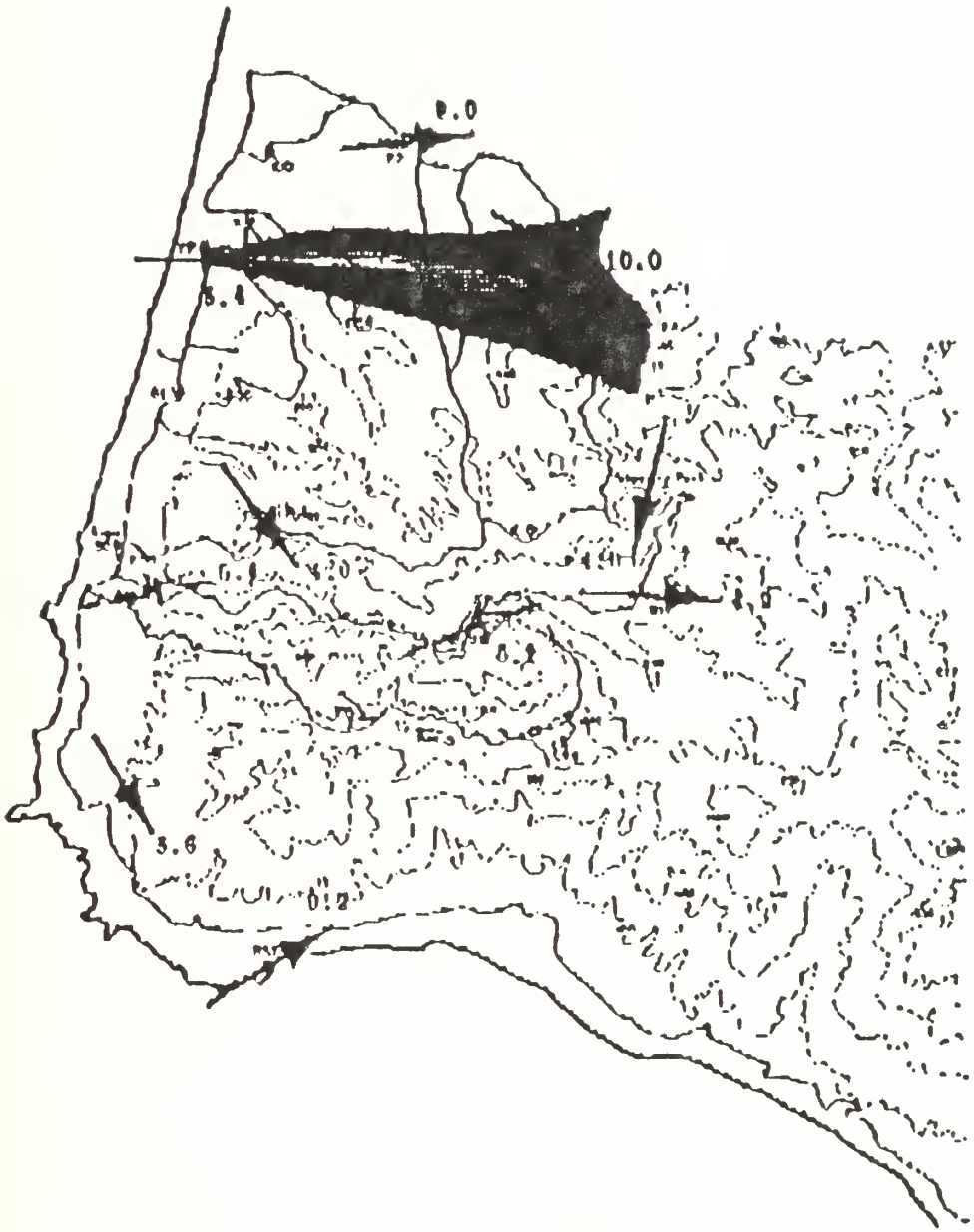

Fig. 24 Mt. Iron Case 110 plume isopleths and tower wind vectors from the Mt. Iron Report Phase I Vol. I.

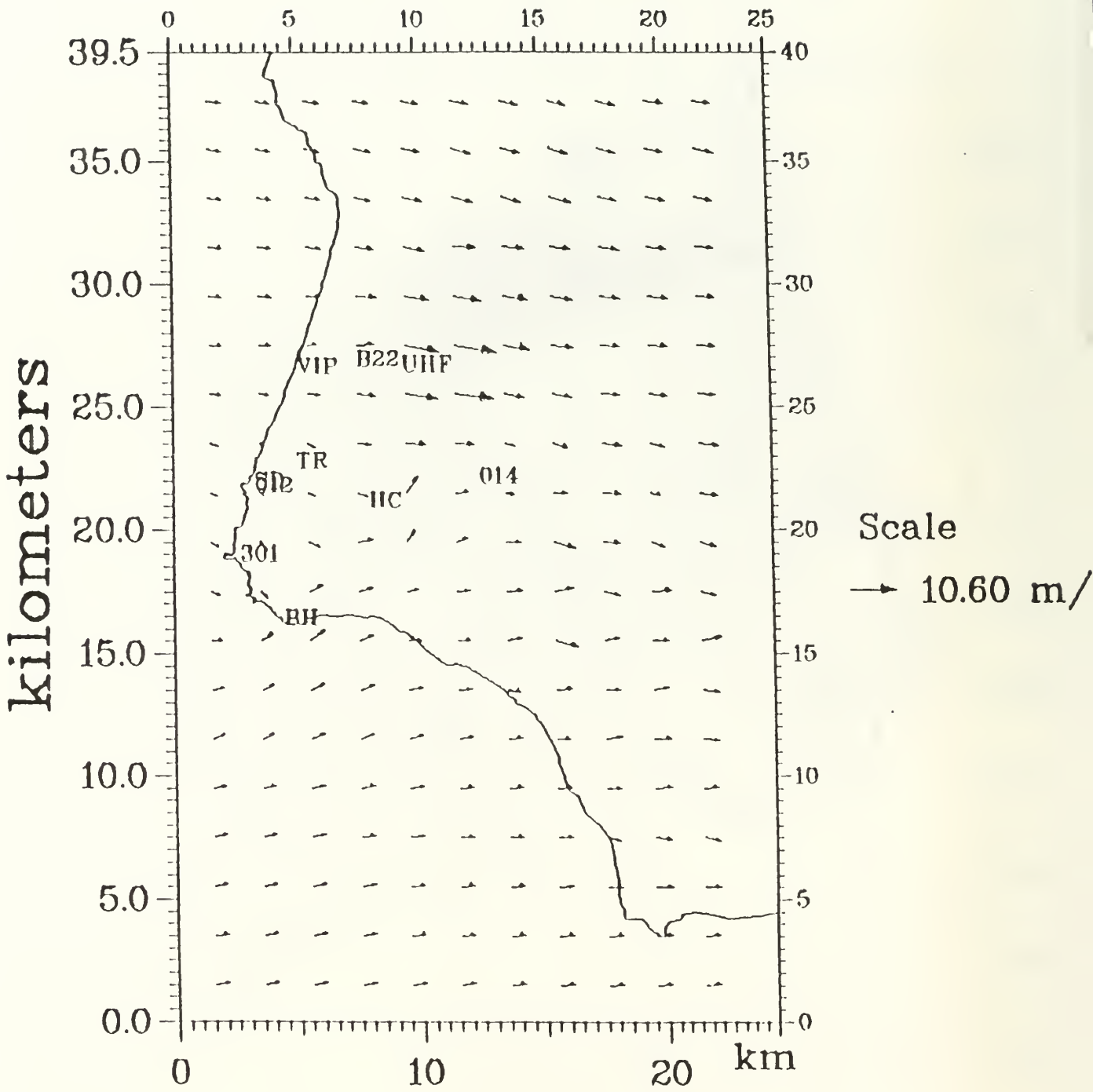

Fig. 25 LINCOM Case 110 (seabreeze weak westerly) wind vectors shown at every fourth grid point (2km). Domain is 25 x 40 km.

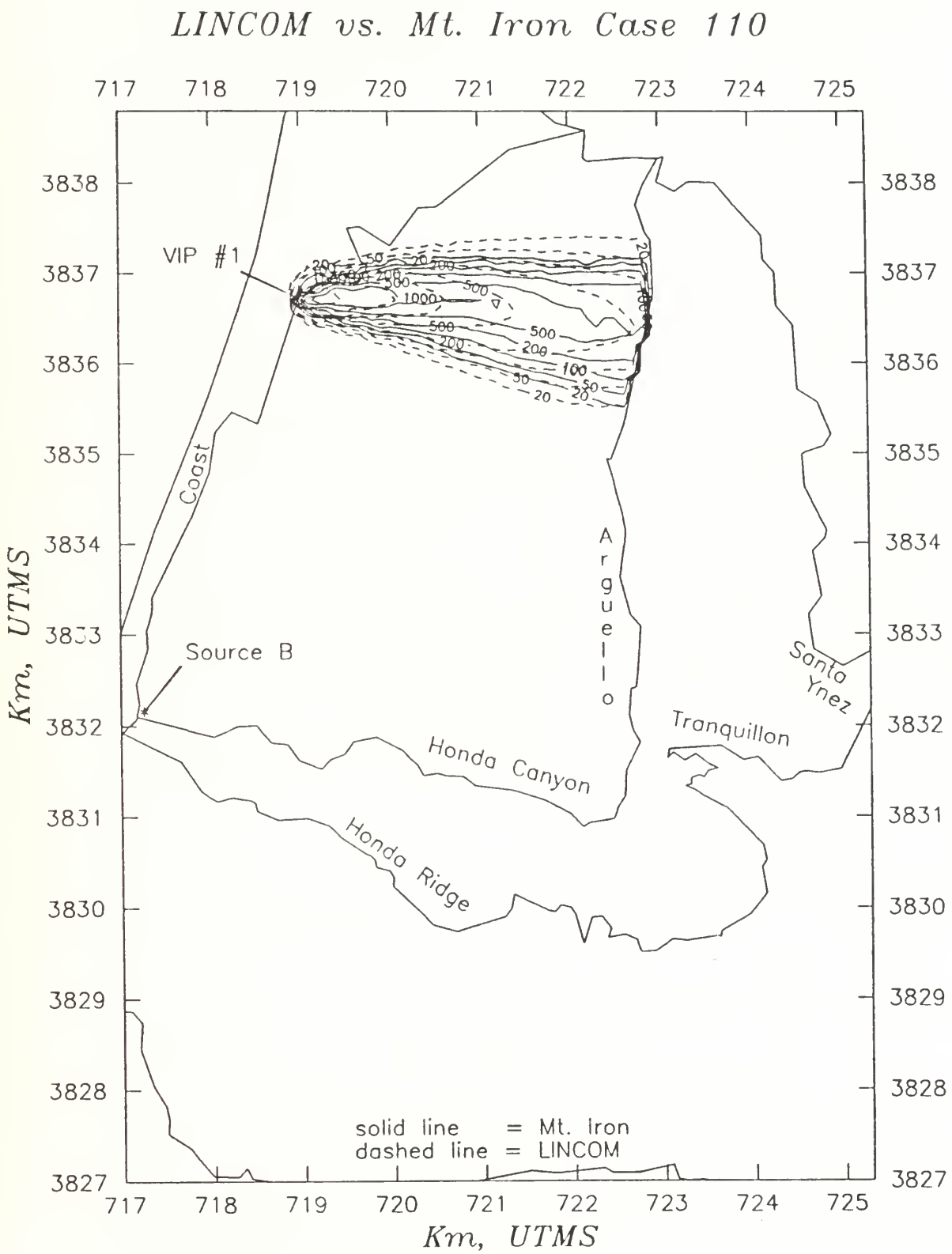

Fig. 26 LINCOM/RIMPUFF and Mt. Iron dose isopleths for Case 110 at 100m resolution. Domain is 8.4 x 11.9 km.

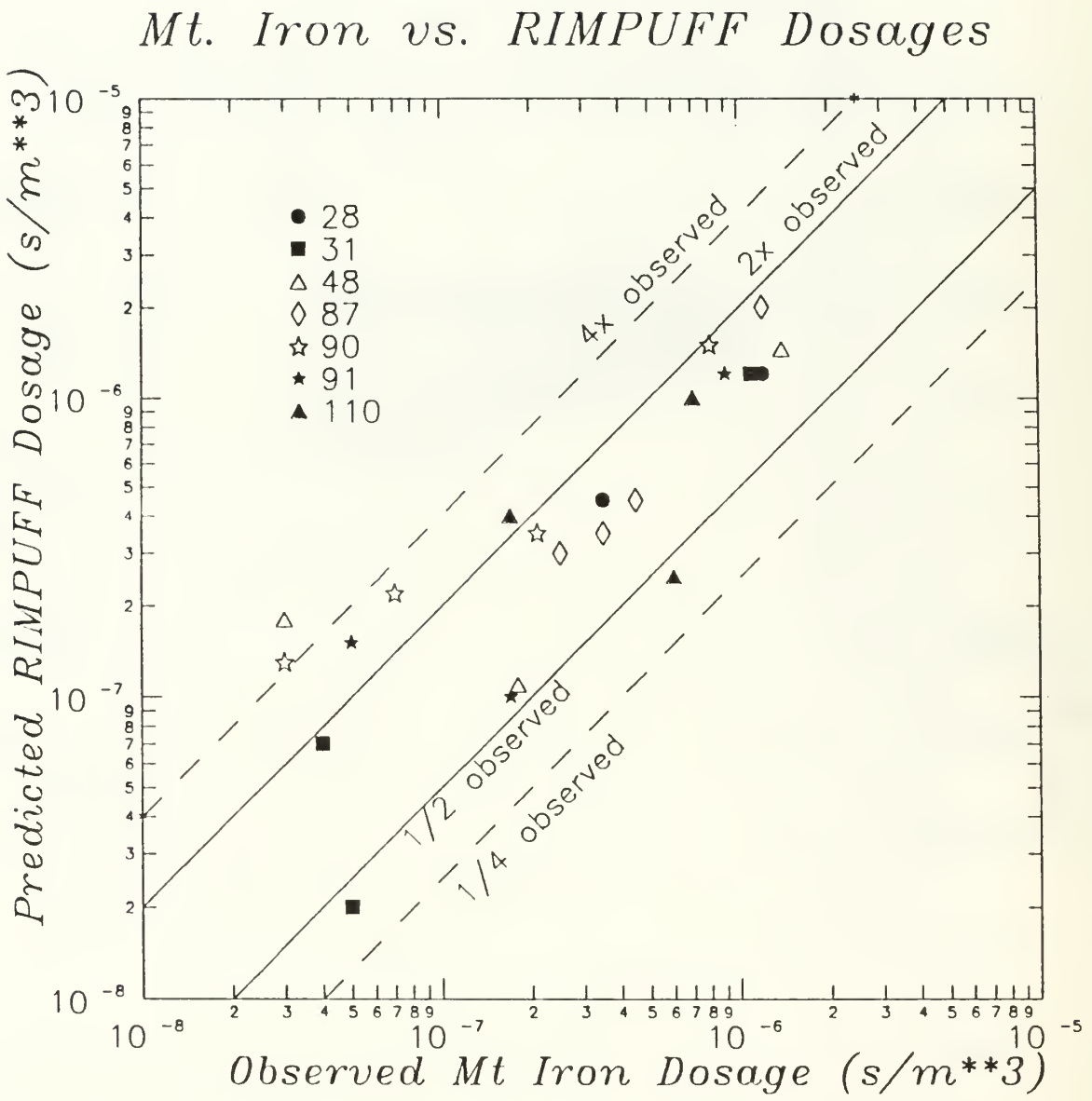

Fig. 27 Scatter plot of normalized centerline dose exposures for Mt. Iron versus LINCOM/RIMPUFF. Units are sec/m^3

5.2 Discussion of Results

As shown in figs. 3 - 18, the LINCOM generated wind fields conform quite closely to those observed. This level of conformity is not usually seen in diagnostic models and is mainly due to the "tower anchoring" feature discussed in section 3.1. Since the towers were not located at exact grid points and tower influence decays with a modified inverse distance squared, the more exaggerated flow divergence indicated by the towers is mitigated on the gridded wind field by LINCOM dynamics. However, in cases 90 and 91 this conformity becomes overzealous, since Tower 012 at the mouth of Honda Canyon was probably in error (figs. 13, 15).

As an example of the "aliasing" problem discussed in section 3.1, LINCOM is also overly influenced by towers at the bottoms of canyons where the winds are very locally controlled but do not conform to the bulk of the boundary layer flow. The imposition of strict mass conservation as in LINCOM 1.1 should retain the main flow features but would not resolve the local flows. In fact, tower observations will generally suggest more flow divergence than is displayed in modeled wind fields because the tower winds respond to all forcings, including the ones that are of smaller scale than the model grid resolution such as turbulence and very local terrain.

This leads to a partial dilemma for tracer studies in hilly, complex terrain. As at Vandenberg, available roads for fixed or mobile samplers are often along the bottoms of canyons. If the canyon transects the plume, canyon samples often will show wider plume widths, reflecting the tendency for local along-canyon flow (see LVDE, 1991). However, most of the plume will be relatively unaffected and float over such canyons. Without very high resolution and complete prognostic dynamics, numerical models may not agree well with data when the sampling does not conform to the bulk of the flow. Of course aircraft data would tend to mitigate this sampling flaw.

The height of the inversion base is another important influence on the flow field. LINCOM/RIMPUFF assumes that the inversion base parallels the terrain. For daytime unstable conditions, this is a reasonable assumption as shown in Kamada et al (1990). However, local inversion height changes are suggested in cases 48 and 90, (see section 2.4). A lowered inversion may be responsible for the high winds seen at the Boathouse in case 90 (fig. 13). The inversion base may also be somewhat flatter than terrain parallel under neutral or mildly stable conditions. These features require a complete physics package and cannot be resolved by the dynamics of simpler diagnostic models. On the other hand, in this case the "tower anchoring" feature in LINCOM assists modeling accuracy in the winds south of Honda Ridge, in spite of the crude inversion height assumption.

Figs. 19 - 26 and the corresponding DICA, FB, and NMSE scores suggest that LINCOM/RIMPUFF matches the Mt. Iron isopleths fairly well, except for case 55 where the DICA score falls below 0.2. However, the fractional biases indicate that the LINCOM/RIMPUFF plumes are longer than Mt. Iron in seven of the eight cases. I.e., doses are higher than those measured at longer downwind ranges, particularly cases 28, 90, and 110, where FB are less than -0.4, even though downwind ranges for the higher dose isopleths are quite comparable. This is in keeping with the AFTOX/Mt. Iron and WADOCT/Mt. Iron comparisons of plume centerline dosages (Kunkel and Izumi, 1990; Kunkel, 1991). It is also consistent with the LVDE results.

As in the above reports, we suggest that the zinc sulfide wet aerosol tracer was not physically inert as previously assumed, but probably was gradually adsorbed into the ground canopy as the plume was advected downwind. This is consistent with oral reports that by the conclusion of the Mt. Iron releases, pools of dried tracer material surrounded the release sites.

For most cases, the DICA and NMSE scores yield parallel results. For instance, case 87 shows the best fit with both methods. However, the DICA and NMSE scores diverge for cases 31, 90, and particularly 91. The NMSE was much higher for case 91 than the other cases, even though the DICA and FB scores were fairly good. As in 31 and 90, the NMSE in case 91 involves a large number of points (column 2 of Table 5.1.1). However, both the measured and simulated average dosages are low (columns 3 and 4), as is the total error (column 5). But the NMSE is large here because the dose average is so small. Case 90, with a much larger average dosage and error, has a much smaller NMSE. This suggests that normalizing the error by the average isopleth value may skew the results to favor cases with large average dosages, despite having large errors prior to normalization.

On the other hand, the DICA algorithm does not seem to suffer from this problem. It sorts the LINCOM/RIMPUFF model results for the eight cases in much the same order as derived by a qualitative visual inspection, but more accurately. For example, a visual inspection (Fig. 23) suggests that case 87 shows the best fit. It also has the highest DICA score; case 55 (fig. 22) shows the worst fit and lowest DICA score. However, it is difficult to distinguish case 87 from 110 or to compare two rather different cases, such as 28 and 91, for congruence by eye, while DICA does so easily. Given these strengths, we suggest that DICA be utilized as a standard performance measure where applicable.

Save for cases 55 and 90 (figs. 22 and 24), the modeled plume thicknesses are comparable to the Mt. Iron estimates. In cases 55 and 90 RIMPUFF overestimates the lateral dose footprint. 55 is a special case discussed in more detail below. However, we suspect that the problem in case 90 stems from underestimating the vertical

diffusion. Wind/temperature vertical profiles for case 90 suggest near neutral conditions with significant mechanical turbulence. For such conditions, RIMPUFF's vertical turbulence parameterization will tend to underestimate the extent of the shear based turbulence. In general, it is also hard to assure accuracy for tower based temperature profiles on a routine operational basis, due to the need for frequent, precise sensor calibrations. Perhaps the surface radiation (rather than profile based) stability algorithm in LINCOM 1.1 should be used in RIMPUFF as well.

Whereas the releases were nearly point sources, in each case the modeled plume head appears thicker, due to the initial 100 meter puff diameter. A smaller initial puff diameter could have been used. So this is not a wholly necessary model artifact. Part of the extra thickness is also due to the interpolation routine used in the plotting program, as seen from the increased thickness in interpolating the hand drawn Mt. Iron plots. However, the higher valued dose isopleths are generally broader in RIMPUFF than the hand drawn isopleths. This is not as true of the lower valued dose isopleths, since diffusion decays exponentially with distance.

We also see that whenever the plume passes over Honda Canyon, substantial deviations between the modeled and hand drawn isopleths can result. The modeled winds are influenced by towers located at the bottom of Honda Canyon, while in cases 31, 48, 90, and 91, much of the real plume seems to have floated above and beyond the sampling lines at the bottom of the canyon. The LINCOM/ RIMPUFF tandem cannot reproduce the local minimum dosage values seen in these cases at the bottom of Honda Canyon. Kunkel (1990) reports a similar modeling constraint for the WADOCT model. Without non-hydrostatic capability, i.e., both buoyancy and acceleration in the vertical momentum equation, neutral LINCOM's ability to simulate the vertical divergence indicated by these cases is quite limited. For example, the hydrostatic version of HOTMAC/RAPTAD also did not reproduce the local minimums seen in cases 90 and 91, even though HOTMAC does include buoyancy in its vertical momentum equation (Yamada and Bunker, 1991). It may be that resolutions higher than 500m are also required to show such effects.

On the other hand, cases 31, 48, and 90 (figs. 20, 21, and 24) probably indicate aliasing in LINCOM 1.0. Presumably, the mass conservation integral to LINCOM 1.1 and the inclusion of buoyancy in LINCOM 2.0 should improve the simulation in such cases.

Perhaps roughly 80% of the accuracy in plume dispersion estimates depends on accurate initial wind directions. For example, case 28 shows that a few degrees error (or perhaps real wind shift) in specifying wind direction can lead to substantially lower DICA and higher NMSE values.

The effect of downwind towers cannot be ascertained for the weak

westerly and southwesterly seabreeze cases: 28, 87, and 110 (figs. 19, 23, and 26), due to the lack of data beyond the sampling line at Arguello Rd. and consequent truncation of the plumes.

For case 55 (fig. 22) the LINCOM/RIMPUFF plume is much longer than the measured one. As discussed in the case flow analysis of section 2.3, a convective cumulus condition with vigorous updrafts is indicated by the unstable lapse rates, high mid-April inversion, and patchy cloud cover over neighboring sites in Honda Canyon and Scout D. Thus, the plume may simply have lofted and dispersed over unsampled areas. Or a sustained local downdraft may have forced adsorption into the canopy. The former interpretation is probably more likely.

There are data problems which render the scatter diagram in fig. 27 less meaningful than is immediately apparent. 1) Since we compare only eight cases, there are only twenty-two valid data points. 2) Only the hand-drawn isopleths were available, rather than actual bag sample exposure levels. Hence, non-linear interpolation was needed to obtain actual values. 3) The sampling lines for Mt. Iron were along accessible roads rather than concentric circles. Thus, it was sometimes difficult or impossible to compare modeled and measured values when the centerlines diverged in direction. 4) Figure 19 seems to coincide with the fractional bias results which show that the RIMPUFF predictions are higher than those observed at lower dosage levels; actually, the predicted centerline dosages are higher mainly only in Honda Canyon.

6. SUMMARY AND CONCLUSIONS

Results from the LINCOM/RIMPUFF dispersion model were compared with eight representative cases from the Mt. Iron tracer study conducted at South Vandenberg AFB during 1966. We conclude that:

1) The LINCOM wind fields conform fairly closely to observations due to "tower anchoring". Tower anchoring allows LINCOM to retain complex flow features which would otherwise require the use of a higher resolution, non-hydrostatic prognostic flow model with a complete physics package. However, this feature is a mixed blessing when local towers misrepresent the main flow. For tracer studies, this points to the need for aircraft sampling in addition to ground sampling to determine local as well as bulk flow features.

2) Plume simulations based on LINCOM/RIMPUFF compare fairly well with Mt. Iron, but the modeled plumes are generally somewhat longer, as is consistent with other published reports. Perhaps part of this is due to some adsorption of the zinc sulfide wet aerosol onto the vegetation canopy during transit.

3) Four indicaters were used to compare the modeled dispersion

pattern with observations. The most useful appear to be scores from the dose isopleth correlation area (DICA) method and the fractional bias (FB). We also used the normalized mean square error (NMSE) and a centerline scatterplot comparison. The NMSE seems to suffer from a tendency to overweight errors when dosages are relatively low. The centerline scatterplot involves too few data points and suffers the effects of some other Mt. Iron data idiosyncrasies discussed in section 5.2.

4) Lateral plume thicknesses compare fairly well with those observed, except perhaps when turbulence intensities were miscalculated, due to observational error, limited spatial resolution, or deficiencies in the turbulence parameterization algorithms.

5) The low dosages recorded in Honda Canyon indicate that plumes tend to float over the canyon rather than parallel the terrain contours. LINCOM/RIMPUFF's ability to handle this feature is rather limited, since a complete vertical momentum equation is not included. Other diagnostic and prognostic model simulations of Mt. Iron have also shown an inability to reproduce such local dosage minima. Resolutions higher than 500m may be helpful in refining such simulations.

7. ACKNOWLEDGEMENTS

This work was performed under contract #FY76169100412 with the Space Systems Division of USAF. We would like to thank our contract monitors, Capt. David Struck SSD/CLR and Bart Lundblad of the Aerospace Corporation for their comments and assistance. We would also like to thank Mr. Van Ramsdell of the Battelle Laboratory, Richland, WA for providing us with the Mt. Iron data set, our colleague, Mr. Charles Skupniewicz, the USAF SSD Toxic Release Assessment Group, and the Vandenberg meteorology and modeling community for providing both encouragement and an interested forum for this work.

8. APPENDICES

8.1 LINCOM Model Theory

8.1.1 Introduction

We simulated plume dispersion for each of the above ten flow types with a combined flow/puff model. LINCOM, the flow model, extends linear neutral potential flow theory (over a single hill) to a more general case involving mesoscale complex terrain. LINCOM is a diagnostic code which employs highly efficient solutions, which are spectrally based in the horizontal plane and analytic in the vertical. A "look-up table" of pre-computed results streamlines this procedure even further. Based on data from ten or more towers, LINCOM 1.0 can output a 100 x 140 gridded wind field for five vertical levels in the boundary layer at 500m horizontal resolution in less than one minute on a 386/33 PC.

The flow model is initialized with mean uniform velocity, pressure, and potential temperature fields, (U_0, V_0, W_0, and P_0), using data from each tower one at a time. Thus, at each tower the perturbation quantities u, v, w, and p induced by the terrain are all zero. LINCOM then solves the governing hydrodynamic equations solely in terms of the perturbation quantities; and adds the perturbation fields to the mean fields to obtain the final results: $U = U_0 + u$, $V = V_0 + v$, etc. So at any distance away from that tower the u, v, w, and p can assume non-zero values. We repeat this procedure for all n towers to obtain n separate initial perturbation wind fields. These fields are combined with a modified $1/r^2$ weighting scheme which warps each tower's circle of influence into ovals that are essentially congruent with the elevation contours for the surrounding terrain. This method ensures that the final field will exactly match the tower data, while tower influences extend strongly only along similar terrain elevations. In this way, even under differing stability conditions, a sufficient density of towers will tend to restore some of the non-neutral physics and force the final field to closely resemble the measured flow.

One problem with this procedure is that mass continuity can be compromised. Thus, in LINCOM 1.1 we instead find the set of mean fields which provides the best fit to the existing set of tower data when added to the resultant perturbation fields.

8.1.2 Governing equations

To discuss the modeling ideas in more detail, we begin with a truncation of the full atmospheric equation set which neglects density variations due to effects other than gravity. This

standard Boussinesq set forms the basis for almost all atmospheric modeling. Included are the three dimensional momentum equations (neglecting horizontal shear):

$$\frac{\partial u}{\partial t} + U\frac{\partial u}{\partial d} + V\frac{\partial u}{\partial y} + W\frac{\partial u}{\partial z} - fv = -\frac{1}{\rho}\frac{\partial \bar{p}}{\partial x} - \frac{1}{\rho}\frac{\partial}{\partial z}\tau_{xz} \quad , \qquad (8.1.1a)$$

$$\frac{\partial v}{\partial t} + U\frac{\partial v}{\partial x} + V\frac{\partial v}{\partial y} + W\frac{\partial v}{\partial z} + fu = -\frac{1}{\rho}\frac{\partial \bar{p}}{\partial y} - \frac{1}{\rho}\frac{\partial}{\partial z}\tau_{yz} \quad , \qquad (8.1.1b)$$

$$\frac{\partial w}{\partial t} + U\frac{\partial w}{\partial x} + V\frac{\partial w}{\partial y} + W\frac{\partial w}{\partial z} = -\frac{1}{\rho}\frac{\partial \bar{p}}{\partial z} - \frac{1}{\rho}\frac{\partial}{\partial z}\tau_{zz} - \frac{g\delta\theta}{\theta} \quad , \qquad (8.1.1c)$$

the thermodynamic energy (or potential temperature) equation,

$$\frac{\partial \theta}{\partial t} + U\frac{\partial \theta}{\partial x} + V\frac{\partial \theta}{\partial y} + W\frac{\partial \theta}{\partial z} + W\Gamma = -\frac{1}{\rho c_p}\frac{\partial \bar{\theta}}{\partial z} \quad ; \qquad (8.1.2)$$

the shallow convection form of the mass conservation or incompressible fluid continuity equation (applicable to boundary layer models), and the ideal gas equation of state,

$$\frac{\partial u}{\partial x} + \frac{\partial v}{\partial y} + \frac{\partial w}{\partial z} = 0 \quad ; \quad p = \rho RT \quad . \qquad (8.1.3)$$

Here, f, the Coriolis parameter is defined as $2\Omega\sin\theta$, where Ω is the earth's rate of rotation. Γ, the potential temperature lapse rate, is $\partial\theta/\partial z$. R and c_p are the gas and specific heat constants for air, and the τ_{ij} represent eddy stresses. We wish to simplify these equations because their complete solution at all relevant scales of motion in what is termed a direct simulation is beyond the forseeable capacity of computers. That is, the current direct simulation limit on CRAY class supercomputers is $\sim 10^7$ grid points for mesoscale flows. A 3-D direct simulation would require $\sim 10^{23}$ grid points to resolve the larger mesoscale (10^5m) circulations, the dissipation of turbulent kinetic energy which occurs down to 10^{-3}m, and the intervening scales of turbulent and forced motions. Since operational models use less than 10^5 grid points, sub-grid scale effects must be parameterized rather than modeled directly. Much of the energy is resolved on the grid itself; however, sub-grid motions cannot be neglected because the non-linear eddy stress dynamically links all scales of turbulence in an energy

cascade. Thus, without dissipation into internal energy, that is, heat, the modeled turbulence kinetic energy would simply grow without bound.

Other difficulties abound. For example, due to the continuum of turbulence scales, simple analytic forms for eddy stress do not exist. The better approximations are spatially dependent. They also involve higher order correlations between both supra and sub-grid velocity and pressure fluctuations whose magnitudes are still being debated. Non-linear advection also creates annoying cross terms which are usually simply ignored when the equations are written in non-orthogonal terrain following coordinates. Thus, even with supercomputers, the full or "primitive" equation mesoscale models are still too unwieldy for operational purposes.

Thus, to simplify in a way which hopefully blends suitability with convenience, we can make linearizing approximations of the sort,

$$U\partial U/\partial x = (U_0 + u)d(U_0 + u)/\partial x \tilde{} U_0\partial u/\partial x \quad . \qquad (8.1.4)$$

Fourier transforming the linearized equations to spectral space will then allow symbolic matrix inversion solutions for each wavenumber for the entire domain at once, rather than grid point by grid point as in finite differencing methods. However, we must remain aware that the linearization procedure neglects the higher order products of perturbed quantities, such as $u\partial u/\partial x$. This is only valid if $u\partial u/\partial x << U_0\partial u/\partial x$.

To suit this level of modeling we match the above approximation with a first order approximation of the eddy stress, i.e., $\tau_{uz} = -K \partial u/\partial z$, where K is the horizontally diffusivity coefficient.

Moreover, for stationary flows or at least if $\partial U/\partial t << U\partial U/\partial x$, we can also neglect time derivatives. This inequality implies that $1/T << u/L$, where T and L are characteristic time and length scales for flow changes. For a typical $T \tilde{} 6hr$ and $u \tilde{} 1m/s$, we need an $L << 20$ km. For $u \tilde{} 10m/s$, we need an $L << 200$ km. These are both reasonable for Vandenberg.

In LINCOM 1.0 and 1.1 we also neglect buoyancy forces caused by an uneven density/temperature field. So neutral LINCOM cannot diagnose thermally induced slope flows or seabreezes, except as indicated within the mean flow given by the towers or the later tower based objective analysis. this neglect allows a decomposition of the flow field into orthogonal components which are pre-calculable for a given domain and thus lead almost immediately to a final wind field. Also, thermal forcing at scales less than 10 km is often subordinate to the dynamic pressure forces which neutral LINCOM does account for.

At any rate, we are left with the following simplified, steady state, linearized equation set for the perturbed part of the flow:

$$U_0 \frac{\partial u}{\partial x} + V_0 \frac{\partial u}{\partial y} = - \frac{\partial p}{\partial x} + fv + K \frac{\partial^2 u}{\partial z^2} \quad , \qquad (8.1.5a)$$

$$U_0 \frac{\partial v}{\partial x} + V_0 \frac{\partial v}{\partial y} = - \frac{\partial p}{\partial y} - fu + K \frac{\partial^2 v}{\partial z^2} \quad , \qquad (8.1.5b)$$

$$U_0 \frac{\partial w}{\partial x} + V_0 \frac{\partial w}{\partial y} = - \frac{\partial p}{\partial z} + K \frac{\partial^2 w}{\partial z^2} \quad . \qquad (8.1.5c)$$

The continuity and ideal gas equations remain unchanged. The $1/\rho$ density factor has been absorbed into the perturbation pressure, p. As discussed, we have dropped the buoyancy term, $g\delta\Theta/\Theta$. We have also dropped the small vertical terms. The solution set is analytic for any choice of the perturbation quantities. (u, v, w, p, and K)

8.1.3 Solution method

To solve eqns. (8.1.2, 3, and 5) we drop the Coriolis term and begin with a simplified 2-D version of the model in order to sketch the main ideas. Later, we add more complex refinements included in the real 3-D model. First, we Fourier transform the x component of velocity into wave number (k) space in the fashion,

$$u(k,z) = \int_{-\infty}^{\infty} u(x,z) \exp(ikx) \, \partial x \quad , \qquad (8.1.6a)$$

$$u(x,z) = \frac{1}{2\pi} \int_{-\infty}^{\infty} u(k,z) \exp(-ikx) \, \partial k \quad , \qquad (8.1.6b)$$

where eqn. (8.1.6b) is the back transform of u(k,z). Note that the z direction does not participate in the transform and is written only to remind us of the height dependence of u. Then by differentiation of eqn. (8.1.6a),

$$\frac{\partial u}{\partial x} = ik\int_{-\infty}^{\infty} u(k,z)\exp(-ikx)\,\partial k = iku \quad . \qquad (8.1.7a)$$

Thus, the momentum equation for u may be written as,

$$U_0 ik\int_{-\infty}^{\infty} u(k,z)\exp(-ikx)\partial k + ik\int_{-\infty}^{\infty} p(k,z)\exp(-ikx)\partial k -$$

$$K\frac{\partial}{\partial z}\int_{-\infty}^{\infty} u(k,z)\exp(-ikx)\partial k = 0. \qquad (8.1.7b)$$

So the sum of the wave number components must total to zero. For each wave number, the 2-D version of the governing equations will then look like,

$$ikU_0u(k,z) + ikp(k,z) - K\,\partial^2u/\partial z^2 = 0 \quad , \qquad (8.1.8a)$$

$$ikU_0w(k,z) + \partial p(k,z)/\partial z - K\,\partial^2w/\partial z^2 = 0 \quad , \qquad (8.1.8b)$$

$$iku(k,z) + \partial w(k,z)/\partial z = 0 \quad . \qquad (8.1.8c)$$

By virtue of the Fourier transform, the sum of the perturbation quantities at each wave number, k, summed over all k, is equivalent to their determination for each grid point along x in real space. However, it remains to determine the dependence of these perturbation quantities along the z axis. Thus, eliminating w(k,z) and p(k,z) from this set leads to a fourth order ordinary differential equation (O.D.E.) with constant coefficients,

$$\frac{\partial^4u(k,z)}{\partial z^4} - (k^2 + ikU_0/K)\frac{\partial^2u(k,z)}{\partial z^2} + \frac{ikU_0k^2u(k,z)}{K} = 0. \qquad (8.1.9)$$

As is the usual fashion for ordinary differential equations, we can assume exponential solutions in z of the form, $\exp(-\alpha z)$, where α is a complex number. This leads to the fourth order polynomial equation,

$$\alpha^4 - (k^2 + ikU_0/K)\alpha^2 + ikU_0k^2/K = 0 \quad , \tag{8.1.10}$$

which is characteristic of the fourth order O.D.E. This equation has the four roots,

$$\alpha = \begin{cases} +/- \ |k| \quad , \quad \text{and} \\ +/- \ \sqrt{(ikU_0/K)} \quad . \end{cases} \tag{8.1.11}$$

However, the two positive roots lead to unlimited increases in u with z. Thus, only the two negative roots represent components of the real solution,

$$u(k,z) = U_1 \exp(\sqrt{(ikU_0/K)}\ z) + U_2 \exp(-|k|z) \quad , \tag{8.1.12a}$$

or

$$u(k,z) = U_1 \exp(-\alpha_1 z) + U_2 \exp(-\alpha_2 z) \quad . \tag{8.1.12b}$$

Note for each component solution that

$$\partial u(k,z)/\partial z = -\alpha_i U_i \exp(-\alpha_i z) \quad . \tag{8.1.13}$$

So in general α is equivalent to the differential operator,

$$\alpha = d/\partial z \quad . \tag{8.1.14}$$

We will use this below in determining U_1 and U_2. But before doing so, we focus on the exponential terms. First, we introduce the inner and outer length scales, ℓ, and L. In the simplest case, L is the horizontal dimension for a solitary hill. This will introduce only one wave number, k = 1/L, into the flow response. We define the inner scale, ℓ, by

$$\ell \ln (\ell/z_0) = k^2L = k \quad , \tag{8.1.15}$$

where z_0 is the roughness length (Jackson and Hunt, 1979). Physically, we are assuming that the hill interacts strongly with the region below ℓ through turbulent exchange. Thus, below ℓ is a region of large wind shear, whereas above ℓ turbulent exchange is small and resulting in nearly inviscid potential flow.

For neutral flow Monin-Obukhov similarity theory specifies for horizontally homogeneous surface layers that

$$U_0(z) = u_* \ln(z/z_0)/\kappa, \quad \text{and} \tag{8.1.16a}$$

$$K(z) = u_* z/\kappa \quad , \tag{8.1.16b}$$

where κ, the von Karman constant is $\simeq 0.4$. Thus, $U_0/K = \ln(z/z_0)/\kappa^2$. This leaves,

$$\alpha_1 = \sqrt{(ikU_0/K)} = (1+i)\sqrt{(\ln(z/z_0)/k)}/\sqrt{2} \quad , \tag{8.1.17}$$

where we have used $\sqrt{i} = (1+i)/\sqrt{2}$. Now at the height $z = \ell$, we have

$$\alpha_1 = (1+i)/\sqrt{(2\ell)} \quad , \tag{8.1.18}$$

while the second root is simply,

$$\alpha_2 = -|k| = -1/L \quad . \tag{8.1.19}$$

Thus, we have framed the advection velocity component at wavenumber, k, in terms of the two Jackson-Hunt length scales.

Returning to the U_1 and U_2 coefficients, for real flows with a non-slip bottom boundary, u(k,z) must become zero at z = 0. From eqn. (8.1.12b) this forces

$$U_1 = -U_2 \quad . \tag{8.1.20}$$

For the magnitude of U_1, we assume to first order that the vertical wind near the surface is given by the vertical component of the wind vector parallel to the surface, whose speed is taken to be equal to the horizontal wind speed. That is, $U \cdot \nabla h = w(0)$, where h is terrain height and U is the steady state wind. By the Fourier transformation, h(x) becomes -ikh(k) , where h(k) is defined by

$$h(x) = \frac{1}{2\pi} \int_{-\infty}^{\infty} hk \exp(-ikx)\partial k \quad . \tag{8.1.21}$$

This leads to the condition,

$$-ikh(k) = \frac{W_1}{U_{01}} + \frac{W_2}{U_{02}} \quad . \tag{8.1.22}$$

Here we have approximated the mean wind U_0 from eqn. (8.1.16a) in terms of two components, U_{01} and U_{02}, as functions of α_1 and α_2 and, hence, ℓ and L. Namely, U_{01} and U_{02} are the mean wind velocities at $z = \ell$ and $z = L$. We approximate K, the turbulent diffusivity, similarly in terms of ℓ and L. This implies that a perturbation penetrating to larger heights will be subject to larger mean velocities and diffusivities than less penetrative perturbations.

At any rate, from eqns. (8.1.8) and (8.1.14), we have

$$w(k,z) = ik\, u(k,z)/\alpha \quad . \tag{8.1.23}$$

Combining eqn. (8.1.20) with (8.1.22) and (8.1.23) gives

$$\frac{ik}{\alpha_1 U_{01}} + \frac{ik}{\alpha_2 U_{02}} U_1 = -ikh(k) \quad . \tag{8.1.24}$$

With $LU_{02} >> \ell U_{01}$ we can neglect the first term and with eqn. (8.1.19),

$$U_1 \approx -|k| U_{02}\, h(k) \quad . \tag{8.1.25}$$

Substituting this into eqn. (8.1.12), we finally obtain for the simple 2-D case the velocity perturbation for a single wave number, k, at height z above the terrain,

$$u(k,z) = \frac{h(k)}{L} U_0(L) \left[e^{-z/L} - e^{(1+i)z/\sqrt{2}\ell} \right] \quad . \tag{8.1.26}$$

We then back Fourier transform to real space and add the perturbation to the mean velocity to produce the total U field. A plot of the vertical profile shows that the maximum perturbation in 2-D occurs at $(3/2\sqrt{2})\ell \sim 3.3\ell$. That is, hills induce pressure gradients which interact with the shear stress to force advection to produce a low-level jet, as in Jackson-Hunt theory.

Generalizing to 3-D flow requires that we re-introduce the Coriolis term and add an equation and terms for the y component. In the 2-D case we solved the O.D.E. system by eliminating variables and consolidating equations until only one fourth order O.D.E. remained. However, for 3-D cases this procedure is too cumbersome. So we re-organize the mathematics by writing the governing equations in matrix form and solve them systematically through elementary row operations on the matrix, rather than by elimination.

For the 3-D case the form of the Fourier transform and back transform now become,

$$u(k,m,z) = \int_{-\infty}^{\infty} \int_{-\infty}^{\infty} u(x,y,z)\exp(ikx + imy)\,\partial x\,\partial y \quad , \qquad (8.1.27a)$$

$$u(x,y,z) = \frac{1}{2\pi} \int_{-\infty}^{\infty} \int_{-\infty}^{\infty} u(k,m,z)\exp(-ikx-imy)\,\partial k\,\partial m \quad , \qquad (8.1.27b)$$

or more precisely, using the discrete (fast) Fourier transform pair,

$$u(k,m,z) = \sum_{k=0}^{n-1} \sum_{m=0}^{n-1} u(x,y,z) W_{nkx}\, W_{nmy} \quad , \qquad (8.1.28a)$$

$$u(x,y,z) = \frac{1}{n^2} \sum_{x=0}^{n-1} \sum_{y=0}^{n-1} u(k,m,z) W_{n-kx}\, W_{n-my} \quad , \qquad (8.1.28b)$$

where $W = \exp(i2\pi/n)$, and similarly for v, w, p, and h. Then the momentum and continuity equations for the Fourier transformed components at each wave number pair, (k,m), may be written in the form of the matrix equation,

$$\begin{bmatrix} C & -f & 0 & ik \\ f & C & 0 & im \\ 0 & 0 & C & -\alpha \\ ik & im & -\alpha & 0 \end{bmatrix} \begin{bmatrix} u(k,m) \\ v(k,m) \\ w(k,m) \\ p(k,m) \end{bmatrix} = \begin{bmatrix} 0 \\ 0 \\ 0 \\ 0 \end{bmatrix} , \qquad (8.1.29)$$

where, using eqn. (8.1.14),

$$C \equiv i(kU_0 + mV_0) - K\alpha^2 \quad . \qquad (8.1.30)$$

Rather than by elimination, we can solve this set systematically through elementary row operations (cf. any text on O.D.E. systems). In place of eqn. (8.1.10) the characteristic equation becomes,

$$C(k^2 + \alpha^2) = 0 \quad . \qquad (8.1.31)$$

We replace eqn. (8.1.15) for ℓ by

$$\ell \ln (l/z_0) = \kappa^2 L/\cos \beta \quad , \qquad (8.1.32)$$

where the mean wind vector, $\mathbf{V} \equiv (U_0,V_0)$, $L = 1/k$, and β is the slope angle, such that

$$|\mathbf{V}||(k,m)|\cos \beta = \mathbf{V} \cdot (k,m) \quad . \qquad (8.1.33)$$

The surface boundary condition for w changes from eqn. (8.1.22) to

$$-ikh_{k,m} = \frac{W_1}{(k,m) \cdot \mathbf{V}_{01}} + \frac{W_2}{(k,m) \cdot \mathbf{V}_{02}} \quad . \qquad (8.1.34)$$

For winds not perpendicular to a 2-D hill, Troen (1986) showed that eqn. (8.1.26) still gives the perturbation of the component normal to the hill. That is, the first, outer scale, term in L is not affected by wind direction, but ℓ, given by eqn. (8.1.32), is now larger for off-normal winds; below ℓ, the wind speed perturbation

is no longer given by a simple cosine response.

An idealized neutrally stable boundary layer should have no abrupt top. In reality the top, H, is usually specified by other conditions, such as a subsidence inversion (chronic for Vandenberg) or the advected "fossil" remains of a capping inversion formed when the upstream boundary layer was last convectively unstable. So we must account for H. We also expect that LINCOM will be used in cases where the atmosphere is not truly neutral. That is, the inverse Obukhov length, $1/L_{mo}$ will not be zero. In that case, L_{mo} can be measured from surface data and used in similarity functions in order to obtain the vertical profiles of mean wind speed and diffusivity. E.g., the mean wind and diffusivity profiles may be obtained from the following extended boundary layer similarity profiles of Sorbjan (1989). He suggested that

$$V_0 = 2.5u_*(\ln(z/z_0) + 5\ z/L - z/H - 2.5\ z^2/HL_{mo})) \quad , \quad (8.1.35a)$$

$$K = 0.4\ u_*z(1 - z/H)/(1 + 5\ z/L_{mo}) \quad , \quad (8.1.35b)$$

for stable cases and

$$V_0 = 2.5u_*(\ln(z/z_0) + \phi_m \quad , \quad (8.1.36a)$$

$$K = 0.4\ u_*z(1 - 28\ z/L_{mo})^{1/4} \quad , \quad (8.1.36b)$$

for unstable cases. Here we supply a new, more efficient algorithm for ϕ_m,

$$\phi_m = (1.19 + 0.23*\ln(-z/L_{mo})\ )^2 \quad . \quad (8.1.37)$$

8.1.4 Obukhov length

Unless sensors are frequently calibrated, potential temperature differences between vertical levels cannot be measured accurately enough on a routine operational basis to maintain confidence in atmospheric surface layer stability estimates. Thus, LINCOM 1.1 does not determine Obukhov length from the potential temperature and wind speeds differences between vertical levels. Instead, it relies on measured solar and thermal radiation values or estimates thereof. This type of method is useful for Vandenberg because the

near coastal areas are chronically shrouded with stratus cover, while the sky is often quite clear several kilometers inland. Thus, for diagnostic models such as LINCOM, Obukhov lengths need be computed for only a few areas between sun and shade, based on moderate differences in roughness length and local wind speeds.

We also included a routine to estimate downwelling solar and thermal radiation, if measured data is not available. This routine requires a fractional cloud coverage estimate as well as other commonly available input data, such as inversion height, screen level wind speed, temperature, and relative humidity.

All solar radiation models require current date and time to compute sun angle, ψ. This is done in LINCOM using standard algorithms. We modified a simple ASHRAE model for downwelling solar direct and diffuse radiation (Iqbal, 1983) by computing sine curve fits to the seasonal adjustments for apparent extra-terrestrial radiation, atmospheric optical air mass, and column length of precipitable water, W.

If cloud base height, z_c, and boundary layer height, H, are not available, the solar transmissivity through clouds, τ_c, is estimated using the simple algorithm,

$$\tau_c = (1 - 0.6FCC) \quad , \tag{8.1.38}$$

where FCC is fractional cloud coverage of the sky. FCC can be obtained from ground based observation and/or on-line GOES satellite data, using the algorithm described in Skupniewicz et al, (1991). If z_c and H are available (from rawinsonde data or aircraft landing reports), the solar transmissivity for a non-reflective ground surface can be estimated more accurately from the method of Liou and Wittman (1979). This method uses sun angle and column height of precipitable water within the cloud in a bivariate polynomial regression based on results from an accurate multi-stream discrete ordinates model. Currently, we assume that the cloud coverage is stratiform and confined to the boundary layer, with a liquid water content of 0.78 grams/meter of cloud depth. Hence, the only inputs required are date, time, cloud base height, and boundary layer depth. The algorithm can be extended easily to include other cloud types and water content. The regression form is

$$\tau_c(\mu_0, W) = \sum_{i=0}^{3} \sum_{j=0}^{3} b_{ij} \, \mu_0^i \, W^j \quad , \tag{8.1.39}$$

where μ_o is solar zenith angle, W is precipitable water, and the b_{ij} are the coefficients obtained from the regression. For actual non-

zero surface albedoes, A_s (default value, 0.15), we modify the cloud solar transmissivity, using the algorithm of Kamada (1984),

$$\tau_{cm} = \left[\frac{1 - A_s A_c}{(1 - 0.12A_c)(1 - 0.1A_s)} (1 - d\phi)\tau_c + d\phi \right]^{FCC} , \qquad (8.1.40)$$

where A_c is cloud top albedo (default value for stratiform clouds is 0.55), d = 0.001068, and ϕ is in degrees latitude. The total downwelling solar radiation is then

$$SOL\downarrow = (I_0 \sin(\psi) + I_{diff})\tau_{cm} , \qquad (8.1.41)$$

where I_{diff} is the downward diffuse solar radiation at the surface.

The downwelling thermal radiation computation is initiated, using the algorithm of Martin and Berdahl (1983), which employs surface dewpoint temperature, T_{dp}, hour of the day, Hr, and pressure, p, to estimate the effective clear sky emissivity,

$$\epsilon_{cs} = 0.711 + 0.0056\,T_{dp} + 0.00073\,T_{dp}^2 + 0.013\cos(0.262Hr) + 0.00012(p - 1000) . \qquad (8.1.42)$$

T_{dp} is readily obtained from the relative humidity and temperature, using standard formulas. The emissivity is then modified for clouds according to cloud base height, z_c, and fractional cloud coverage, FCC. Thus, we have

$$\epsilon_c = \epsilon_{cs} + 0.85\,FCC(1 - \epsilon_{cs})\exp(1.22\times10^{-4}\,Z_c) . \qquad (8.1.43)$$

Again, boundary layer stratus clouds are assumed here but other cloud types are readily included. Downwelling thermal radiation is computed by assuming the cloudy or clear sky to be a grey body thermal emitter, such that

$$IR\downarrow = \epsilon_c \sigma \Theta^4 , \qquad (8.1.44)$$

where $\sigma = 5.67 \times 10^{-8}$ is the Planck black body constant. Total downwelling radiation at the earth's surface is obtained by combining solar and thermal contributions via,

$$RAD\downarrow = (1 - A_s)SOL\downarrow + IR\downarrow \quad . \tag{8.1.45}$$

With the radiation component of the surface energy budget computed, we can obtain the atmospheric stability and temperature flux from the ground surface to the air. As a measure of atmospheric stability, the Obukhov length is defined as,

$$L = u_*^2 \theta / g\kappa\theta_* \quad , \tag{8.1.46}$$

where u_* is the surface layer friction velocity, $\theta = T(1000/p)^{0.285}$ is the near surface potential temperature, g is gravitational acceleration, κ is 0.4, the von Karman constant, and θ_* is the Obukhov temperature scale. The temperature flux can be defined as the statistical correlation between vertical velocity and potential temperature perturbations, and is also given by

$$\overline{w'\theta'}_0 = -u_* \theta_* \quad . \tag{8.1.47}$$

Thus, given the downwelling radiation, we can iterate between estimates of L and estimates of surface temperature flux until both quantities converge. This requires that we compute both u_* and θ_*. u_* comes from

$$u_* = U(z) \sqrt{\frac{k}{Ln(z/z_0) - \Psi m}} \quad , \tag{8.1.48}$$

where U(z) is the mean windspeed at height z, and z_0 is the surface vegetative canopy roughness length (typically $\simeq$ 1/7 the mean vegetation height). ϕ_m is given by eqn. (8.1.37). Analogous to u_*, θ_* is given by

$$\theta_* = \overline{\delta\theta}(z) \sqrt{\frac{k}{Ln(z/z_0) - \Psi_h}} \quad , \tag{8.1.49}$$

From Dyer and Bradley (1982), we have

$$\Psi_h = 2\ \mathrm{Ln}\left(\tfrac{1}{2}\ (1 - \sqrt{1 - 14z/L}\ )\right) \quad . \qquad (8.1.50)$$

To obtain the ground surface "skin" temperature, θ_{00}, we assume that the potential temperature difference between the roughness height, z_0, and height, z, is given by $\delta\theta$, and that the temperature difference across the laminar layer between z_0 and the surface is given by θ_*. Thus,

$$\theta_{00} = \theta - (\theta_*/\kappa)(\mathrm{Ln}(z/z_0) - \Psi_h) - \theta_* \quad . \qquad (8.1.51)$$

Since $\delta\theta$ is not known, θ_* is initially set to zero and the skin temperature is set equal to the screen level potential temperature. The temperatures then diverge toward equilibrium values by iteration. The net radiative budget at the surface is given by

$$\mathrm{NETRAD} = \mathrm{RAD}\downarrow - \epsilon_g \sigma \theta_{00}^4 \quad , \qquad (8.1.52)$$

where the ground surface emissivity, ϵ_g, has a default value of 0.95. Following the Penman-Monteith model (1948, 1965), temperature flux into the ground is estimated as, $Q_g = 0.15$ NETRAD with the stipulation that for stable conditions (if $L > 0$), Q_g is 3.3 times larger. The Penman-Monteith equation is used to estimate the temperature flux,

$$\overline{w'\theta'}_0 = \frac{-(\gamma\ (-\mathrm{NETRAD} + Q_g) - \overline{w'q'}_0)}{(\ \varrho\ c_p\ (X_g\ s_{cc} + \gamma)\ )} - 0.84\ \overline{w'q'}_0, \qquad (8.1.53)$$

where $\overline{w'q'}_0$ is the humidity flux, ρ is air density, $c_p = 1005\ \mathrm{J\ kg^{-1}\ K^{-1}}$ is the heat capacity of air, X_g is soil relative humidity, s_{cc} is the change rate of specific humidity with temperature for saturated air, and $\gamma = c_p/L_v \simeq 0.0004\ ^\circ\mathrm{K}^{-1}$ is the psychrometric constant. In turn these latter variables are obtained from standard algorithms. The Obukhov temperature scale is obtained from,

$$\theta_* = -w'\theta'_0/u_* \quad . \qquad (8.1.54)$$

In this scheme, note that under neutral conditions when the temperature flux falls to zero, θ_* will vanish and L becomes infinite. Thus, to avoid infinities during iterative numerical evaluation, it is better to compute the inverse Obukhov length, 1/L.

From a rough bivariate analysis of our results, we found that a useful first guess is

$$1/L = 0.000674(300 - RAD\downarrow)\ Ln(10\,z/z_0)/U^2(z)\ . \qquad (8.1.55)$$

In order to cover a wide range of radiation values, wind speeds, temperatures, and roughness lengths, the iteration procedure must be quite robust, otherwise convergence is not obtained, especially at low wind speeds. Even with a good first guess like eqn. (8.1.54), we found that simple iteration was unreliable, that the Newton-secant root finding procedure was needed for standard cases, and that second order Aitken acceleration was required for low wind speeds and small roughness lengths.

The Newton-secant root finding algorithm utilizes the form,

$$x_{i+1} - x_i = \delta_{i+1} = \frac{-\delta_i\, f(x_i)}{f(x_i) - f(x_{i-1})}\ , \qquad (8.1.56)$$

where i is iteration number. Here x is 1/L, and f(x) is the difference between old and new values of 1/L. The object of the iteration process is to adjust f(x) toward zero. Unlike the standard Newton-Raphson technique, the secant method does not require an analytic expression for the first derivative of f(x), which in our case is not obtainable. The Aitken technique is a second order acceleration method,

$$x_{i+3} - x_i = \delta_{i+3} = \frac{x_i x_{i+2} - x^2_{i+1}}{x_{i+2} - 2x_{i+1} + x_i}\ , \qquad (8.1.57)$$

which relies on the Newton-secant method for the first two iterations, then computes the rate of change of the convergence from the first two iterations and uses it to obtain a refined estimate for the third and subsequent iterations.

8.1.5 Objective Analysis

To produce each of the n flow fields for the n towers, the mean wind vector from each tower is added to the terrain induced perturbation field from LINCOM. Then at each grid point, the U_i from the n flow fields are combined according to the algorithm,

$$U(x,y) = \frac{\sum_{i=1}^{n} U_i/r_i^2}{\sum_{i=1}^{n} 1/r_i^2} \quad , \qquad (8.1.58)$$

where r_i is the terrain modified distance from the grid point to tower i. In general we define r as,

$$r = (a + (b - a)|\sin \phi|)R \quad , \qquad (8.1.59)$$

Here ϕ is the tower-to-grid-point angle measured from north (as in meteorological wind angle). R is the actual tower-to-grid-point distance,

$$a = \sqrt{(A/B)} \quad , \text{ and } \quad b = 1/a \quad .$$

where the dominant aspect ratio of the surrounding terrain height contours is given by A/B. Thus, rather than a $1/R^2$ diminished circle of influence, each tower has a $1/r^2$ diminished oval of influence which corresponds to the dominant shape and orientation of the elevation contours surrounding the tower. Of course for every grid point the r_i in a given domain need be computed only once, then stored for future use.

This method of combining flow fields from each tower ensures that the final field will exactly match the tower data, while winds at locations between towers are prescribed by a combination of terrain modified objective analysis and neutral boundary layer dynamics.

In LINCOM 1.1 we noted from eqns. (8.1.16 - 19) that α_1 and α_2, the vertical decay coefficients for the terrain induced wind perturbation fields, are independent of mean wind speed. For neutral flow this means that the fundamental characteristics of the perturbation field are determined by the terrain and are thus domain specific. So the perturbation field may be expressed as a linear combination of the mean wind vector and the two orthogonal

component solutions for the perturbations along the x and y axes. Since the component solutions for any given domain may be pre-stored, this allows an extremely fast "look-up table" mode of running LINCOM.

Actually, several sets of orthogonal solutions may be stored to account for different inversion heights. Interpolation and a fitting algorithm are then used to determine the mean wind vector, which when combined with the perturbation fields, will best fit the available tower data. The best fit is determined by minimizing the differences between the tower and LINCOM winds. Unlike LINCOM 1.0 this new procedure in LINCOM 1.1 relaxes absolute tower anchoring in order to ensure mass conservation of the flow field. A reasonably close fit to the tower data is retained, but with little potential for aliasing as described in sections 3.1 and 5.2. This procedure also results in a significant gain in computational speed when many towers are involved.

8.2 RIMPUFF Model Theory

8.2.1 Introduction

Since distinctions between turbulence and mean wind are not well resolved in complex terrain, some arbitrary scale such as the model's grid resolution becomes a convenient divider. That is, we can determine the mean flow down to the grid scale as a direct deterministic response to the physical forces. However, the grid resolution cannot be arbitrarily fine because we lack fine scale information about bottom boundary conditions, especially in complex terrain, and also because computer power is finite. Moreover, sub-grid scale effects must be parameterized rather than simply neglected because the non-linear eddy stress dynamically links all scales of turbulence in an energy cascade. Thus, without modeling the dissipation to heat, the turbulence kinetic energy would simply grow without bound. Luckily for our investigation, the sub-grid fluid motions can be treated statistically, since smaller scales tend to behave more randomly, even in complex terrain.

Hence, RIMPUFF lets LINCOM handle the bulk transport, while it treats the instantaneous diffusion in a relative frame which follows the mean flow. Continuous releases, i.e., plumes, are modeled by a series of puffs released into the meandering flow field. RIMPUFF computes species concentrations by summing contributions from all puffs for each grid point and time step. Depending on computer capacity, the model can handle several hundred puffs released from multiple point sources anywhere within the domain. Such sources can have individual release rates, times and heat production rates. Plume heights depend on standard formulas using downwind distance, stability, and stability dependent, vertical profiles of windspeed. The inversion is assumed to parallel the terrain and is treated as a material surface. Both the inversion and source heights are user specified.

Total surface reflection of puffs is normally assumed for inert gases, but the reflection coefficient is adjustable from zero to unity for materials with real deposition rates. Dry deposition is calculated from source depletion. Dispersion parameters for each puff depend on items such as pollutant type, atmospheric stability, and wind speed. Wet deposition depends on species and the space/time distribution of the rain field.

8.2.2 Governing equations

The horizontal sub-grid diffusion is treated by linking puff growth to the time averaged, local component spectra of the lateral velocities (see below). A kinematic-statistical approach is employed which assumes that the relative displacement of fluid elements proceeds in a gaussian manner.

That is, with Q referring to total puff mass and C(x,t) to the observed concentration field in space and time, we begin by posing the mass conservation and center of mass location as

$$Q = \int C(x,t)\,\partial x \quad , \quad \text{and} \tag{8.2.1}$$

$$c(t) = 1/Q \int x\, C(x,t)\,\partial x \quad . \tag{8.2.2}$$

The center of mass is subject to transport by the mean flow determined by LINCOM and also by grid scale and sub-grid scale turbulence not included in LINCOM. This turbulence "meander" is estimated by a stochastic puff advection scheme described later. At any rate the center of mass velocity in a fixed frame can be described as a summation of the product of the puff mass at each location with its respective velocity,

$$V_{cm}(t) = 1/Q \int u(x,t)\, C(x,t)\, \partial x \quad , \tag{8.2.3}$$

where u(x,t) represents the fluid velocity field. We then denote both the average of all particles within a puff and the ensemble average by "< >" and fluctuations by " ' ". Thus, if $C(x,t) = \langle C(x,t) \rangle + C'(x,t)$, then $1/Q \langle C(x,t) \rangle \partial x$ denotes the probability of finding a marked particle at the point (x,t) and

$$\langle x^2 \rangle = 1/Q \int x^2 \langle C(x,t) \rangle \partial x \tag{8.2.4}$$

denotes the ensemble averaged, fixed frame, absolute diffusion. The latter may be expressed as the sum of meander and relative diffusion, or

$$\langle x^2(t) \rangle = \langle y^2(t) \rangle + \langle c^2(t) \rangle \quad , \tag{8.2.5}$$

where y = x - c defines a coordinate frame moving with the center of mass velocity.

Now, using τ to time integrate along a particle's path with respect to the center of mass, the puff growth rate becomes,

$$\partial\sigma^2/\partial t = 2 \int_0^t \langle v(t)\, v(t-\tau) \rangle\, d\tau$$

$$= \langle v^2(t) \rangle \int_0^t r(t,\tau)d\tau = \langle v^2(t) \rangle t_r(t) \quad . \tag{8.2.6}$$

Here, σ is puff size (standard deviation of particle displacement relative to center of mass) and $\langle v^2(t) \rangle$ is the corresponding relative velocity variance. The relative correlation function, $r(t,\tau)$, depends on both t and τ. This indicates a non-stationary process, unlike Taylor's single particle diffusion. Letting $v = u - V_{cm}$ be the moving frame particle velocity, we can show that

$$\partial\sigma^2/\partial t = 2 \int_0^t [R_{abs}(\tau) - R_{cm}(t,\tau)] \, \partial\tau \quad . \tag{8.2.7}$$

Here,

$$R_{abs}(\tau) = \langle u(t)u(t-\tau) \rangle \quad , \quad \text{and} \tag{8.2.8a}$$

$$R_{cm}(t,\tau) = \langle V_{cm}(t)V_{cm}(t-\tau)) \rangle \tag{8.2.8b}$$

are the appropriate auto-covariance functions for absolute single particle diffusion, and from the center-of-mass-velocity viewpoint, respectively. Since R_{abs} is known, we can focus on obtaining a model for R_{cm}.

Using (8.2.3), $R_{cm}(t,\tau)$ can be rewritten as

$$\iint \langle u(x',t)u(x'',t-\tau) \; C(x',t)C(x'',t-\tau) \rangle \partial x' \partial x'' \quad . \tag{8.2.9}$$

From this point the puff can be modeled as a set of passive marked particles with instantaneous concentration, C(x,t), moving within a large but numerable set of unmarked fluid elements, with Eulerian velocity field u(x,t). Any relative displacements, y(t), can also be assumed to obey the same un-correlated gaussian statistics (see fig. 8.2.1). That is, any two particles viewed in the moving frame will appear to disperse in an uncorrelated fashion, such that

$$\langle \Delta y_i \; \Delta y_j \rangle = \begin{cases} \sigma^2(t) - \sigma^2(t-\tau) & \text{for } i = j \\ 0 & \text{for } i \neq j \end{cases} \tag{8.2.10}$$

Physically, this means that the characteristic scale of motion in the moving frame must be much shorter than the puff size. However, these scales may overlap in the atmosphere, implying that only the ensemble average of individual puff releases will be approximately gaussian.

Hence, a gaussian puff of initial size, $\sigma(0)$, will remain a gaussian puff of size, $\sigma(t_i)$, at a later time, (t_i), so that

$$G_{\sigma(t)}(y,t) = \int G_s(y-y_0,t)\ G_{\sigma(t-\tau)}(y_0,t-\tau)\,\partial y_0 \quad . \qquad (8.2.11)$$

We also see that the spread, $< \Delta y^2{}_i(t,\tau) >$, for the transition probability, G_s, given in eqn. (8.2.10) satisfies eqn. (8.2.11).

Substituting the instantaneous concentrations from eqn. (8.2.9) with the corresponding gaussians now leads to

$$R_{cm}(t,\tau) = \int\int < u(y',t)u(y'',t-\tau) > G_{\sigma(t)}(y',t)\,G_{\sigma(t-\tau)}(y'',t-\tau)\,\partial y'\partial y'', \qquad (8.2.12)$$

where the moving frame fluid velocity, u, relates to the fixed frame velocity by $u(y,t) = u(y+c,t)$.

We must also obtain the two-point, two-time (fixed frame) velocity covariance, $< u(y',t)u(y'',t-\tau) >$. For two particles, i and j, in a homogeneously turbulent field, the velocity covariance function, in a fixed frame, $R_{abs}(\xi_{ij},\tau)$, will depend only upon the temporal and spatial separations, τ and ξ_{ij}, between the particles. That is,

$$R_{abs}(\xi_{ij},\tau) = < u(x_i(t))\ u(x_i(t-\tau) - \xi_{ij}) > \quad . \qquad (8.2.13)$$

Thus, the moving frame velocity covariance in eqn. (8.2.12) is written in terms of the absolute velocity covariance function and the transition probability from eqn. (8.2.11) as

$$< u(y',t)u(y'',t-\tau) > = \int G_s(y'-y''-\xi,t)\,R_{abs}(\xi,\tau)\,d\xi \quad . \qquad (8.2.14)$$

Returning this to eqn. (8.2.12) and integrating over y' and y" will reformulate the center-of-mass covariance as

$$R_{cm}(t,\tau) = R_{abs}(\xi,\tau)/[2\sigma(t)\sqrt{\pi}\ e^{-\xi^2/4\sigma^2(t)}]\partial\xi \quad . \tag{8.2.15}$$

Thus, in terms of the fixed frame covariances, the horizontal rate equation for puff growth becomes,

$$\partial\sigma^2/\partial t = 2\int_0^t (R_{abs}(0,\tau) - R_{abs}(\xi,\tau)/[\ 2\sqrt{\pi}\ \sigma(t)\ e^{-\xi^2/4\sigma^2(t)}]\ d\xi\partial\tau \quad . \tag{8.2.16}$$

For ease of use, we employ the Fourier transform,

$$R_{abs}(\xi,\tau) = S(\kappa,\omega)\ e^{i(\kappa\xi+\omega\tau)}\partial\xi\partial\omega \quad , \tag{8.2.17}$$

to render eqn.(8.2.16) as,

$$\partial\sigma^2/\partial t = 2t\int\int S(\kappa,\omega)\ \sin(\omega t)/\omega t\ (1 - e^{-\kappa^2\sigma^2(t)})\ \partial\omega\partial\kappa \quad . \tag{8.2.18}$$

In this case the spatial filter, $1 - e^{-\kappa^2\sigma^2(t)}$, has been inserted to remove wave numbers smaller than $1/\sigma$, while the low pass temporal frequency filter, $\sin(\omega t)/\omega t$, does likewise beyond $\omega = 1/t$. The shaded area in Fig. 8.2.2 shows the part of $S(k,\omega)$ that effectively contributes to the growth rate.

For puffs much larger than the turbulence length scale, eqn. (8.2.18) reduces to Taylor's formula for single particle diffusion. Hence, behavioral differences between a puff and a single particle are closely related to the spatial correlation of the turbulence. That is, for classically homogeneous turbulence with a Kolmogorov inertial subrange, the spectral index, $p = -5/3$. Puff growth will then follow a standard $t^{3/2}$ prediction. However, in a stably stratified atmosphere, p may be $\simeq -3$, implying exponential growth. In either case, we assume that the sub-grid diffusion is locally homogeneous. If so, we can scale the puff's instantaneous growth rate over intermediate ranges (< 500m) with the local lateral turbulence intensity, σ_i, such that $\partial\sigma/\partial t \approx 0.3\sigma_i u$. We obtained turbulence intensities for Vandenberg by modeling Eulerian wave lengths with the similarity formula,

$$\sigma_i = \sigma_{i0}(1 + B/ut)^{-1/3} \quad , \qquad (8.2.19)$$

where σ_{i0} refers to limiting values at large times (Skupniewicz, et al, 1989). That is, even within complex terrain, the turbulent energy characterized by Vandenberg's tower wind spectra tends to plateau at larger scales. Equation (8.2.19) tends to apply over a wider range of scales than simple power law estimates. Power law fits to Vandenberg data are also found to be rather windspeed dependent. Note that the constant, B, depends upon measurement height and stability and is proportional to the dominant eddy size at a given height. Thus, values for σ_{i0} and B were determined by multi-variate regression for each tower for each of three periods: pre-dawn, noon, and dusk, indicative of stable, unstable, and neutral conditions. Values were also classed by wind direction. The longitudinal and lateral values determined for σ_{i0} ranged typically from 700 - 2,000m and 200 - 1,000m, respectively. As in flat terrain, the longitudinal component clearly dominates. However, our values were consistently larger, suggesting that flow distortions due to complex terrain feed energy directly into larger horizontal scales of motion.

8.2.3 Puff splitting

Real diffusion in complex terrain also often displays plume bifurcation and/or vertical shear due to channeling, slope flows, or inversions. To simulate such decoupling we allow each puff to split as often as necessary. The daughter puffs are arranged such that the original center concentration, radially integrated second moments of the concentration distribution, and mass are all conserved.

These constraints may be summarized as,

$$\text{i} \quad \sum_{5}^{2} = \sigma^2_{p1} \quad , \qquad (8.2.20a)$$

$$\text{ii} \quad C_5(0,0) = C_1(0,0) \quad , \qquad (8.2.20b)$$

$$\text{iii} \quad \sigma_{p5} = (1/2)\sigma_{p1} \quad , \text{ and} \qquad (8.2.20c)$$

iv mass conservation.

For the Vandenberg simulations the initial puff diameter was set to 100m (one standard deviation in concentration). When the puff attains a diameter equal to the 500m grid spacing, it splits (pentafurcates) horizontally into five new gaussian puffs. The daughter puff diameters are initially set to 250m. The conservation relations then require that the four satellite puffs be centered at 0.89 σ_v from the origin and that the satellite and center puffs each carry 23.53 and 5.88% of the total matter, respectively (fig.5).

In the case of layers decoupled vertically by shear, the original puff is allowed to trifurcate into three daughter puffs which are centered along the original puff's vertical axis. To simulate a gaussian radial concentration profile, the conservation rules require that the two satellite puffs be centered at $+/-1.19\sigma_v$, with each new puff carrying 26.58 % of the initial pollutant mass. The new center puff retains the remaining 48.84 %. Again, the new puffs are born with half the diameter of the original puff.

The purpose of this splitting scheme is to allow each new puff its own individual growth rate and direction, as set by the mean flow and turbulence intensities local to it. We assume in this procedure that the sub-grid scale shearing is locally homogeneous so that filtered turbulence estimates can be used in the parameterization. The puff-splitting scheme can be repeated to a practical limit of several hundred puff progeny. In this way the plume bifurcation caused by terrain features can be modeled in detail. Such bifurcation was seen extensively during LVDE (see LVDE Data Report, 1990)

8.2.4 Stochastic puff-advection

The mean flow field provided by LINCOM should be updated every 5 to 10 minutes to include temporal variability and allow for puff meander in RIMPUFF due to non-stationary winds. But if measured winds are available only as one hour means, only horizontal shear in the static wind field is left to induce any meander in the puff center-of-mass advection velocity, V_{cm}. Such was the case for the eight Mt. Iron diffusion experiments. To re-introduce temporal variability in the wind field, we have added an auto-regressive (Langevin equation based) advection component to the two horizontal (u, v) wind components of the mean flow model. This is akin to standard Langevin random forcing in Monte Carlo dispersion but applied to puffs rather than particles.

We estimated supra-grid scale (> 500 m) wind variance, $\langle V_{cm}V_{cm}\rangle$, by low-pass filtering the horizontal wind energy spectrum below wave number $k = 2\sigma/500$ m. Since we already use the sub-grid scale (< 500 m) variance for puff growth, we now account for turbulence at all scales. $T_{L,\,puff} = L_E/u$ also provides a Lagrangian time scale for

horizontal puff motion, where L_E, an Eulerian length scale, is derived from velocity spectra measurements (see Handbook).

With these we can estimate stochastic contributions to V_{cm} from

$$V_{cm(t+\Delta t)} = \rho V_{cm(t)} + \eta \quad , \qquad (8.2.21)$$

where the Lagrangian correlation coefficient for the center-of-mass velocity is given by

$$\rho = \exp(-\Delta t/T_L) \quad , \qquad (8.2.22)$$

and η is white gaussian noise having a variance, $(1 - \rho^2)\langle V_{cm}V_{cm}\rangle$.

By comparing cases with and without, we found that the stochastic component is clearly visible during individual simulations. However, its contribution to the overall plume widths is small.

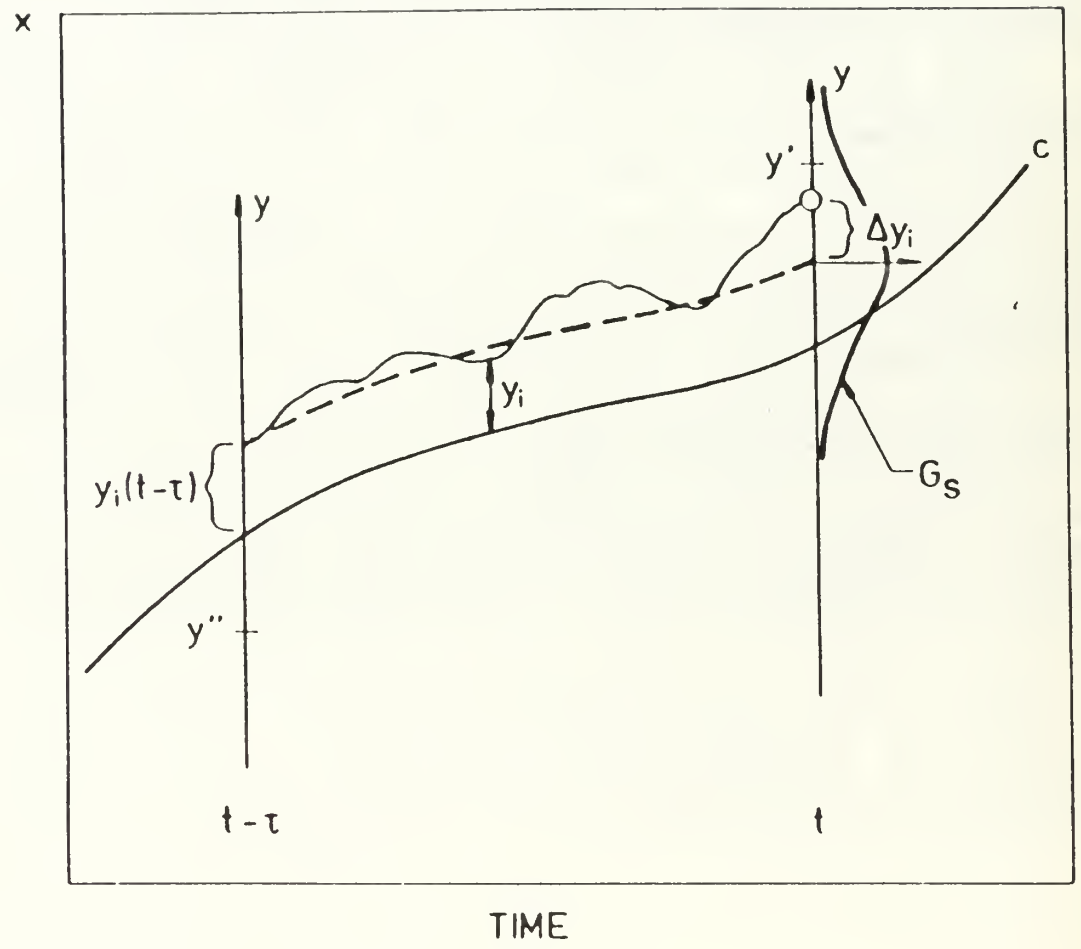

Fig. 8.2.1 The moving frame trajectory, y_i, of a marked fluid particle, i, that at time $t-\tau$, holds the position, $y_i(t-\tau)$. The quantity, $\Delta y_i \equiv y_i(t) - y_i(t-\tau)$, and its gaussian distribution function, G_s, are shown at time t.

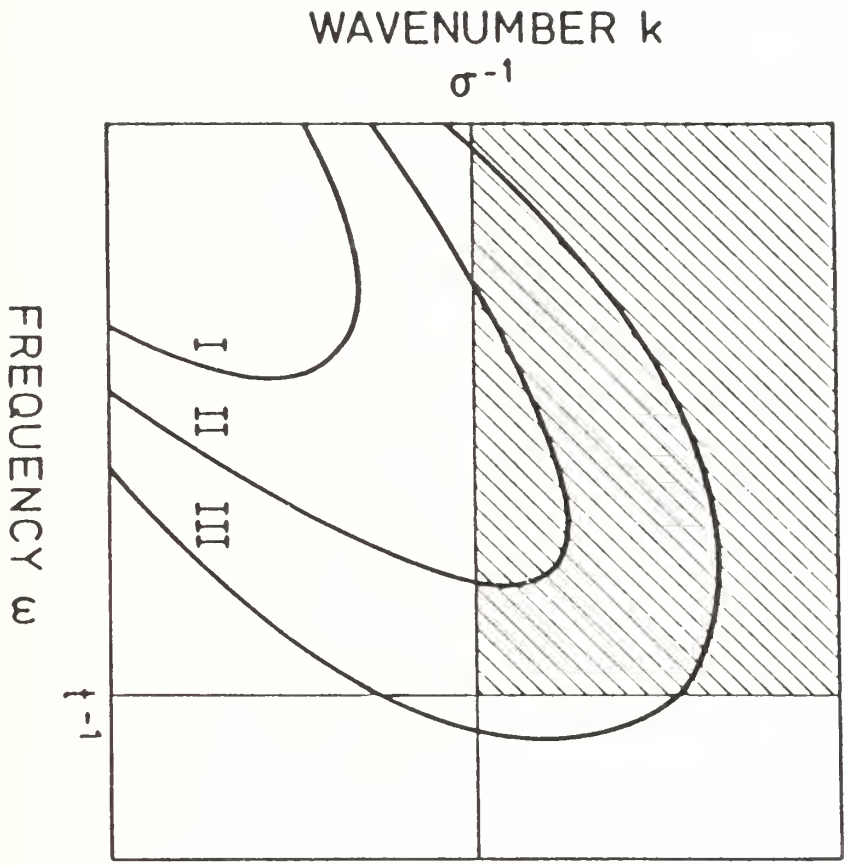

Fig. 8.2.2 Schematic isopleth plot of spectrum, $S(k,\omega)$. Its maximum value is at $(k,\tilde{\omega}) = (0,0)$ from where the function decreases monotonically through the levels I, II, and III. The shaded region is the effective domain of the model defined by vertical line, $\tilde{\omega} = t^{-1}$, (using the low-pass filter, $\sin(\tilde{\omega}t)/\tilde{\omega}t$) and the horizontal line, $k = \sigma^{-1}$ (using the high pass filter, $1 - \exp(-k^2\sigma^2)$).

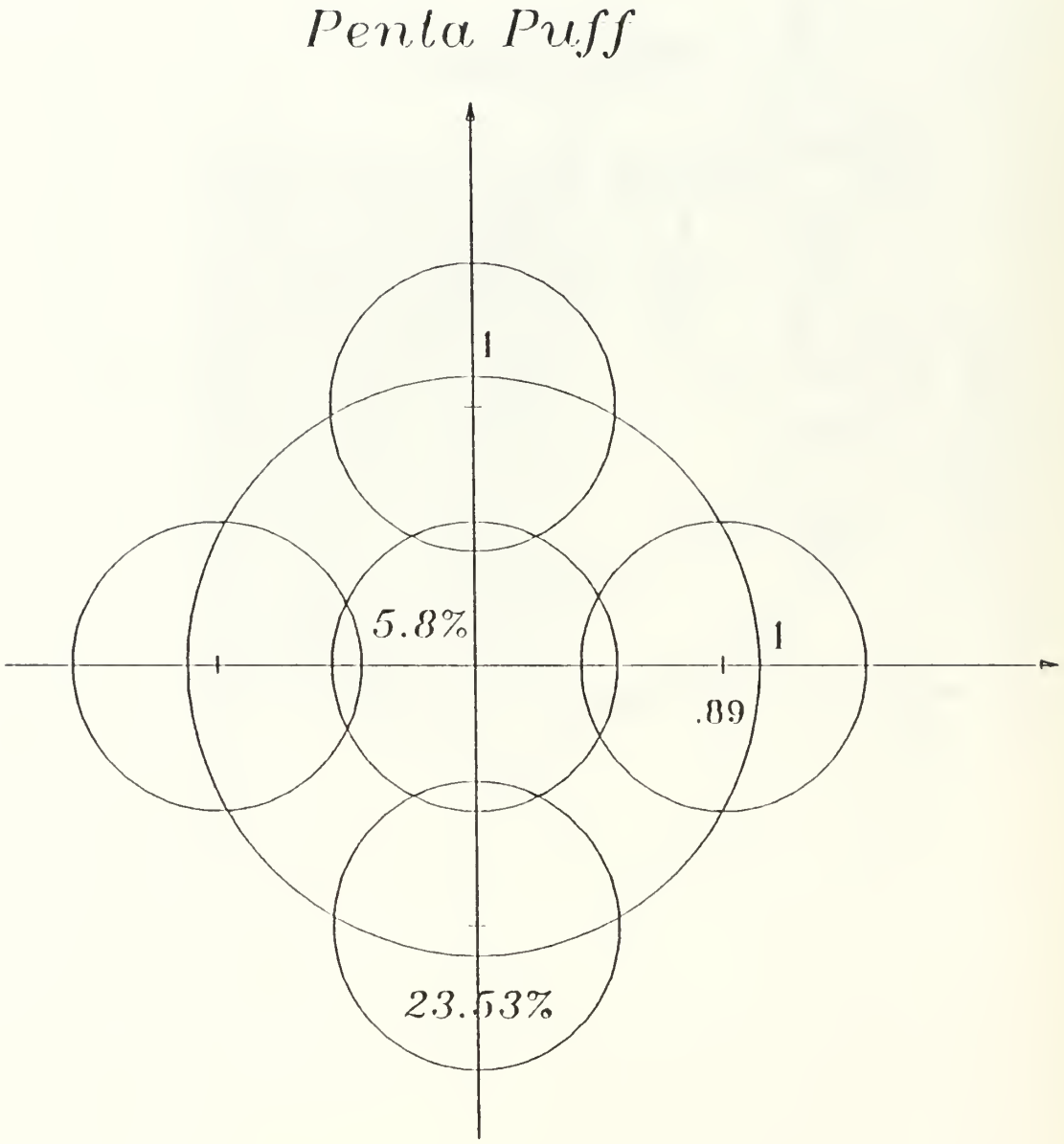

Fig. 8.2.3 Puff pentafurcation: the original single puff of size σ divides into five new puffs, each of size $\frac{1}{2}\ \sigma$, conserving total mass, and peak and second moments of the concentration distribution around the cloud's center of mass point (moment of inertia).

8.3 Comparison Procedures

The following describes how the LINCOM/RIMPUFF model runs were compared with the digitized Mt. Iron data for cases 28, 31, 48, 55, 87, 90, 91 and 110.

First, the LINCOM/RIMPUFF model runs and Mt. Iron case studies were plotted with the SURFER graphics package so the plumes could be visually inspected. By overlaying a model run with a case study it was evident for some cases that the source points were not collocated. The Mt. Iron grids were moved by an appropriate number of grid points in the x and y directions to align the source point of the Mt. Iron case study and the LINCOM/RIMPUFF model run.

Headers at the top of the SURFER formatted *.grd files define the latitude/longitude coordinates in UTMS for the four corners of the LINCOM/RIMPUFF and Mt. Iron dose files. For all of the LINCOM/ RIMPUFF runs, the headers did not correctly locate the source points relative to a map of Vandenberg. By plotting some of the roads at Vandenberg along with the location of VIP-1, the proper coordinates for the surfer header files for each of the model runs were determined. These roads were plotted by picking off latitude and longitude coordinates for points on the roads using a 300' (.3 arc seconds) resolution map of Vandenberg. Program utm.for was written to convert the longitude/latitude values to UTMS coordinates.

For cases 28, 48, 87, 90 and 110 the plotted roads (which were also sampling lines for the Mt. Iron data set) were used to define plume cutoff lines. Since the plumes did not reach Santa Ynez Rd. in cases 28 and 110, these plumes were truncated at Arguello Rd. The plumes were truncated at Santa Ynez Rd. for cases 87 and 90 because there was enough data to define these plumes at Santa Ynez. For case 48, the plume was cut off at Honda Ridge.

The following procedure was used for this evaluation. 1) TEST, an ASCII file was created to hold the input and output names of the LINCOM/RIMPUFF and Mt. Iron grid files. This file is comprised of four file names followed by a blank line for each comparison. For example, to compare a digitized data grid with a model simulation grid for case 28, TEST would look like:

```
mi28.grd        # input file name of Mt. Iron data grid
case28.grd      # input file name of LINCOM/RIMPUFF simulation grid
p28.grd         # output file name of Mt. Iron grid
c28.grd         # output file name of LINCOM/RIMPUFF grid
```

2) The program, drawsurf1.f, was run to collocate the release points, find the merit scores where the hand-drawn isopleths were left untruncated (cases 31, 55 and 91), and to create an output file to contour with TOPO.

3) The header files in all of the LINCOM model files were changed so that the x and y are in UTMS coordinates:

4) Cases 31, 55 and 91 were then complete and ready to be plotted.

5) Program mt3.for was run for the truncation cases: 28, 87, 90 and 110. All concentrations beyond the last sampling line where appreciable doses were measured were set to zero.

6) mt4.for was run for case 48 which was truncated at Honda Ridge.

7) Program drawsrf2.f was run on cases 28, 48, 87, 90 and 110. This program is actually the same as drawsrf1.f except that the format statements to read the input grids are different and also the source point adjustment is not re-evaluated.

8) Cases 28, 48, 87, 90 and 110 were then complete and plotted. The "roads.bln" file was used to overlay some roads on the plots. Some of these roads correspond to sampling lines.

REFERENCES

Baerentsen, J. H., and R. Berkowicz, 1984: Monte Carlo simulation of plume dispersion in the convective boundary layer. Atmos. Environ., 18, 701-12.

Briggs, G.A., 1985: Analytical Parameterizations of Diffusion: the Convective Boundary Layer. J. Climate Appl. Meteorol., 24, 1167-89.

Deardorff, J.W. and G.E. Willis, 1975: A Parameterization of Diffusion into the Mixed Layer. J. Appl. Meteor. 14, 1451-58.

DMAAC, 1976: Vandenberg A.F.B. California AIM-2 Map Scale 1:62,500 Edition 2, Defense Mapping Agency Aerospace Center, St. Louis Air Force Station, Missouri 63118.

Draxler, R.R., 1976: Determination of Atmospheric Diffusion Parameters. Atmos. Environ. 10, 99-105.

Dyer, A.J. and E.F. Bradley, 1982: An Alternative Analysis of Flux-Gradient Relationships at the 1976 ITCE. Bound. Layer Meteorol., 22, 3-19.

Golder, D., 1972: Relations among Stability Parameters in the Surface Layer. Bound. Layer Meteorol., 3, 47-58.

Hanna, S.R. and D.G. Strimatis, 1991: Uncertainties in Hazardous Gas Model Predictions. International Conference and Workshop on Modeling and Mitigating the Consequences of Accidental Releases of Hazardous Materials. American Institute of Chemical Engineers, New York, New York, 345-68.

Haugen, D. A. and J.H. Taylor, 1963: The Ocean Breeze and Dry Gulch Diffusion Program. AFCRL-63-791(I) and 791(II), AFGL, Boston, Mass.

Hinds, W.T., and P.W. Nickola, 1967: The Mountain Iron Diffusion Program. Phase I, BNWL-572, Pacific Northwest Laboratory, Batelle Memorial Institute, Richland, Washington.

Iqbal, M., 1983: Solar Radiation, Acad. Press, NY, 1983, 202-10.

Jackson, P.S. and J.C.R. Hunt, 1975: Turbulent wind flow over a low hill. Q. J. R. Meteorol. Soc. 101, 929-55.

Kaimal, J.C., J.C. Wyngaard, Y. Izumi, and O.R. Cote, 1972: Spectral Characteristics of Surface Layer Turbulence. J. Fluid Mech. 96, 641-69.

Kamada, R.F., 1984: A General Cloud Transmittance Modifier, Solar Energy Journal, 33, 6, 631-32.

Kamada, R.F., C.E. Skupniewicz, J.W. Glendening, G.E. Schacher, T. Mikkelsen, S. Thykier-Nielsen, I. Troen, S.E. Larsen, E.S. Takle, L.N. Ly, and J. Griffin, 1989: Vandenberg Air Force Base Meteorology and Plume Dispersion Handbook for Boundary Layer Releases. Naval Postgraduate School, NPS-61-89-004.

Kamada, R.F., 1989: Preliminary review of flow models considered for use at Vandenberg air force base, Naval Postgraduate School, Monterey, California, NPS-61-89-007.

Kamada, R.F., C.E. Skupniewicz, L. McKay, and S.A. Drake, 1990: An Inversion Height Study in Complex Coastal Terrain, Proc. 5th JANAFF Safety &d Env. Prot. Subcomm. Meeting, Livermore, CA, June 18-20.

Kunkel, B.A. and Y. Izumi, 1990: WADOCT - An Atmospheric Dispersion Model for Complex Terrain, GL-TR-90-0124, ERP. No. 1062.

Liou, K.N. and G.D. Wittman, 1979: Parameterization of the Radiative Properties of Clouds, J. Atmos Sci., 36, 1261-73.

Martin, M. and P. Berdahl, 1983: Characteristics of Infrared Sky Radiation in the United States, LBL-16344, Lawrence Berkeley Labs.

Mikkelsen, T. and R.M. Eckman, 1985: A statistical model for relative diffusion in the surface layer. formulation and experimental evaluation. Proc. 7th Symp. on Turb. and Diff., Boulder, CO, 9/12-15.

Mikkelsen, T., S.E. Larsen, and H.L. Pecsli, 1987: Diffusion of gaussian puffs. Q. J. R. Meteorol. Soc, 113, 81-105.

Mikkelsen, T., S. Thykier-Nielsen, S.E. Larsen, I. Troen, A.F. DeBaas, R.F. Kamada, C.E. Skupniewicz, and G.E. Schacher, 1988: A Model for Accidental Releases in Complex Terrain, 17th NATO/CCMS International Meeting on Air Pollution Modelling and its Application , Cambridge (UK), September 19-22.

Misra, P.K., 1982: Dispersion of nonbuoyant particles inside a convective boundary layer. Atmos. Environ., 16, 239-43.

Monteith, J.L., 1965: Evaporation and Environment. Symp. Soc. Exp. Biol., 19, 205-34.

Pasquill, F. and F.B. Smith, 1983: Atmospheric Diffusion, Ellis Horwood Lim., Halstead Press, Chichester, England.

Penman, H.L., 1948: Natural Evaporation from Open Water, Bare Soil, and Grass, Proc. Roy. Soc. London, A193, 120-95

Skupniewicz, C.E., R.F. Kamada, and G.E. Schacher, Turbulence Measurements over Complex Terrain, 1989: Bound. Layer Meteorol.,

48, 109-28.

Skupniewicz, C.E., R.F. Kamada, S.A. Drake, and L. McKay R.N. Abernathy, K.C. Herr, and G.J. Scherer, and A. Guenther, 1990: "Lompoc Valley Diffusion Experiment Data Report", Naval Postgraduate School Technical Report, NPS61-90-017

Skupniewicz, C.E., J.W. Glendening, and R.F. Kamada, 1991: Atmospheric Boundary Layer Transition Across a Stratocumulus Cloud Edge in a Coastal Zone, Mon. Wea. Review, 119, 10, 2337-57.

SURFER Version 4.0, 1989: Golden Software, Inc., Golden, Colorado 80402.

Thykier-Nielsen, S. and T. Mikkelsen, 1987: RIMPUFF - User's guide/ Version 20. M-2673, Ris0 National Laboratory, DK-4000 Roskilde, Denmark.

Troen I. and A.F. DeBaas, 1986: A spectral diagnostic model for wind flow simulation in complex terrain, Proc. Euro. Wind Energy Assoc. Conf., Rome, October 7-9.

Yamada, T., S. Bunker, and M. Moss, 1991: Numerical Simulations of Atmospheric Transport and Diffusion over Coastal Complex Terrain, J. Appl. Meteorol., to be published April 1992.

DISTRIBUTION LIST

		No.copies
1.	Defense Technical Information Center Cameron Station Alexandria, VA 22314	2
2.	Dudley Knox Library Naval Postgraduate School Monterey, CA 93943-5000	2
3.	Director of Research (012) Naval Postgraduate School Monterey, CA 93943-5000	2
4.	Dept. of Physics (PH) Naval Postgraduate School Monterey, CA 93943-5000	2
5.	Dr. Ray Kamada/061kd Naval Postgraduate School Monterey, CA 93943-5100	7
6.	Capt. David Struck (SSD/CLGR) Los Angeles AFB Los Angeles, CA 90009-2960	2
7.	Prof. Gordon Schacher Dean of Science and Engineering Naval Postgraduate School Monterey, CA 93943-5100	1
8.	Mr. Charles Larcomb (SSD/SDW) Los Angeles AFB Los Angeles, CA 90009-2960	1
9.	Maj. Anita Dye (AFSPACECOM/DOW) Peterson AFB, CO 80914-5000	1
10.	Lt. Col. Hergenrader (AFSPACECOM/SGPB) Peterson AFB, CO 80914-5000	1
11.	Capt. Mike Moss (AFESC/RDVS) Tyndall AFB, FL 32403-6001	1
12.	Lt. Col. Stephen Pryor (730 SPW) Vandenberg AFB, CA 93437-5000	1
13.	Lt. Col. Winston Crandall (PL/WE) Kirtland AFB, NM 87117-6008	1
14.	Mr. Glen Boire (730 SPW/DOW) Vandenberg AFB, CA 93437-5000	1

15. Mr. Steve Sambol (730 SPW/DOW) 1
Vandenberg AFB, CA 93437-5000

16. Mr. Darryl Dargitz (WSMC/SEY) 1
Vandenberg AFB, CA 93437-5000

17. Mr. Randy Nyman 1
ACTA
Vandenberg AFB, CA 93437-5000

18. Mr. Davis Downing 1
Geodynamics Corp.
P.O. Box 5548
Vandenberg AFB, CA 93437

19. Dr. Don Ermak 1
Lawrence Livermore National Lab
P.O. Box 808, L-262
Livermore, CA 94550

20. Mr. Bruce Kunkel (PL/GPAA) 1
Hanscom AFB, MA 01730-5000

21. Mr. Bill Boyd (45 WS/WER) 1
Patrick AFB, FL 32925-5000

22. Mr. Dick Tatsch (45 SPW/SEMP) 1
Patrick AFB, FL 32925-5000

23. Mr. Don Cameron (AFFTC/WE) 1
Edwards AFB, CA 93523-5000

24. Col. David Schmargie (ET) 1
Vandenberg AFB, CA 93437-5000

25. Mr. Ron Cionco 1
US Army Atmospheric Sciences Lab
SLCAS-AR-M
White Sands Missile Range, NM 88002-5501

26. Mr. John Edwards 1
SSD/DEV
Los Angeles, AFB, CA 90009-2960

27. Mr. Larry Mendenhall 1
Geodynamics Corp.
21171 Western Ave
Suite 100
Torrence, CA 90501

28. Dr. Raymond Hedner (Aerospace/El Segundo) 1
PO Box 92957
Los Angeles, CA 90009

29. Dr. Robert Abernathy (Aerospace/El Segundo) 1
PO Box 92957
Los Angeles, CA 90009

30. Mr. Bart Lundblad (Aerospace/El Segundo) 1
PO Box 92957
Los Angeles, CA 90009

31. Mr. Fred Sobottka (Aerospace/VAFB) 1
PO Box 5068
Vandenberg AFB, CA 93437-0068

32. Mr. Lou Ullian (SE) 1
Patrick AFB, FL 32925-5000

33. Mr. Jose Caraballo 1
NASA
Industrial Safety/RT-SOE
KSC, Florida 39899

34. Mr. Jan Zysko 1
NASA
PM-PCO-4
KSC, Florida 39899

35. Dr. T. Yamada 1
Yamada Science and Art
147 Monterey Bay Dr. S.
Los Alamos, NM 87544

36. Dr. D. Pepper 1
5301 N. Commerce #A
Moorpark, CA 93021

37. Dr. Walt Lyons 1
46040 Weld County Rd 13
Ft. Collins, CO 80524

38. Dr. Roger Gibbs 1
Naval Surface Warfare Center
Dahlgren, Virginia 22448-5000

39. Dr. Kenneth Moe 1
USAF Space Division
Box 92960 World Way
Los Angeles, CA 90009-2960